Atmos. Chem. Phys., 14, 505–521, 2014
www.atmos-chem-phys.net/14/505/2014/
doi:10.5194/acp-14-505-2014

Atmospheric
Chemistry
and Physics

Long-range transport of giant particles in Asian dust identified by physical, mineralogical, and meteorological analysis

G. Y. Jeong[1]**, J. Y. Kim**[2]**, J. Seo**[2,3]**, G. M. Kim**[1]**, H. C. Jin**[2]**, and Y. Chun**[4]

[1]Department of Earth and Environmental Sciences, Andong National University, Andong 760-749, Republic of Korea
[2]Korea Institute of Science and Technology (KIST), Seoul 136-791, Republic of Korea
[3]School of Earth and Environmental Sciences, Seoul National University, Seoul 151-742, Republic of Korea
[4]Asian Dust Research Division, National Institute of Meteorological Research, Seoul 156-720, Republic of Korea

Correspondence to: G. Y. Jeong (jearth@anu.ac.kr)

Received: 28 May 2013 – Published in Atmos. Chem. Phys. Discuss.: 13 August 2013
Revised: 8 November 2013 – Accepted: 3 December 2013 – Published: 15 January 2014

Abstract. Giant particles transported over long distances are generally of limited concern in atmospheric studies due to their low number concentrations in mineral dust and possible local origin. However, they can play an important role in regional circulation of earth materials due to their enormous volume concentration. Asian dust laden with giant particles was observed in Korea on 31 March 2012, after a migration of about 2000 km across the Yellow Sea from the Gobi Desert. Scanning electron microscopy (SEM) revealed that 20 % of the particles exceeded 10 µm in equivalent sphere diameter, with a maximum of 60 µm. The median diameter from the number distribution was 5.7 µm, which was larger than the diameters recorded of 2.5 and 2.9 µm in Asian dust storms in 2010 and 2011, respectively, and was consistent with independent optical particle counter data. Giant particles (> 10 µm) contributed about 89 % of the volume of the dust in the 2012 storm. Illite–smectite series clay minerals were the major mineral group followed by quartz, plagioclase, K-feldspar, and calcite. The total phyllosilicate content was ∼52 %. The direct long-range transport of giant particles was confirmed by calcite nanofibers closely associated with clays in a submicron scale identified by high-resolution SEM and transmission electron microscopy. Since giant particles consisted of clay agglomerates and clay-coated quartz, feldspars, and micas, the mineral composition varied little throughout the fine (< 5 µm), coarse (5–10 µm), giant-S (10–20 µm), and giant-L (> 20 µm) size bins. Analysis of the synoptic conditions of the 2012 dust event and its migration indicated that the mid-tropospheric strong wind belt directly stretching to Korea induced rapid transport of the dust, delivering giant particles. Giant dust particles with high settling velocity would be the major input into the terrestrial and marine sedimentary and ecological systems of East Asia and the western Pacific. Analysis of ancient aeolian deposits in Korea suggested the common deposition of giant particles from Asian dust through the late Quaternary Period. The roles of giant particles should be reviewed with regard to regional circulation of mineral particles and nutrients.

1 Introduction

Asian dust is composed of soil particles from the surfaces of western China and Mongolia. Asian dust is transported eastward across China, Korea, Japan, and the North Pacific. The size, morphology, chemistry, and mineralogy of dust particles are important for modeling their transport (Westphal et al., 1987; In and Park, 2002), radiative impacts (Tegen and Lacis, 1996; Reid et al., 2003; Park et al., 2005; Kandler et al., 2007; Kim et al., 2008), and chemical reactions (Laskin et al., 2005; Jeong and Chun, 2006; Dentener et al., 1996; Sullivan et al., 2009; Song et al., 2013). They supply inorganic nutrients to marine ecosystems (Meskhidze et al., 2005), and are eventually deposited on land and the ocean floor to form aeolian sediments, recording paleoclimatic changes through the Quaternary Period (Bradley, 1999). The Korean Peninsula lies in the main path of the Asian dust transfer and is suitable for observation of its physical, optical, and chemical characteristics (Seinfeld et al., 2004).

In studies of mineral dust, attention is often paid to fine particles because they are more respirable, produce harmful effects (Dockery et al., 1993), react with gaseous pollutants (Dentener et al., 1996), and reflect light close to solar wavelengths (Tegen and Lacis, 1996). Modeling of the radiative properties of mineral dust considers particles $< 10\,\mu m$ because the atmospheric lifetime of particles $> 10\,\mu m$ is less than 1 day (Tegen and Lacis, 1996; Seinfeld and Pandis, 2006). Chun et al. (2001) suggested that particles $> 10\,\mu m$ in Asian dust collected in Korea may be derived from local sources. Thus, real-time monitoring networks of Asian dust by governmental institutes of Korea (National Institute of Environmental Research and Korea Meteorological Administration) measure $PM_{2.5}$ and PM_{10}, but not total suspended particulate (TSP) matter.

Although particles $> 10\,\mu m$ have attracted little attention, they can be transported over long distances, and may play significant roles in regional circulation of materials. Long-range transport of coarse particles has been reported in Saharan dust across the Atlantic Ocean and the Mediterranean Sea (Goudie and Middleton, 2001; Díaz-Hernández and Párraga, 2008). However, there are rarely reports dedicated to the research of coarse mineral dusts providing systematic data of particle size and mineralogy with a meteorological interpretation about their outbreak and migration. Although number concentrations of relatively coarse particles are normally low compared with fine particles, their mass/volume concentrations can be high (Seinfeld and Pandis, 2006). The mass flux of dust via dry deposition can be controlled by a relatively small fraction of aerodynamically large particles (Coude-Gaussen et al., 1987; Arimoto et al., 1997). They are absorbers of light at thermal wavelengths (Tegen and Lacis, 1996). On a regional scale near dust sources, the radiative effect of coarser particles is not negligible (Ginoux, 2003). The bulk geochemistry and isotopic composition of dust have largely been determined for TSP, where the mass is dominated by coarse particles (Kanayama et al., 2002).

The modal particle diameters of volume–size distribution of Asian dust have been reported to range from 2 to $4\,\mu m$ as measured with an optical particle counter in Seoul, Korea (Chun et al., 2001, 2003; Jeong, 2008), and British Columbia, Canada (McKendry et al., 2008), and using a cascade impactor in Japan (Mori et al., 2003; Mikami et al., 2006). However, size distribution curves of Asian dust often extend over $10\,\mu m$. Park and Kim (2006) reported a mean diameter of $9.12\,\mu m$ on a mass basis using a cascade impactor in Seoul. In addition, there are probably interevent and in-event fluctuations of particle size distribution depending on synoptic conditions, which have not been studied in detail. Giant particles were observed in the central North Pacific by Betzer et al. (1988), who traced them to Asian sources, indicating global circulation of giant particles. However, there are almost no reports on the occurrence and characterization of Asian dust heavily laden with giant particles despite numerous articles on Asian dust events.

Asian dust was observed in Korea on 31 March 2012. Despite a low TSP concentration, it was laden with giant particles compared to two previous events (2010 and 2011). The 2012 dust provided a unique opportunity to observe the long-range transport of the giant particles. We report physical, mineralogical and meteorological characteristics of the 2012 dust event, in comparison to previous events, and discuss the remote origin of giant particles as well as the implications for regional circulation of mineral particles and elements. Here, dust particles were classified as fine ($< 5\,\mu m$ in diameter), coarse (5–$10\,\mu m$), giant-S (10–$20\,\mu m$), and giant-L ($> 20\,\mu m$) particles.

2 Dust outbreak and migration

In terms of spatiotemporal evolution of the dust storm, the infrared measurements by geostationary satellites are fairly useful to trace the dust outbreak and migration in the short-term timescale. To detect dust aerosols from the satellite, the brightness temperature difference (BTD) between $10.8\,\mu m$ and $12.0\,\mu m$ bands ($T_{11\,\mu m} - T_{12\,\mu m}$) has been widely used (Ackerman, 1997). BTD is positive over a thin ice cloud and negative over the dust storms (Chaboureau et al., 2007). However, since the BTD technique has low sensitivity on the ocean and discontinuity between daytime and nighttime images, other dust indices have been developed and provided by the Korea Meteorological Administration (KMA).

In this study, aerosol index derived from the Communication, Ocean, and Meteorological Satellite (COMS) of the KMA launched on 27 June 2010 is used for the dust events in 2011 and 2012 (Fig. 1). The COMS aerosol index is based on the BTD technique, but derived from the difference between BTD and the background threshold value (BTV), which is defined as a difference between the maximum of $T_{11\,\mu m}$ for the past 10 day and observed $T_{12\,\mu m}$ at each pixel. Since BTV and BTD are same in the clear sky condition, the difference between BTD and BTV can be utilized for the detection of the Asian dust (Hong et al., 2010). To reveal the 2010 dust event, which occurred before the launching of COMS, we also show (in Fig. 1) the infrared difference dust index (IDDI) (Legrand et al., 2001) derived from the Multi-functional Transport Satellite-1R (MTSAT-1R) of the Japan Meteorological Agency launched on 26 February 2005. MTSAT-1R IDDI is based on the brightness temperature in the dust-sensitive $10.8\,\mu m$ band ($T_{11\,\mu m}$) and is derived from the difference between $T_{11\,\mu m}$ in the clear sky condition and observed $T_{11\,\mu m}$.

The images of COMS aerosol index during the 2012 dust event (National Meteorological Satellite Center, 2013) reveal the dust outbreak in the Gobi Desert of southern Mongolia and northern China ($40°$–$45°$ N, $90°$–$105°$ E) at around 12:00 Korea Standard Time (KST) on 30 March 2012 and its migration to the east (Fig. 1). The dust arrived at the western coast of Korea at around 16:00 KST on 31 March, based
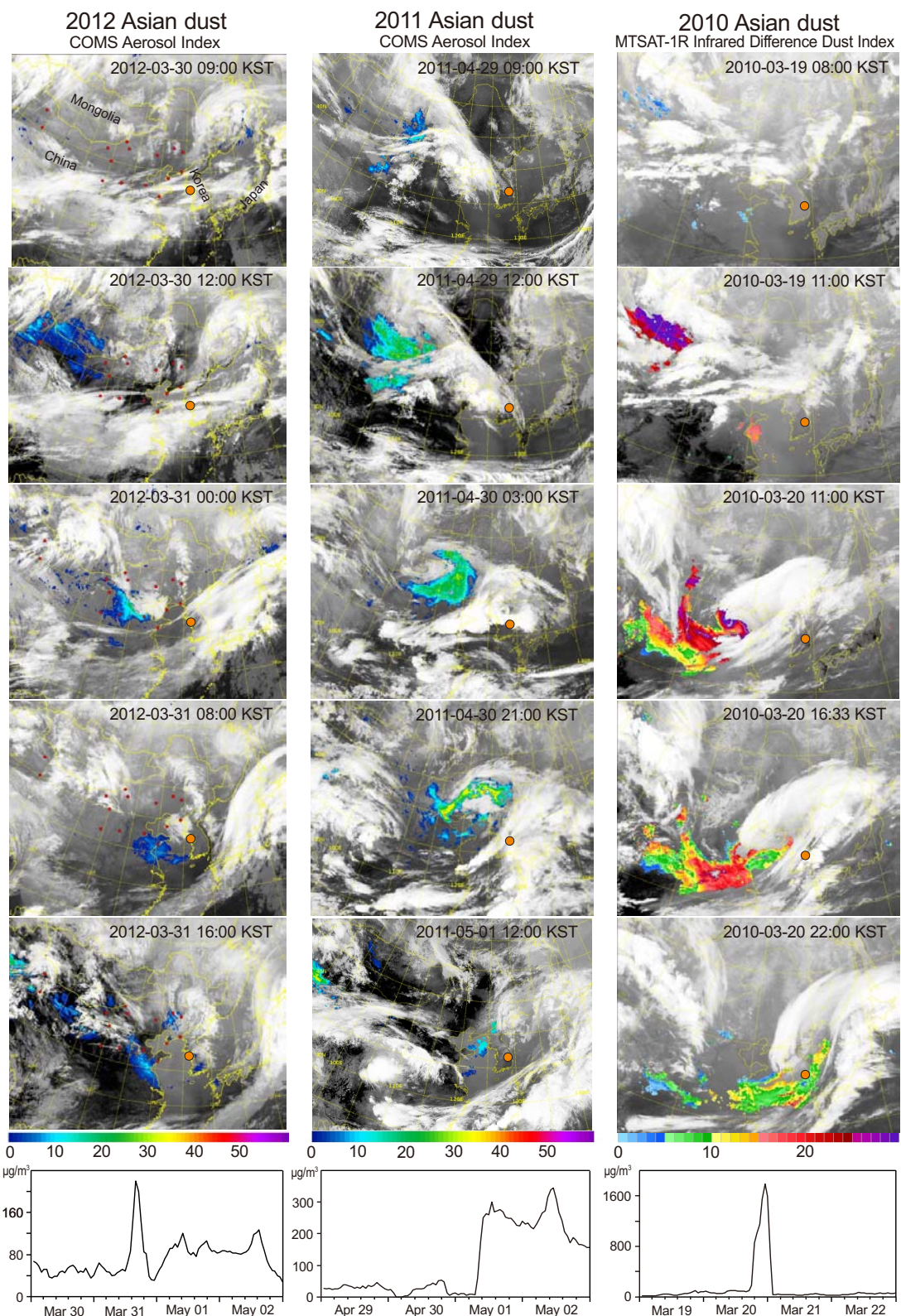
Fig. 1. COMS and MTSAT satellite images of the Asian dust index of three events observed in Korea. Solid orange circles are the TSP sampling sites in Korea. The graphs are plots of hourly PM_{10} concentrations over 4 days in the Korea Meteorological Administration aerosol monitoring stations near sampling sites. Red dots in the 2012 COMS images are the stations of the Korea–China joint Asian dust monitoring networks.

on the time series of PM$_{10}$ concentrations in Seoul (KMA, 2013). The time of flight was about 28 h for the migration of about 2000 km. The duration of the Asian dust event was 4 h with a peak PM$_{10}$ concentration of 220 μg m^{-3}.

During the 2011 dust event, the images of COMS aerosol index images show that the dust outbreak occurred in the Gobi Desert (40°–45° N, 95°–105° E) at around 12:00 KST on 29 April 2011 and the dust arrived at the sampling site (Andong) at 09:00 KST on 1 May 2011. The time of flight was about 45 h and the event lasted for about 3 days (ca. 62 h) with a peak PM$_{10}$ concentration of 344 μg m^{-3}.

MTSTR-1R IDDI images during the 2010 dust event show the dust outbreak in the Gobi Desert of southern Mongolia (43°–46° N, 100°–110° E) at 11:00 KST on 19 March 2010. The dust arrived at around 22:00 KST on March 20 with the time of flight of about 35 h. Time series of PM$_{10}$ concentrations indicated short duration (7 h) at the sampling site (Andong, Korea) with a peak concentration of 1788 μg m^{-3}. Although the sampling site used for the 2011 and 2010 dust events (Andong) was different from that used for the 2012 dust event, mineralogical and physical differences between Korean sites were not likely to be significant because Asian dust was a nationwide phenomenon over the Korean Peninsula in both events.

3 Dust samples and methods

The TSP Asian dust in 2012 was collected using a high-volume sampler (Thermo Scientific) fitted with a Teflon-coated borosilicate glass-fiber filter (8 in.×10 in. PALLFLEX membrane filters). The sampler was installed on a peak at Deokjeok Island (190 m above sea level, 37°13′59″ N, 126°08′57″ E) off the western coast of Korea, 85 km from Seoul. Sampling proceeded for 24 h from 09:00 on 31 March to 08:00 on 1 April 2012. The flow rate of the sampler was adjusted to 250 L min^{-1} to avoid coagulation of particles on the filter surface. The measured TSP concentration for 24 h was 255 μg m^{-3}. For comparison, we used TSP samples collected by the same procedure on 20 March 2010, and 1 May 2011 in Andong (36°32′34″ N, 128°47′56″ E). The late Quaternary sediments of ancient Asian dust were sampled from a Paleolithic excavation site at Jeongok, Korea (Shin et al., 2004; Jeong et al., 2013). The exact ages of the sediments are debated but certainly younger than ca. 500 000 yr (Jeong et al., 2013). The silty sediments were prepared as polished thin sections after epoxy impregnation for comparison to Asian dust particles.

The physical and mineralogical characterization of the Asian dust was carried out by the electron microscopic analysis of single particles. Mineralogical analysis of bulk dust using X-ray powder diffraction was not possible due to the low mass of samples. For scanning electron microscopy (SEM), three layers of conductive sticky carbon tape were attached to Cu–Zn stubs. The filter surface was touched lightly with car-

bon tape. The filter surface was observed to change from light yellow brown to white, indicating transfer of the dust particles onto the carbon tape. Since our goal was to perform the entire morphological, chemical, and high-resolution electron microscopic analyses from one specimen, the particles were transferred onto the stable substrate of conductive sticky carbon tape. The dust particles collected on the filter were not suitable for the high resolution SEM and focused ion-beam (FIB) work due to charging even after metal coating.

After platinum coating for electrical conductivity, the morphology and chemistry of particles were analyzed with a TESCAN LMU VEGA microscope equipped with an IXRF energy dispersive X-ray spectrometer (EDXS) at 20 kV acceleration voltage and 15 mm working distance. The IXRF EDXS detects elements from carbon. Numbers of analyzed particles were 3085, 1441, and 1689 in 2012, 2011, and 2010 dusts, respectively. High-resolution imaging of the surface microtextures of giant dust particles was performed with a JEOL JSM 6700F field emission gun microscope at 5 kV acceleration voltage and 8 mm working distance. SEM work was performed at the Center for Scientific Instruments, Andong National University. Then, ultrathin slices (ca. 50 nm in thickness) of about ca. 6 μm × 6 μm size were cut from dust particles using a SMI3050TB FIB instrument. Submicron minerals in the slices were characterized on the basis of lattice fringe spacing, electron diffraction, and chemical composition using a JEOL JEM3010 transmission electron microscope (TEM) at the National Center for Inter-University Research Facilities, Seoul National University and an Oxford EDXS system of a JEOL JEM 2010 TEM. The polished thin sections of the aeolian sediment from the Paleolithic site were examined in backscattered electron imaging mode using a TESCAN SEM instrument.

Single particle analysis of mineral dust employing SEM–EDXS analysis is basically qualitative because of the irregular shape and wide size range of dust particles (Blanco et al., 2003; Kandler et al., 2007; Fletcher et al., 2011). In addition, the dust particles are mostly the agglomerates of subgrains of wide-ranging mineralogy and size in varying ratios. Thus, quantitative mineralogical analysis of single dust particle is practically impossible. However, the mineral types dominating dust particles can be reliably estimated from the EDX spectral pattern, compared with those of reference mineral particles. The mineralogical identification of the Asian dust particles was greatly facilitated by referring to quantitative mineralogical and microscopic data of the source soils and the Chinese loess deposited from the Asian dust around desert sources (Jeong, 2008; Jeong et al., 2008, 2011). Additionally, our SEM–EDXS identifications of Asian dust particles were confirmed by the TEM and EDXS analysis of the FIB slices of individual dust particles.

Dust particles were classified depending on their predominant mineral using EDX spectra following the identification procedure of Jeong (2008). Quartz and feldspars (K-feldspar and plagioclase) were easily identified. However,

mineralogical classification of clay minerals was more difficult due to their complex chemistry and structural diversity (Weaver, 1989). Fine-scale mixing of submicron platelets of clay minerals made classification more difficult. Clay minerals in dust and sediments include illite, smectite, illite–smectite mixed layers, kaolinite, vermiculite, and chlorite (Shi et al., 2005; Jeong and Chun, 2006; Jeong, 2008; Jeong et al., 2008, 2011). Kaolinite and chlorite were readily identified from their EDX spectra; however, illite, smectite, illite–smectite mixed layers, and vermiculite could not be positively identified because of their fine-scale mixing. Therefore, to avoid over-interpretation they were grouped into illite–smectite series clay minerals (ISCMs). The EDX spectra of many biotite and chlorite particles show signatures of partial weathering. Weathered biotite and chlorite that have partly lost of K, Mg, and Fe are often difficult to distinguish from ISCMs. Some muscovite grains with high Mg and Fe contents cannot be readily distinguished from illite. Thus, ISCMs, kaolinite, chlorite, muscovite, and biotite were further classed as total phyllosilicates. ISCM may be underestimated by counting the quartz and feldspar grains with ISCM coatings as quartz and feldspar particles, but overestimated by counting the ISCM agglomerates with quartz and feldspar inclusions as ISCM particles. Thus, both the errors will be partly canceled. Obviously, single-particle counting method is semiquantitative. Nevertheless, the results in Tables 2–4 are internally consistent, showing the distribution characteristics of minerals through different dust sizes and events. Jeong (2008) showed that mineral compositions obtained by the single-particle counting were consistent with those determined by X-ray diffraction analysis.

Particle diameters equivalent to a sphere were derived from 2-D images. The shape of particles in 2-D images approximates an ellipse (Reid et al., 2003). The orthogonal long and short dimensions of particle ellipses were measured using Corel Draw®. The surface area and volume of the spheroids and the diameter of the equivalent spheres were calculated assuming spheroidal 3-D morphology of the particles (Reid et al., 2003). Large micaceous (muscovite, biotite, and weathered equivalents) flakes ($>20\,\mu m$) could not be approximated by spheroidal morphology. Their volumes were calculated by multiplying the 2-D area by thickness, assuming a 7 : 1 ratio of area-equivalent diameter to depth, because the ratios of micaceous flakes in Chinese loess ranged from 5 : 1 to 10 : 1 (Jeong et al., 2008, 2011; Jeong and Lee, 2010). Particle sizes were divided into 12 size bins from 0.5 to $60\,\mu m$. The number, surface area, and volume fractions of the bins divided by the width of each bin were plotted against particle diameter on a logarithmic scale (Reist, 1993). Volume distribution is almost equivalent to mass distribution because the densities of the major minerals fall into a narrow range (2.6–2.9 g cm^{-3}).
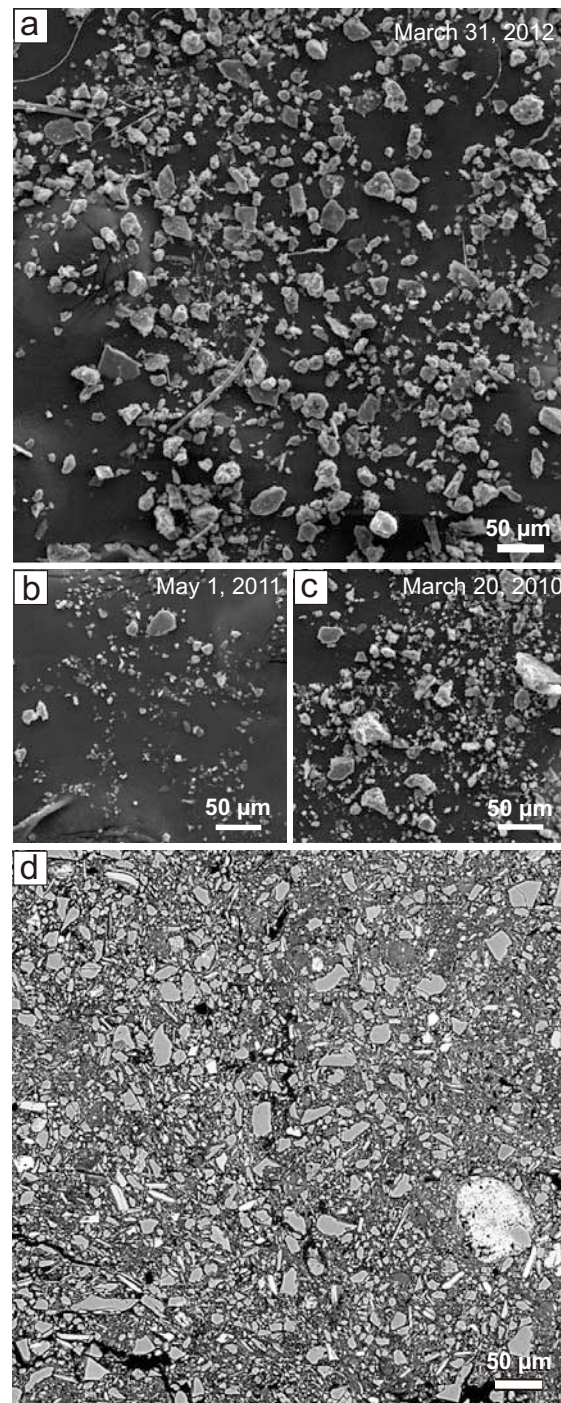
Fig. 2. Scanning electron micrographs of Asian dust particles. **(a)** Giant Asian dust particles, 31 March 2012, Deokjeok Island. Curved threads are contaminants from borosilicate glass-fiber filter. **(b)** Asian dust, 1 May 2011, Andong. **(c)** Asian dust, 20 March 2010, Andong. **(d)** Back-scattered electron image of the polished, thin section of aeolian sediment from the Jeongok Paleolithic site, showing quartz, K-feldspar, and plagioclase particles (bright gray contrast) in the fine clay matrix (dark gray contrast) with pores (black) impregnated with epoxy resin.

Table 1. Particle number, surface area, and volume distribution of three Asian dusts from SEM measurements with basic properties.

Diameter (μm)	ΔN	$\Delta N/(N_T \Delta \log D)$	ΔS (μm^2)	$\Delta S/(S_T \Delta \log D)$	ΔV (μm^3)	$\Delta V/(V_T \Delta \log D)$
2012 (Md = 5.7 μm, PM$_{10}$ = 181 μg m^{-3}, duration time = 4 h)[a]						
0.5–1	0	0.00	0	0.00	0	0.00
1–2	29	0.03	296	0.00	90	0.00
2–3	296	0.54	6174	0.04	2735	0.01
3–4	481	1.25	18 424	0.18	10 839	0.04
4–6	849	1.56	65 891	0.45	55 065	0.13
6–8	494	1.28	76 220	0.74	88 849	0.30
8–10	325	1.09	82 309	1.03	121 106	0.53
10–15	365	0.67	169 056	1.16	347 368	0.83
15–20	143	0.37	134 371	1.30	388 857	1.32
20–40	91	0.10	187 604	0.76	829 779	1.17
40–60	12	0.02	84 314	0.58	681 117	1.63
n	3085					
Giant-S %	16.5		36.8		29.1	
Giant-L %	3.3		33.0		59.8	
2011 (Md = 2.9 μm, PM$_{10}$ = 273 μg m^{-3}, duration time = 62 h)						
0.5–1	7	0.02	20	0.00	3	0.00
1–2	308	0.71	2635	0.12	744	0.03
2–3	438	1.73	8706	0.70	3729	0.26
3–4	310	1.72	11 635	1.32	6762	0.65
4–6	265	1.04	18 925	1.53	15 393	1.05
6–8	70	0.39	10 105	1.15	11 486	1.11
8–10	25	0.18	6124	0.90	9145	1.14
10–15	13	0.05	5755	0.46	11 886	0.81
15–20	4	0.02	4173	0.47	12 723	1.23
20–40	1	0.00	2369	0.11	11 096	0.44
40–60	0	0.00	0	0.00	0	0.00
n	1441					
Giant-S %	1.2		14.1		29.7	
Giant-L %	0.1		3.4		13.4	
2010 (Md = 2.5 μm, PM$_{10}$ = 1518 μg m^{-3}, duration time = 7 h)						
0.5–1	18	0.04	45	0.00	7	0.00
1–2	541	1.06	4864	0.19	1211	0.03
2–3	501	1.68	9713	0.65	4088	0.19
3–4	269	1.27	10 158	0.96	5921	0.38
4–6	225	0.76	16 917	1.13	14 136	0.65
6–8	68	0.32	10 346	0.97	12 144	0.78
8–10	31	0.19	7365	0.89	10 838	0.90
10–15	26	0.09	11 961	0.80	25 877	1.19
15–20	5	0.02	4716	0.44	13 758	0.89
20–40	5	0.01	8995	0.35	36 016	0.96
40–60	0	0.00	0	0.00	0	0.00
n	1689					
Giant-S %	1.8		19.6		32.0	
Giant-L %	0.3		10.6		29.0	

[a] Md is the median particle diameter on number basis. PM$_{10}$ value is the mean of hourly measurements for 4 h around peak concentration (Korea Meteorological Administration, 2013).

Table 2. Mineral compositions of Asian dust TSP collected on 31 March 2012 (unit in %).

Mineral	Total ($n = 2870$)			Fine ($< 5\,\mu m$)[1] ($n = 1555$)[2]			Coarse (5–$10\,\mu m$) ($n = 1130$)			Giant-S (10–$20\,\mu m$) ($n = 490$)			Giant-L ($> 20\,\mu m$) ($n = 95$)		
	No.	Area	Vol.	No.	Area	Vol.	No.	Area	Vol.	No.	Area	Vol.	No.	Area	Vol.
Phyllosilicate															
Total	52.3	52.7	52.1	52.0	53.5	54.2	54.2	55.1	54.3	49.2	50.7	48.2	49.5	53.4	53.9
ISCMs[3]	42.1	39.2	36.1	42.4	43.4	44.1	43.2	43.3	42.5	40.2	40.8	37.9	33.7	33.4	33.6
Kaolinite	2.4	3.0	4.5	3.5	2.5	2.9	1.7	1.6	1.7	1.0	1.2	1.2	3.2	6.5	7.0
Muscovite	1.5	2.6	3.5	0.7	0.8	0.7	1.9	2.5	2.5	1.8	1.4	1.3	3.2	4.4	5.1
Chlorite	3.5	3.0	2.6	3.1	4.1	3.7	4.3	4.3	4.2	2.7	3.0	3.5	3.2	2.0	1.7
Biotite	2.9	4.9	5.4	2.2	2.6	2.8	3.1	3.4	3.4	3.5	4.3	4.3	6.3	7.1	6.5
Talc	0.0	0.0	0.0	0.1	0.1	0.1	0.0	0.0	0.0	0.0	0.0	0.0	0.0	0.0	0.0
Other silicates															
Quartz	19.7	21.1	25.0	17.9	17.6	17.7	20.1	20.1	20.7	22.4	21.5	20.8	22.1	21.8	28.5
Plagioclase	10.3	11.9	10.1	9.1	9.7	9.1	11.2	11.2	11.4	10.8	11.3	13.8	10.5	13.6	7.8
K-feldspar	5.2	5.0	4.4	5.0	5.3	5.1	4.2	4.0	4.0	7.6	6.8	7.2	6.3	3.5	2.9
Amphibole	0.9	0.9	0.8	0.8	1.1	0.8	0.8	0.8	0.9	1.0	0.7	0.7	2.1	1.1	0.8
Pyroxene	0.1	0.2	0.3	0.0	0.0	0.0	0.1	0.1	0.1	0.0	0.0	0.0	1.1	0.6	0.5
Titanite	0.2	0.2	0.3	0.3	0.4	0.3	0.1	0.1	0.1	0.0	0.0	0.0	1.1	0.7	0.6
Zoisite	0.4	0.4	0.1	0.2	0.1	0.2	0.6	0.5	0.5	0.4	0.7	0.2	0.0	0.0	0.0
Non-silicates															
Calcite	6.7	6.0	5.9	7.2	6.8	6.5	6.3	6.1	6.1	6.3	6.4	7.1	7.4	5.4	5.1
Dolomite	1.2	0.5	0.4	2.0	1.5	1.7	0.8	0.7	0.7	0.6	0.7	0.8	0.0	0.0	0.0
Iron oxides	1.6	0.6	0.4	2.7	2.0	2.0	0.8	0.7	0.6	1.0	0.8	0.8	0.0	0.0	0.0
Fe–Ti oxides	0.4	0.2	0.1	0.4	0.5	0.4	0.4	0.4	0.4	0.4	0.3	0.2	0.0	0.0	0.0
Ti oxides	0.1	0.0	0.0	0.3	0.4	0.3	0.1	0.1	0.1	0.0	0.0	0.0	0.0	0.0	0.0
Gypsum	0.8	0.1	0.0	1.9	1.0	1.2	0.1	0.0	0.0	0.0	0.0	0.0	0.0	0.0	0.0
Apatite	0.1	0.1	0.0	0.2	0.1	0.2	0.1	0.1	0.1	0.2	0.1	0.1	0.0	0.0	0.0
Pyrite	0.0	0.0	0.0	0.1	0.2	0.2	0.0	0.0	0.0	0.0	0.0	0.0	0.0	0.0	0.0

[1] Particle diameter of equivalent sphere.
[2] Number of analyzed particles.
[3] Illite–smectite series clay minerals (illite, smectite, and their mixed layers).

4 Results

4.1 Particle size

SEM images revealed that the particles of 2012 dust were much larger than those in 2010 and 2011 dusts. Giant particles were common in the 2012 dust (Fig. 2a), while they were rare in the 2010 and 2011 dusts (Fig. 2b, c). Number distributions of the three dusts showed roughly log-normal distributions (Fig. 3, Table 1). The median equivalent-sphere diameter of the 2012 dust was $5.7\,\mu m$ and the maximum was $60\,\mu m$. The proportion of giant particles (giant-S and giant-L) was 20 % on a number basis, but they contributed 89 % of the total volume. Giant-L particles occupied 60 % of the volume. In contrast, the median diameters of the 2010 and 2011 dusts were 2.5 and $2.9\,\mu m$, respectively. The number proportions of the giant particles were only 2 and 1 % in the 2010 and 2011 dusts, respectively, while the respective volume proportions were 61 and 43 %. The volume contributions of giant-L particles were 29 and 13 % in both dusts. SEM backscattered electron images of thin sections of the sediment (Fig. 2d) identified giant particles of quartz and feldspar enclosed in the clay matrix.

4.2 Particle mineralogy

Phyllosilicates were the most common mineral group in 2012 dust particles (Table 2). The number and volume abundance of total phyllosilicates were 52.3 and 52.1 %, respectively. ISCMs were the major phyllosilicates (42.1 % of number abundance and 36.1 % of volume abundance), followed by muscovite, biotite, and chlorite. Biotite and chlorite were partly weathered as shown in the loss of cations including K, Mg, and Fe. The other silicates were quartz (19.7 and 25.0 %), plagioclase (10.3 and 10.1 %), K-feldspar (5.2 and 4.4 %), and amphibole (0.9 and 0.8 %). Calcite was the major carbonate (6.7 and 5.9 %) with a minor dolomite content (1.2 and 0.4 %). The number and volume ratios of dolomite to calcite were about 0.18 and 0.06, respectively. Fe, Ti, and iron–titanium oxides were minor components in Asian dust with total content of about 1 %.

Mineral composition varied little throughout the four size bins (Table 2). The abundance of ISCMs decreased from the fine bin (44.1 %) to giant-L bin (33.6 %). However, increases
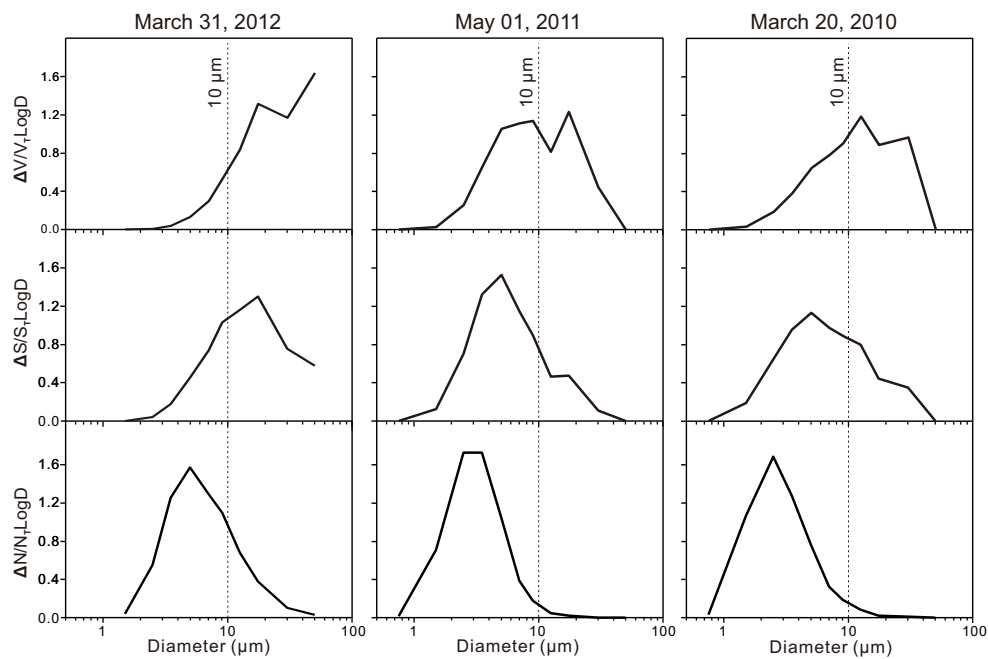
Fig. 3. Number, surface area, and volume–size distributions of three Asian dusts measured by scanning electron microscopy.

Table 3. Particle number, surface area, and volume contributions of four size bins to major minerals in the Asian dust TSP collected on 31 March 2012 (unit in %).

Mineral	Number					Area					Volume				
	F[2]	C	GS	GL	Sum	F	C	GS	GL	Sum	F	C	GS	GL	Sum
Phyllosilicates															
Total	40.0	40.8	16.0	3.1	100	4.6	24.4	38.8	32.2	100	2.2	10.8	29.9	57.1	100
ISCMs[1]	40.6	40.4	16.3	2.7	100	5.0	25.8	42.0	27.1	100	2.6	12.2	33.9	51.3	100
Kaolinite	60.3	27.9	7.4	4.4	100	3.7	12.5	15.4	68.5	100	1.4	4.0	8.5	86.2	100
Muscovite	19.0	52.4	21.4	7.1	100	1.4	22.5	22.0	54.1	100	0.4	7.3	11.9	80.3	100
Chlorite	35.6	48.5	12.9	3.0	100	6.1	33.0	40.5	20.4	100	3.0	16.9	44.1	36.0	100
Biotite	30.1	42.2	20.5	7.2	100	2.4	16.1	35.4	46.1	100	1.1	6.5	25.5	66.9	100
Other silicates															
Quartz	36.6	40.2	19.5	3.7	100	3.8	22.2	41.1	32.8	100	1.5	8.6	26.9	63.0	100
Plagioclase	35.6	43.1	18.0	3.4	100	3.7	21.9	38.2	36.2	100	1.9	11.6	43.8	42.6	100
K-feldspar	38.9	32.2	24.8	4.0	100	4.8	18.6	54.4	22.2	100	2.5	9.4	52.2	35.9	100
Amphibole	36.0	36.0	20.0	8.0	100	5.5	22.0	33.4	39.0	100	2.1	11.6	28.3	58.0	100
Non-silicates															
Calcite	43.2	37.0	16.1	3.6	100	5.1	23.5	43.0	28.3	100	2.4	10.7	39.2	47.7	100
Dolomite	65.7	25.7	8.6	0.0	100	13.0	34.0	52.9	0.0	100	9.9	19.8	70.4	0.0	100
Iron oxides	68.9	20.0	11.1	0.0	100	15.7	26.6	57.7	0.0	100	11.6	16.5	71.9	0.0	100
Sum	40.2	39.4	17.1	3.3	100	4.5	23.3	40.3	31.8	100	2.1	10.3	32.3	55.2	100

[1] Illite–smectite series clay minerals (illite, smectite, and their mixed layers).
[2] F is fine ($<5\,\mu m$), C is coarse (5–$10\,\mu m$), GS is giant-S (10–$20\,\mu m$), and GL is giant-L ($>20\,\mu m$).

in muscovite and biotite contents result in little variation of total phyllosilicate content over the size bins. Quartz content increased from 17.7 to 28.5 %. The fine size bin was relatively enriched with trace minerals, such as iron oxides, titanium oxides, dolomite, and gypsum.

The contributions of size bins to the number, surface area, and volume of each mineral or mineral group are listed in Table 3. Their variations with minerals were not significant regardless of number, surface area, and volume. Giant particles accounted for 70–75 % of the volume of mineral and

Table 4. Mineral number compositions of Asian dust TSPs collected on 1 May 2011 and 20 March 2010 (%).

Mineral	2011 ($n =981$)	2010 ($n =953$)
Phyllosilicates		
Total	59.2	60.3
ISCMs[1]	48.2	49.4
Kaolinite	1.6	1.7
Muscovite	0.3	0.9
Chlorite	4.5	5.7
Biotite	4.6	2.4
Talc	0.0	0.2
Other silicates		
Quartz	16.8	16.9
Plagioclase	10.5	10.0
K-feldspar	4.3	3.0
Amphibole	0.6	0.4
Pyroxene	0.0	0.0
Titanite	0.0	0.0
Zoisite	0.4	0.2
Non-silicates		
Calcite	5.8	5.7
Dolomite	0.2	0.9
Iron oxides	0.6	0.8
Fe–Ti oxides	0.1	0.3
Ti oxides	0.2	0.1
Gypsum	0.7	1.1
Barite	0.1	0.0
Pyrite	0.2	0.0
Apatite	0.1	0.3

* Illite, smectite, and illite–smectite mixed-layer clay minerals.

mineral groups, while the volume contribution of the fine size bins was usually < 3 %, e.g., the contribution of giant size bins to ISCM content was 85.2 % on a volume basis, but only 2.7 % on a number basis. However, the contributions of fine size bins to the volumes of dolomite (9.9 %) and iron oxides (11.6 %) were higher than those of other minerals.

Mineral number compositions in the 2010 and 2011 dusts were similar to the compositions of 2012 dust (Table 4). However, the 2010 and 2011 dusts were more enriched with ISCMs by about 10 % compared with the 2012 dust.

4.3 Microtextures and submicron mineralogy of giant particles

The surface details of giant-L particles were imaged using high-resolution SEM. Quartz (Fig. 4a, b) and plagioclase (Fig. 4c) have surface coatings of micron- to submicron-sized fine clay platelets. Calcite nanofibers were closely associated with clay minerals as cross-linked intergrowth (Fig. 4a, b) or single fibers on the surfaces of clay platelets (Fig. 4c). Fine clay platelets agglomerated to form giant clayey particles (Fig. 4d, e). Cross-linked intergrowth of calcite nanofibers was also found in the interstices of clayey agglomerates

(Fig. 4d, e). Some coarse kaolinite was present with coatings of calcite nanofibers (Fig. 4f), resulting in enhanced kaolinite content in the giant-L size bin (Table 2).

TEM images of the FIB slice of the clayey agglomerate giant particle in Fig. 4e showed a fine-scale agglomeration of ISCMs with submicron grains of quartz, K-feldspar, and chlorite (Fig. 5a1). Lattice-fringe imaging of the ISCMs showed the basal spacings of ca. 1.0–1.2 nm (Fig. 5a2). Nanofiber calcite grains of elongated morphology were closely admixed with the ISCM clays in a submicron scale (Fig. 5a3, 5a4). The lattice fringe of ca. 0.3 nm (Fig. 5a5) and EDX spectrum (Fig. 5a6) confirmed calcite. TEM image of the FIB slice of the quartz particle in Fig. 4b showed thin ISCM clay layers (ca. 1 μm thickness) covering quartz grain (Fig. 5b1, 5b2). The ISCMs contain a high amount of Fe (Fig. 5b3). The range of Fe content (8 analyses) of ISCMs determined by EDXS was ca. 3–14 w/w % (average 7 w/w %). Although the dominant clay minerals were ISCMs (Fig. 5b4), kaolinite and chlorite were also admixed as shown in the lattice fringes of 0.7 and 1.4 nm, respectively (Fig. 5b5, 5b6).

5 Discussion

5.1 Comparison of SEM particle sizes to optical particle counter data

SEM images and particle-size data indicated relatively coarse characteristics of the 2012 dust, compared with 2010 and 2011 dust. Particle-size data measured from SEM images were compared with real-time data produced with an optical particle counter (OPC) (GRIMM Aerosol Technik Model 180) at the Korea Meteorological Administration Asian dust monitoring station in Seoul. The OPC reports particle numbers over 30 size bins from 0.25 to 32 μm. The coarse characteristics of the 2012 dust were confirmed by the volume distributions of three Asian dusts measured using OPC (Fig. 6). The volume distributions of the 2012 dust revealed almost monotonic increase toward larger sizes, while distributions of 2010 and 2011 dusts had modes of around 3 μm. The volume portions of giant particles were 64, 8, and 39 % in 2012, 2011, and 2010 dusts, respectively, while those derived from SEM measurements were 89, 43, and 61 %, respectively.

The orders of enrichment of giant particles were consistent in both SEM and OPC measurements, with highest concentration in the 2012 dust and lowest concentration in the 2011 dust. However, the OPC data were shifted toward fine sizes relative to SEM data. Reid et al. (2003) observed similar features in comparison between SEM and aerodynamic particle size data for Saharan dust. The differences are attributed to assumptions made for SEM measurements, measurement objects, or site-specific factors between sampling and OPC installation site. SEM measurements assume spheroidal dust particle morphology. The actual morphology
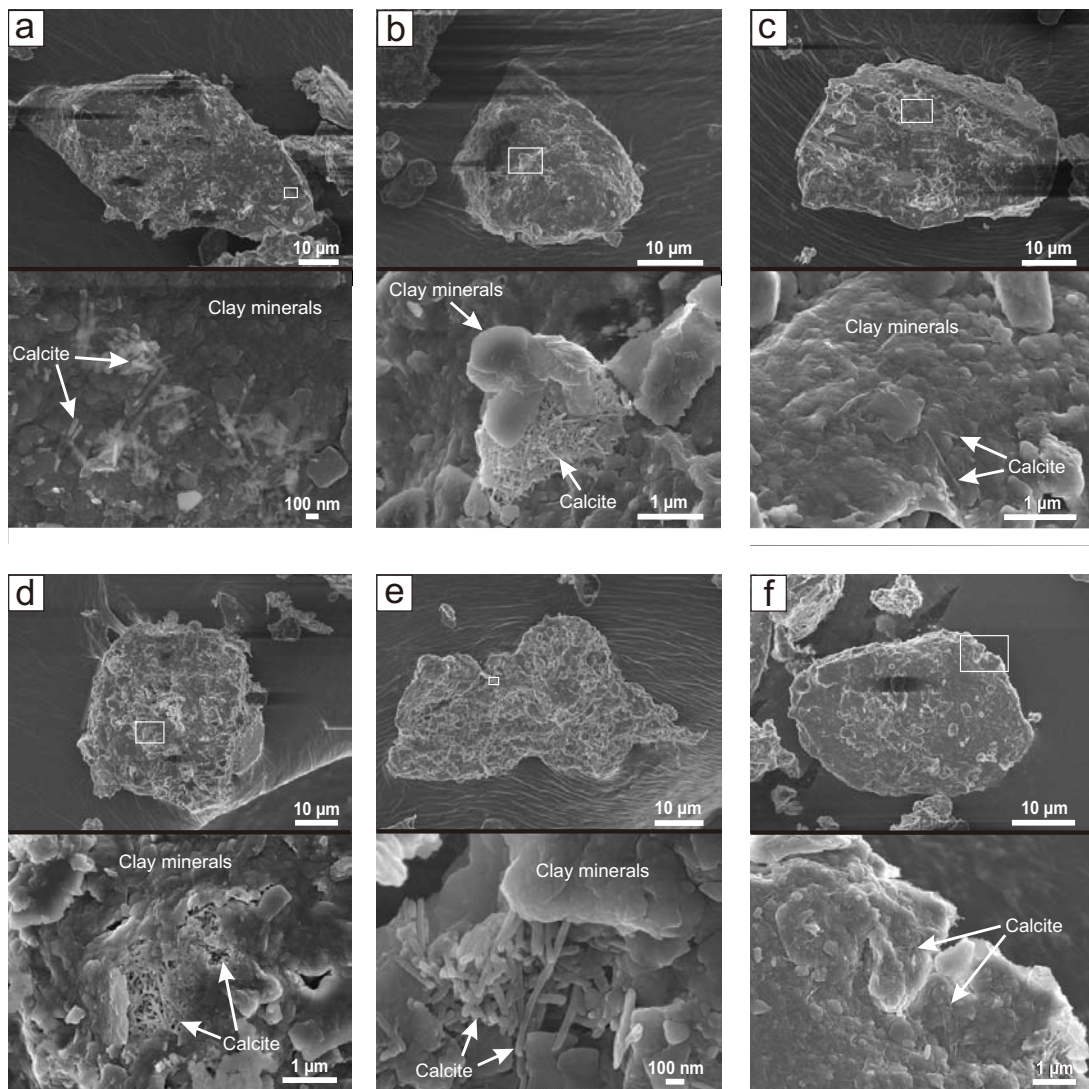
Fig. 4. High-resolution SEM images of the surfaces of giant-L dust particles. Bottom image was magnified from the box in the upper image. **(a, b)** Quartz particles coated with thin layers of clay platelets and intergrowth of calcite nanofibers. **(c)** Plagioclase coated with thin layers of clay platelets and calcite nanofibers. **(d, e)** Agglomerates of clay platelets with intergrowths of calcite nanofibers. **(f)** Kaolinite with calcite nanofibers.

of many particles is not spheroidal but is better approximated as an ellipsoid of which the longer axes are parallel to the filter surface. We have no information regarding the third shortest dimension and therefore the actual diameters would be smaller than those measured by SEM. The OPC cannot distinguish mineral particles from biogenic, marine, and pollutant particles. However, our SEM measurements excluded sea salt and most submicron particles of organic/inorganic pollutants and soot. The volume of giant-L size particles increased markedly in the OPC data for 2010 dust (Fig. 6). This is possibly due to the presence of coarse non-mineral particles, such as pollens, which cannot be distinguished by OPC. However, plants flowering in March are rare around the sampling site (Seoul). Thus, the OPC volume distribution in-

dicates the coarser characteristics of the 2010 dust in Seoul, compared with the SEM size distribution in Andong.

The population of giant particles in the 2012 dust was larger than those in 2011 and 2010 dusts. SEM analysis of single particles enabled determination of mineralogy, chemistry, and size distribution of coarse mineral dust, distinguishing them from non-mineral particles. Combined application of SEM and the wide-ranging particle counter installed at the same sampling site optimizes systematic characterization of mineral dusts laden with large particles.
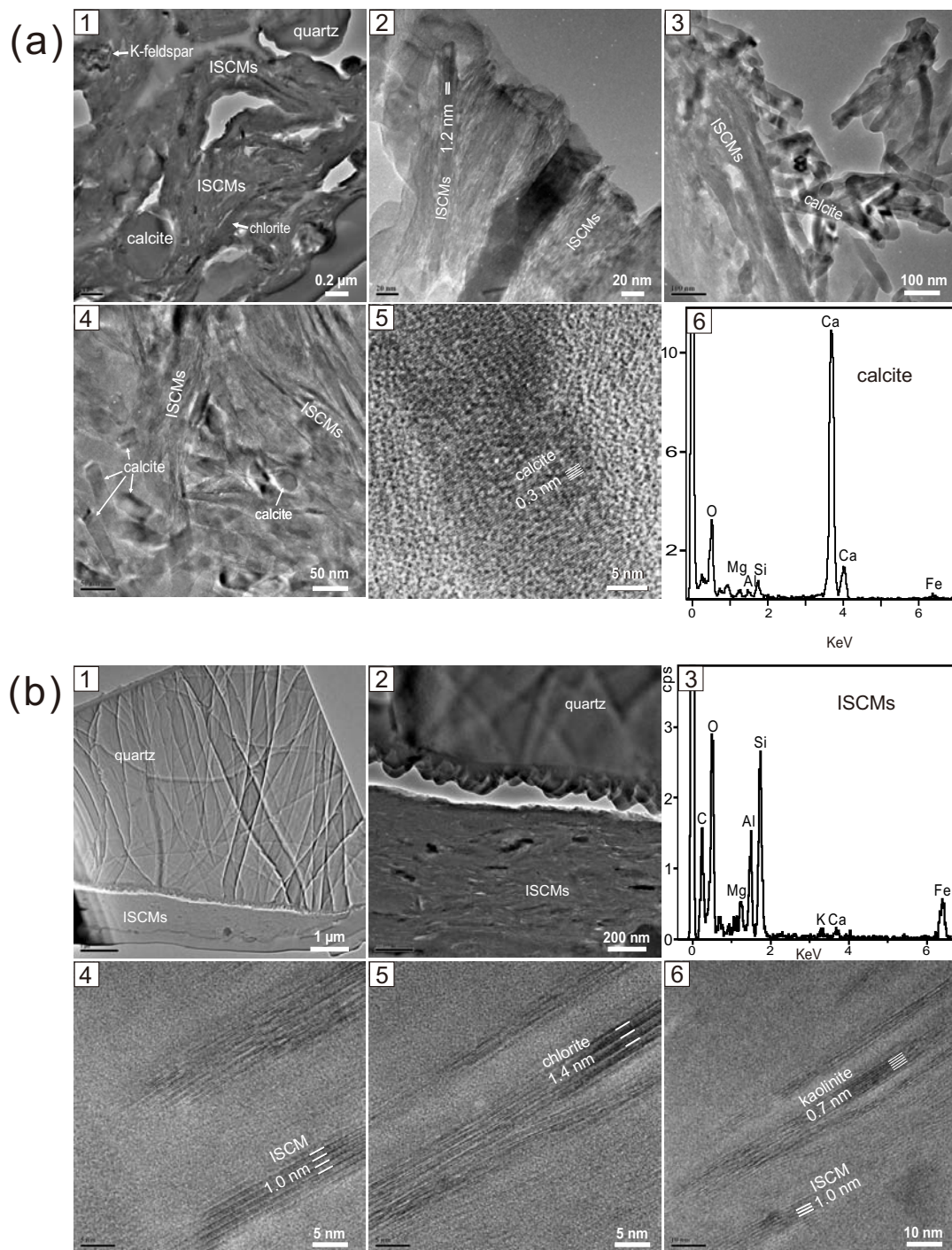
Fig. 5. TEM microtextures and lattice fringe images of giant dust particles with EDX spectra. **(a)** FIB slice of the clayey agglomerate dust particle in Fig. 4e. **(b)** FIB slice of the quartz dust particle in Fig. 4b.

5.2 Mineral compositions and particle sizes

Fine clay minerals (ISCMs) consistently decreased in the larger size bins with general increases in quartz, plagioclase, biotite, and muscovite (Table 2). Concentrations of quartz, plagioclase, biotite, and muscovite in the giant-L size bin were related to their usual occurrence in coarse-grained igneous and metamorphic bedrocks. Despite these mineralogical variations, the mineral compositions were highly uniform from fine to giant-L particles as shown by the large ISCM volume of the giant-L size bin (33.6 %). This was primarily
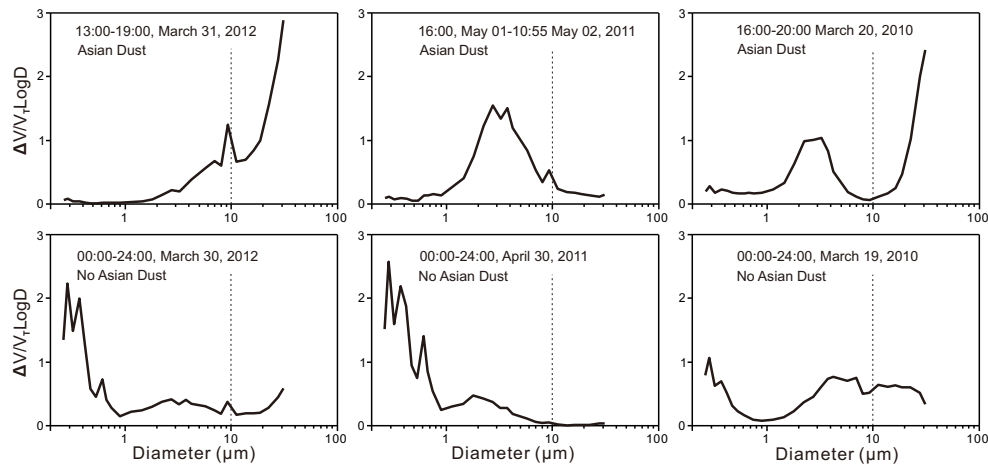
Fig. 6. Volume–size distributions of three Asian dusts measured with an optical particle counter at the Korea Meteorological Administration Asian dust monitoring station in Seoul, compared with those of non-Asian dust days. Dust event periods in Korea Standard Time.

attributed to the occurrence of large agglomerates of fine clay minerals (Fig. 4d, e) and thin coatings on large quartz and feldspar grains (Figs. 4a–c). ISCMs were the most common mineral group throughout all the size bins, even the giant-L size bin (Table 2). Thus, most of the volume (mass) of fine clay minerals was transported in the form of giant particles. Giant-S and giant-L particles contained 34 and 51 % of the ISCMs, respectively (Table 3).

5.3 Nanoscale evidence of the remote origin of giant particles

The size of dust particles transported over 1000 km is generally below 10 μm (Tegen and Lacis, 1996). Giant particles are normally transported and deposited over short distances of a few hundred kilometers (Pye, 1995). Thus, it is difficult to determine whether giant dust particles, particularly at sites on land that are distant from the source, are remote or local. Previous studies at sites on land suggested that Asian dust particles > 10 μm may have been derived from local sources (Chun et al., 2001). The origin of giant dust particles can be confirmed from the nanoscopic features acquired during the chemical weathering in source soils.

Minerals in soils are subjected to chemical weathering. Primary minerals derived from the erosion of rocks are unstable and dissolved by reacting with soil solutions, while secondary minerals are crystallized, depending on their solubility. The intensity of chemical weathering is largely dependent upon annual precipitation and temperature, ranging from the least weathering of primary minerals in arid soils to complete decomposition in tropical soils. The stability of minerals against chemical weathering is very diverse (Brady, 1990), e.g., on the Chinese loess plateau along the climatic gradients, primary minerals were sequentially weathered in a progressive fashion with increasing annual precipitation eastward in the order of calcite, dolomite, biotite, illite, chlorite,

amphibole, and plagioclase (Jeong et al., 2011). Calcite is more susceptible to chemical weathering than other major primary minerals. Thus, even in arid environments, coarse primary calcite in soils could react with water supplied by intermittent rain or melt water. However, leached Ca^{2+} ions are rapidly reprecipitated to form secondary calcites in soils due to high evaporation rates.

The average content of primary calcite in the western Jiuzhoutai loess was about 11.7 % (Jeong et al., 2008). Thus, calcite dissolution and reprecipitation are the major weathering processes in the arid soils of Asian dust sources. The morphological characteristics of secondary calcite are greatly different from those of primary calcite. One of the major forms of secondary calcite is a nano-sized fiber in comparison to micron-sized irregular primary calcite (Jeong and Chun, 2006; Jeong, 2008; Jeong et al., 2011). In the desert sands and loess silts of Asian dust sources, these nanofibers occurred only in samples containing coarse primary calcite particles derived from rocks, indicating that the primary calcite particles were partly dissolved during the occasional rainfalls, and reprecipitated as nanofibers from evaporating soil solutions (Jeong and Chun, 2006).

The precipitation of nanofiber calcites from soil solutions results in the pervasive infilling of the interstices of coarser soil particles, together with submicron clay minerals. Thus, the surfaces of the source soil particles are commonly associated with calcite nanofibers scattered individually or forming their own clusters (Jeong and Chun, 2006). The agglomerates of clay and nanofibers, or the particles of quartz, K-feldspar, and plagioclase with clay and nanofiber coatings, were then blown to form Asian dust. Thus, calcite nanofibers associated with giant particles (Figs. 4, 5a) are the nanoscopic features of Asian dust particles blown from remote arid sources. However, secondary calcite is absent from the aeolian deposits of Korea (Jeong et al., 2013). This suggests a complete

leaching of calcite in the acidic soils of Korea under humid climate conditions compared with the calcareous arid soils in the Asian dust sources. Thus, the common presence of calcite nanofibers associated with giant dust particles (Fig. 4) provides the direct evidence of their long-range transport.

The mineral particles collected on the central North Pacific, north of Hawaii, by Betzer et al. (1988) were exceptionally large ($> 75\,\mu m$), and can be called ultragiant particles. They suggested that the particles were transported over 10,000 km from Asian sources using backward trajectory. However, the Asian desert origin of the ultragiant particles is required to be further confirmed by observing the nanoscopic features such as nanofiber calcite.

Díaz-Hernández and Párraga (2008) reported pinkish mineral microspherulites referred to as iberulites deposited on the southern Iberian Peninsula. The microspherulites are giant particles with a common size range of 60–80 μm. They were formed by the evaporation of cloud water droplets that collided with Saharan dust particles. Thus, the cloud processing is a possible mechanism of the formation of giant dust particles. However, iberulite is characterized by high sphericity, high porosity (a bulk density of $0.65\,\mathrm{g\,cm^{-3}}$), vortex depression, and coarse internal agglomeration grading to fine, thin clay rinds. The irregular giant particles in this study lack the microscopic features of iberulite. They were not the results of cloud processing, but directly transported from the Gobi Desert sources.

5.4 Synoptic conditions of Asian dust laden with giant particles

Since it was revealed that the extraordinary high fraction of giant particles in 2012 Asian dust was the result of long-range transport from the source region rather than local origin, we investigated the synoptic meteorological conditions compared with 2011 and 2010 dust events.

Aerosol index images from the COMS satellite revealed that the outbreak regions, migration routes, and transport distances of the three dusts were almost identical: the Gobi Desert of southern Mongolia and northern China (40°–46° N, 90°–110° E) (Fig. 1). However, the flight time of the 2012 dust was relatively short (28 h) while those of 2011 and 2010 dusts were 45 and 35 h, respectively.

Asian dust incursions in Korea are closely associated with synoptic conditions over dust source regions 2–3 days earlier (Chun et al., 2001; Kim et al., 2010). For example, Chun et al. (2001) showed that a strong pressure gradient with strong baroclinic instability at 850 hPa (about 1.5 km level) over the dust source region is associated with outbreaks of Asian dust in spring. Such strong pressure gradients behind the developing low-pressure system result in high surface wind speeds, which are necessary for dust uplift (Husar et al., 2001). In addition, the strong wind belt in the mid-troposphere is closely related to dust migration. Thus, the dust arrival is much faster

if the strong wind belt at 500 hPa (about 5 km) stretches directly to Korea (Chun et al., 2001).

To examine the synoptic conditions related to the outbreak and migration of dust, we used daily mean of the geopotential height and temperature at 850 hPa, wind speed at 500 hPa, and 10 m wind speed (as a proxy for the surface wind conditions) derived from the European Centre for Medium-Range Weather Forecasts Reanalysis Interim (ERA-Interim) data. We also used the ultraviolet (UV) aerosol index obtained from the Ozone Monitoring Instrument (OMI) onboard the EOS Aura satellite to identify the intensity and locations of the dust. The OMI UV-aerosol index provides qualitative information on the presence of UV-absorbing aerosols such as desert dust or smoke, without interference by ice, snow, and clouds (Ahn et al., 2008).

The 2012 dust event showed unusual characteristics. The intensity of dust at the source region was much weaker, but the transport was much faster than the previous events, even though the dust source regions in the Gobi Desert were almost identical. The meteorological characteristics of the 2012, 2011, and 2010 dust events are shown in Fig. 7. During both the 2010 and 2011 dust events, strong pressure gradients associated with strong baroclinic instability at 850 hPa were observed over the Gobi Desert on 19 March 2010, and 29 April 2011 (Fig. 7). The strong pressure gradients resulted in a high surface wind speed ($> 12\,\mathrm{m\,s^{-1}}$) over the dust source region and thus induced severe dust storms. The dust-laden air mass followed the eastward-moving low-pressure systems and took about 1.5–2 days to reach Korea on both occasions. Despite the similar mechanisms of dust generation and transport in both events, the transport speed was slower, and the duration for which the dust persisted was longer during the 2011 event than the 2010 event because of the lower wind speed at 500 hPa and stagnant atmospheric conditions associated with a high-pressure system over China. This is consistent with the number and volume proportions of giant particles slightly higher in the 2010 event.

During the 2012 dust event, a strong pressure gradient over the Gobi Desert appeared ahead of an expanding high-pressure system over central China on 30 March 2012 (Fig. 7). However, the strong pressure gradient was relatively weak compared with typical dust events. The weak baroclinicity on the boundary of the anticyclone induced a relatively low surface wind speed ($\sim 8\,\mathrm{m\,s^{-1}}$) over the dust source region and hence resulted in a weak dust event. The synoptic conditions during the 2012 event were similar to the typical winter synoptic conditions produced by anticyclones over the continent and cyclones in the east. Between the high and low pressure systems, the contour lines of the 850 hPa geopotential height and 500 hPa strong wind belt were stretched directly southeastward from the Gobi Desert to Korea. These peculiar meteorological characteristics ensured much faster migration of dust and resulted in the extraordinary delivery of abundant giant particles to Korea during the 2012 dust event, even though the dust intensity was relatively weak.
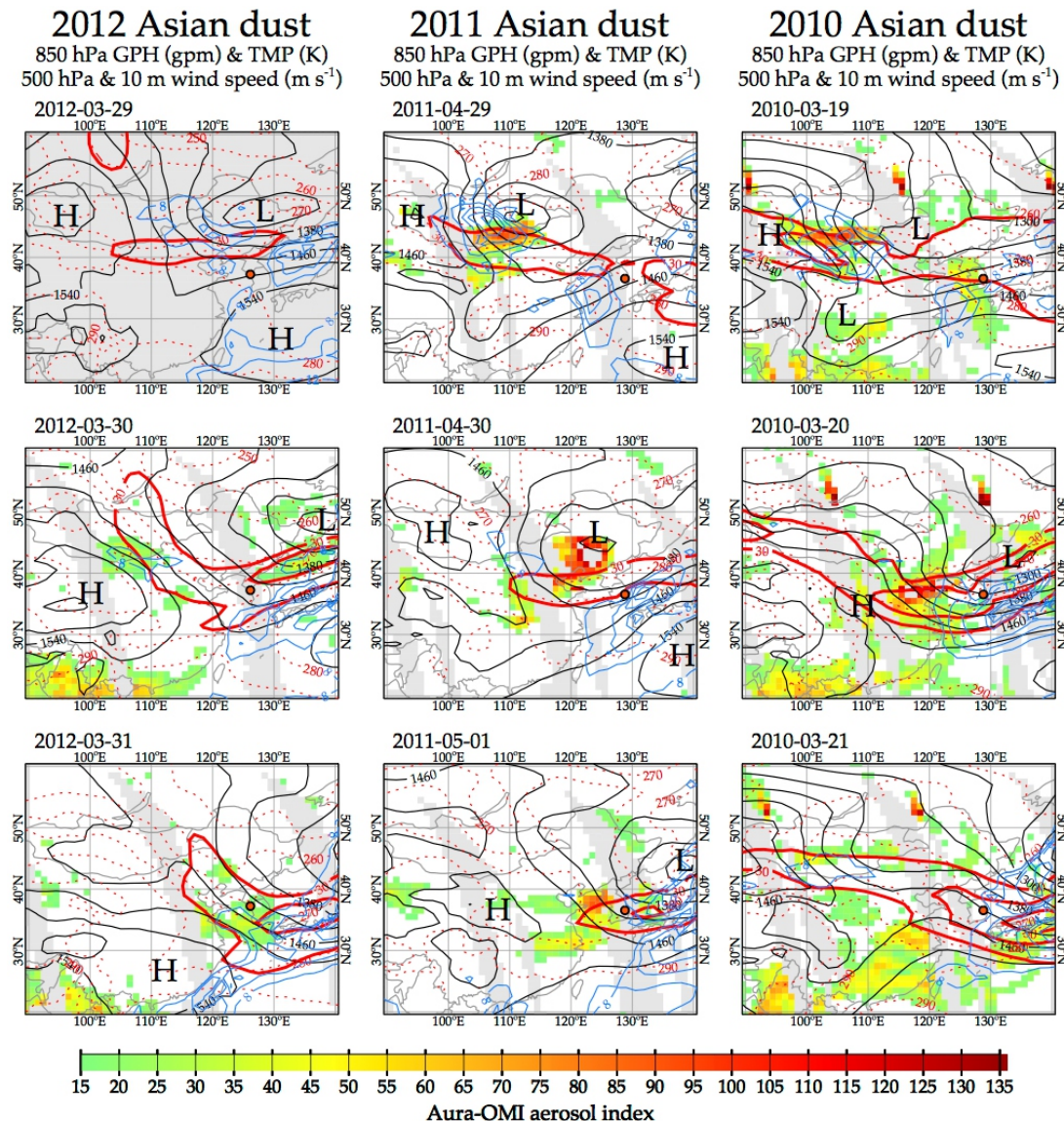
Fig. 7. Daily evolution of the 2010, 2011, and 2012 dust events with ERA-Interim daily meteorological fields superimposed on an Aura-OMI aerosol index over East Asia. Black solid lines and red dotted lines represent the 850 hPa geopotential height (gpm) and temperature (K). Blue thin solid lines and red thick solid lines indicate 10 m wind speed above 8 m s^{-1} and 500 hPa wind speed above 30 m s^{-1}, respectively. The solid orange circles are the TSP sampling sites. Missing values of the OMI aerosol index are shown in light gray color.

The mechanism of the long-range transport of giant particles of several tens of micrometers over several thousands of kilometers is unclear so far (Betzer et al., 1988; Goudie and Middleton, 2001). Giant particles could be transported over long distances when strong upward advection of air masses lifts dust particles to higher altitudes (Windom, 1985; Pye, 1995). Betzer et al. (1988) suggested a resuspension mechanism in the isolated storm along the particles' path. In the 2012 dust event, the dust outbreak and migration are accompanied by a locally strong updraft of 0.09 m s^{-1} at 700 hPa (about 3 km level) until its arrival over the Yellow Sea (figure not shown). If we assumed a sand-like irregu-

lar shaped giant particle with a diameter of 50 μm and density of 2.3 g cm^{-3}, its settling velocity reaches approximately 0.11 m s^{-1} or 9.5 km day^{-1} (Reid et al., 2003). However, the local updraft can significantly reduce the settling velocity, and this mechanism with the fast migration of the 2012 dust event is physically consistent with the transport of the giant particles over the long distance of 2000 km.

5.5 Ancient records of giant Asian dust particles in Korea

The enormous volume of giant particles suggests that deposition of Asian dust would occur near the dust source like in the Chinese Loess Plateau. However, they also contributed to the formation of an aeolian sedimentary body in remote environments.

The particle size and morphology of quartz and feldspars in ancient aeolian sediments (Fig. 2d) in the Paleolithic excavation sites of Korea (Shin et al., 2004; Jeong et al., 2013) are markedly similar to the 2012 dust (Fig. 2a). The origin of the fine clays forming the matrix enclosing quartz and feldspar particles is unknown. However, the common occurrence of giant clay agglomerates in the 2012 dust (Table 2 and Fig. 4d, e) suggests that even the fine clays in the sediments (Fig. 2d) were also derived from giant clay agglomerates. The original morphology and size of clay agglomerates in Asian dust may have been altered by post-depositional pedogenic activity. Thus, the long-term deposition of giant particles through the late Quaternary likely represents major terrestrial input of minerals from long-range transported dust to form an aeolian sedimentary body in East Asia.

The giant particles of ancient Asian dust contributed to the far and remote sedimentary body out of the Asian region. Betzer et al. (1988) suggested the recent anthropogenic disturbance as the cause of the giant dust particles delivered to the North Pacific because giant particles are rare in the deep-sea sediment core of the North Pacific. However, Beget et al. (1993) reported quartz particles as large as 40–60 μm in the late Quaternary tephric loess deposits on the island of Hawaii. There is evidence supporting the long-range transport of large particles, as summarized in Goudie and Middleton (2001), e.g., quartz grains of up to 90 μm in diameter on Sal Island (Cape Verde Islands) off West Africa (Glaccum and Prospero, 1980) and particles > 20 μm in diameter transported 4000 km from their Saharan source (Prospero et al., 1970). Thus, mass contribution of giant particles to the terrestrial and ocean sediments may have been higher than previously thought at least on a regional scale.

5.6 Transport of reactive minerals and nutrients

Iron dissolved from dust particles is important in Fe-deficient marine ecosystems of high-nutrient, low-chlorophyll regions, such as the eastern subarctic North Pacific and the Southern Ocean (Boyd et al., 2004). Fine clay minerals and nanofiber calcite with a large surface area and cation exchange capacity are sensitive minerals that react with acidic gases/droplets and organic/inorganic pollutants. The major form of clay minerals and nano-sized calcites transported are giant clay agglomerates, as revealed by SEM analyses, which showed that giant particles accounted for 89 % of the total volume of the 2012 dust. Mineral dusts supply inorganic nutrients to remote sea locations. The settling rates of giant particles are higher than fine particles. Important inorganic nutrients (e.g., Fe) are associated with fine particles such as Fe-bearing clay minerals and iron oxides. TEM imaging and EDX spectroscopy of individual clay grains of the Asian dusts and their deposits (Chinese loess) showed that ISCMs contain ca. 5–7 % of Fe (Jeong, 2008; Jeong et al., 2008, 2011; this study). About 85 % (vol.) of ISCMs are included in the giant agglomerate particles (Table 3, Fig. 4d, e). Large clay agglomerates are a major source of inorganic nutrients in some regions of the ocean, in comparison to fine particles with a slow settling velocity and long residence time.

6 Summary and conclusions

Particle size, mineralogy, and meteorological characteristics of the Asian dust event on 31 March 2012, were investigated and compared with two previous events in 2010 and 2011. The median equivalent sphere diameters from the number size distributions were 5.7, 2.9, and 2.5 μm in the 2012, 2011, and 2010 dust events, respectively, and were consistent with independent OPC data. Twenty percent of the particles in the 2012 dust event were giant (giant-S and giant-L) particles, with a maximum size of 60 μm. They contributed 89 % of the total dust volume in the 2012 dust and were either agglomerates of submicron clay minerals, or large quartz and feldspar grains with clay-mineral coatings. The occurrence of calcite nanofibers associated with giant particles confirmed their long-range transport from remote arid sources. Illite–smectite series clay minerals were the major mineral group followed by quartz, plagioclase, K-feldspar, and calcite. Mineral compositions showed little variation through the fine, coarse, giant-S, and giant-L size bins because the fine clay minerals formed larger agglomerates. Mineral compositions varied little through the three dust events, but fine clay minerals were more common in the 2010 and 2011 dusts. The particle-size characteristics of the mineral dust may be dependent on the synoptic conditions of the dust outbreak and migration. During the 2012 Asian dust event, a mid-tropospheric strong wind belt stretched southeastward from the Gobi Desert to Korea, making the rapid migration of dust possible, and delivering abundant giant particles. Atmospheric aerosol studies usually focus on particles < 10 μm. However, the role of giant particles should be reviewed with regard to the regional circulation of earth materials through the lithosphere, pedosphere, and atmosphere. For example, analysis of ancient aeolian deposits in Korea suggested the common deposition of giant particles from Asian dust through the Quaternary Period.

Acknowledgements. This work was supported by the National Research Foundation of Korea grant NRF–2011–0028597. We thank Mihály Posfai and three anonymous referees for their thoughtful comments.

Edited by: X. Querol

References

Ackerman, S. A.: Remote sensing aerosols using satellite infrared observations, J. Geophys. Res.-Atmos., 102, 17069–17079, 1997.

Ahn, C., Torres, O., and Bhartia, P. K.: Comparison of ozone monitoring instrument UV aerosol products with aqua/moderate resolution imaging spectroradiometer and multiangle imaging spectroradiometer observations in 2006, J. Geophys. Res.-Atmos., 113, D16S27, doi:10.1029/2007JD008832, 2008.

Arimoto, R., Ray, B. J., Lewis, N. F., and Tomza, U.: Mass-particle size distributions of atmospheric dust and the dry deposition of dust to the remote ocean, J. Geophys. Res.-Atmos., 102, 15867–15874, 1997.

Beget, J. E., Keskinen, M., and Severin, K.: Mineral particles from Asia found in volcanic loess on the island of Hawaii, Sediment. Geol., 84, 189–197, 1993.

Betzer, P. R., Carder, K. L., Duce, R. A., Merrill, J. T., Tindale, N. W., Uematsu, M., Costello, D. K., Young, R. W., Feely, R. A., Breland, J. A., Bernstein, R. E., and Greco, A. M.: Long-range transport of giant mineral aerosol particles, Nature, 336, 568–571, 1988.

Blanco, A., De Tomasi, F., Filippo, E., Manno, D., Perrone, M. R., Serra, A., Tafuro, A. M., and Tepore, A.: Characterization of African dust over southern Italy, Atmos. Chem. Phys., 3, 2147–2159, doi:10.5194/acp-3-2147-2003, 2003.

Boyd, P. W., Law, C. S., Wong, C. S., Nojiri, Y., Tsuda, A., Levasseur, M., Takeda, S., Rivkin, R., Harrison, P. J., Strzepek, R., Gower, J., McKay, R. M., Abraham, E., Arychuk, M., Barwell-Clarke, J., Crawford, W., Hale, M., Harada, K., Johnson, K., Kiyosawa, H., Kudo, I., Marchetti, A., Miller, W., Needoba, J., Nishioka, J., Ogawa, H., Page, J., Robert, M., Saito, H., Sastri, A., Sherry, N., Soutar, T., Sutherland, N., Taira, Y., Whitney, F., Wong, S. -K. E., and Yoshimura, T.: The decline and fate of an iron-induced subarctic phytoplankton bloom, Nature, 428, 549–553, doi:10.1038/nature02437, 2004.

Bradley, R. S.: Paleoclimatology: Reconstructing Climates of the Quaternary, Academic Press, 1999.

Brady, N. C.: The Nature and Properties of Soils, Macmillan Publishing Company, New York, 1990.

Chaboureau, J. -P., Tulet, P., and Mari, C.: Diurnal cycle of dust and cirrus over West Africa as seen from Meteosat Second Generation satellite and a regional forecast model, Geophys. Res. Lett., 34, L02822, doi:10.1029/2006GL027771, 2007.

Chun, Y., Boo, K.-O., Kim, J., Park, S. -U., and Lee, M.: Synopsis, transport, and physical characteristics of Asian dust in Korea, J. Geophys. Res.-Atmos., 106, 18461–18469, 2001.

Chun, Y., Lim, J.-Y., and Choi, B. -C.: The features of aerosol in Seoul by Asian dust and haze during springtime from 1998 to 2002, J. Korean Meteorol. Soc., 39, 459–474, 2003.

Coude-Gaussen, G., Rognon, P., Bergametti, G., Gomes, L., Strauss, B., Gros, J. M., and Le Coustumer, M. N.: Saharan dust on Fuerteventura Island (Canaries): Chemical and mineralogical characteristics, air mass trajectories, and probable sources, J. Geophys. Res.-Atmos., 92, 9753–9771, 1987.

Dentener, F. J., Carmichael, G. R., Zhang, Y., Lelieveld, J., and Crutzen, P. J.: Role of mineral aerosol as a reactive surface in the global troposphere, J. Geophys. Res.-Atmos., 101, 22869–22889, 1996.

Díaz-Hernández, J. L., and Párraga, J.: The nature and tropospheric formation of iberulites: Pinkish mineral microspherulites, Geochim. Cosmochim. Acta, 72, 3883–3906, 2008.

Dockery, D. W., Pope, C. A., Xu, X., Spengler, J. D., Ware, J. H., Fay, M. E., Ferris Jr., B. G., and Speizer, F. E.: An association between air pollution and mortality in six US cities, New Engl. J. Med., 329, 1753–1759, 1993.

Fletcher, R. A., Ritchie, N. W. M., Anderson, I. M., and Small, J. A.: Microscopy and microanalysis of individual collected particles, in: Aerosol Measurement, edited by: Kulkarni, P., Baron, P. A., and Willeke, K., Wiley, printed in the USA, 179–232, 2011.

Ginoux, P.: Effects of nonsphericity on mineral dust modeling, J. Geophys. Res.-Atmos., 108, 4052, doi:10.1029/2002JD002516, 2003.

Glaccum, R. A. and Prospero, J. M.: Saharan aerosols over the tropical north Atlantic – Mineralogy, Mar. Geol., 37, 295–321, 1980.

Goudie, A. S. and Middleton, N. J.: Saharan dust storms: nature and consequences. Earth Sci. Rev., 56, 179–204, 2001.

Hong, S. J., Kim, J. H., and Ha, J. S.: Possibility of applying infrared background threshold values for detecting Asian dust in spring from geostationary satellite, Korean J. Remote Sens., 26, 387–394 (in Korean), 2010.

Husar, R. B., Tratt, D. M., Schichtel, B. A., Falke, S. R., Li, F., Jaffe, D., Gassó, S., Gill, T., Laulainen, N. S., Lu, F., Reheis, M. C., Chun, Y., Westphal, D., Holben, B. N., Gueymard, C., McKendry, I., Kuring, N., Feldman, G. C., McClain, C., Frouin, R. J., Merrill, J., DuBois, D., Vignola, F., Murayama, T., Nickovic, S., Wilson, W. E., Sassen, K., Sugimoto, N., and Malm, W. C.: Asian dust events of April 1998, J. Geophys. Res.-Atmos., 106, 18317–18330, 2001.

In, H. -J. and Park, S. -U.: A simulation of long-range transport of Yellow Sand observed in April 1998 in Korea, Atmos. Environ., 36, 4173–4187, 2002.

Jeong, G. Y.: Bulk and single-particle mineralogy of Asian dust and a comparison with its source soils, J. Geophys. Res.-Atmos., 113, D02208, doi:10.1029/2007JD008606, 2008.

Jeong, G. Y. and Chun, Y.: Nanofiber calcite in Asian dust and its atmospheric roles, Geophys. Res. Lett., 33, L24802, doi:10.1029/2006GL028280, 2006.

Jeong, G. Y. and Lee, K. -S: A mineral tracer toward high-resolution dust provenance on the Chinese Loess Plateau: SEM, TEM, and sulfur isotopes of sulfate inclusions in biotite, Am. Mineral., 95, 64–72, 2010.

Jeong, G. Y., Hillier, S., and Kemp, R. A.: Quantitative bulk and single-particle mineralogy of a thick Chinese loess–paleosol section: implications for loess provenance and weathering, Quaternary Sci. Rev., 37, 1271–1287, 2008.

Jeong, G. Y., Hillier, S., and Kemp, R. A.: Changes in mineralogy of loess–paleosol sections across the Chinese Loess Plateau, Quat. Res., 75, 245–255, 2011.

Jeong, G. Y., Choi, J. -H., Lim, H. S., Seong, C., and Yi, S. B.: Deposition and weathering of Asian dust in Paleolithic sites, Korea, Quat. Sci. Rev., 78, 283–300, 2013.

Kanayama, S., Yabuki, S., Yanagisawa, F., and Motoyama, R.: The chemical and strontium isotope composition of atmospheric aerosols over Japan: the contribution of long-range-transported Asian dust (Kosa), Atmos. Environ., 36, 5159–5175, 2002.

Kandler, K., Benker, N., Bundke, U., Cuevas, E., Ebert, M., Knippertz, P., Rodríguez, S., Schütz, L., and Weinbruch, S.: Chemical composition and complex refractive index of Saharan Mineral Dust at Izaña, Tenerife (Spain) derived by electron microscopy, Atmos. Environ., 41, 8058–8074, 2007.

Kim, S.-W., Yoon, S.-C., and Kim, J.: Columnar Asian dust particle properties observed by sun/sky radiometers from 2000 to 2006 in Korea. Atmos. Environ., 42, 492–504, 2008.

Kim, S.-W., Yoon, S. -C., Kim, J., Kang, J.-Y., and Sugimoto, N.: Asian dust event observed in Seoul, Korea, during 29–31 May 2008: Analysis of transport and vertical distribution of dust particles from lidar and surface measurements, Sci. Total Environ., 408, 1707–1718, 2010.

Korea Meteorological Administration (KMA): http://web.kma.go.kr/eng/weather/asiandust/timeseries.jsp (last access: 7 November 2013), 2013.

Laskin, A., Wietsma, T. W., Krueger, B. J., and Grassian, V. H.: Heterogeneous Chemistry of Individual Mineral Dust Particles with Nitric Acid: A Combined CCSEM/EDX, ESEM, and ICP-MS Study, J. Geophys. Res.-Atmos., 110, D10208, doi:10.1029/2004JD005206, 2005.

Legrand, M., Plana-Fattori, A., and N'doumé, C.: Satellite detection of dust using the IR imagery of Meteosat: 1. Infrared difference dust index, J. Geophys. Res.-Atmos., 106, 18251–18274, 2001.

McKendry, I. G., Macdonald, A. M., Leaitch, W. R., van Donkelaar, A., Zhang, Q., Duck, T., and Martin, R. V.: Trans-Pacific dust events observed at Whistler, British Columbia during INTEX-B, Atmos. Chem. Phys., 8, 6297–6307, doi:10.5194/acp-8-6297-2008, 2008.

Meskhidze, N., Chameides, W. L., and Nenes, A.: Dust and pollution: a recipe for enhanced ocean fertilization, J. Geophys. Res.-Atmos., 110, D03301, doi:10.1029/2004JD005082, 2005.

Mikami, M., Shi, G.Y., Uno, I., Yabuki, S., Iwasaka, Y., Yasui, M., Aoki, T., Tanaka, T.Y., Kurosaki, Y., Masuda, K., Uchiyama, A., Matsuki, A., Sakai, T., Takemi, T., Nakawo, M., Seino, N., Ishizuka, M., Satake, S., Fujita, K., Hara, Y., Kai, K., Kanayama, S., Hayashi, M., Du, M., Kanai, Y., Yamada, Y., Zhang, X. Y., Shen, Z., Zhou, H., Abe, O., Nagai, T., Tsutsumi, Y., Chiba, M., and Suzuki, J.: Aeolian dust experiment on climate impact: An overview of Japan–China joint project ADEC, Global Planet. Change, 52, 142–172, 2006.

Mori, I., Nishikawa, M., Tanimura, T., and Quan, H.: Change in size distribution and chemical composition of kosa (Asian dust) aerosol during long-range transport, Atmos. Environ., 37, 4253–4263, 2003.

National Meteorological Satellite Center: http://nmsc.kma.go.kr/html/homepage/en/main.do (last access: 7 November 2013), 2013.

Park, S.-U. and Kim, J. -W.: Aerosol size distributions observed at the Seoul National University campus in Korea during the Asian dust and non-Asian dust periods, Atmos. Environ., 40, 1722–1730, 2006.

Park, S.-U., Chang, L.-S., and Lee, E.-H.: Direct radiative forcing due to aerosols in East Asia during a Hwangsa (Asian dust) event observed on 19–23 March 2002 in Korea, Atmos. Environ., 39, 2593–2606, 2005.

Prospero, J. M., Bonatti, E., Schuber, C., and Carlson, T. N.: Dust in the Caribbean traced to an African dust storm, Earth Planet. Sci. Lett., 9, 287–293, 1970.

Pye, K.: The nature, origin and accumulation of loess, Quaternary Sci. Rev., 14, 653–667, 1995.

Reid, J. S., Jonsson, H. H., Maring, H. B., Smirnov, A., Savoie, D. L., Cliff, S. S., Reid, E. A., Livingston, J. M., Meier, M. M., Dubovik, O., and Tsay, S. C.: Comparison of size and morphological measurements of coarse mode dust particles from Africa, J. Geophys. Res., 108, doi:10.1029/2002JD002485, 2003.

Reist, P. C.: Aerosol Science and Technology, McGraw-Hill, New York, 1993.

Seinfeld, J. H. and Pandis, S. N.: Atmospheric Chemistry and Physics, John Wiley, Hoboken, NJ, 2006.

Seinfeld, J. H., Carmichael, G. R., Arimoto, R., Conant, W. C., Brechtel, F. J., Bates, T. S., Cahill, T. A., Clarke, A. D., Doherty, S. J., Flatau, P. J., Huebert, B. J., Kim, J., Markowicz, K. M., Quinn, P. K., Russell, L. M., Russell, P. B., Shimizu, A., Shinozuka, Y., Song, C. H., Tang, Y., Uno, I., Vogelmann, A. M., Weber, R. J., Woo, J. -H, and ZhanG, X. Y.: ACE-ASIA regional climatic and atmospheric chemical effects of Asian dust and pollution, B. Am. Meteorol. Soc., 85, 367–380, 2004.

Shi, Z., Shao, L., Jones, T. P., and Lu, S.: Microscopy and mineralogy of airborne particles collected during severe dust storm episodes in Beijing, China, J. Geophys. Res., 110, D01303, doi:10.1029/2004JD005073, 2005.

Shin, J.-B., Yu, K.-M., Naruse, T., and Hayashida, A.: Study on loess-paleosol stratigraphy of Quaternary unconsolidated sediments at E55S20-IV pit of Chongokni Paleolithic site, Journal of the Geological Society of Korea, 41, 369–381 (in Korean with English abstract), 2004.

Song, Y.-C., Eom, H. -J., Jung, H.-J., Malek, M. A., Kim, H. K., Geng, H., and Ro, C.-U.: Investigation of aged Asian dust particles by the combined use of quantitative ED-EPMA and ATR-FTIR imaging. Atmos. Chem. Phys., 13, 3463–3480, doi:10.5194/acp-13-3463-2013, 2013.

Sullivan, R. C., Moore, M. J. K., Petters, M. D., Kreidenweis, S. M., Roberts, G. C., and Prather, K. A.: Effect of chemical mixing state on the hygroscopicity and cloud nucleation properties of calcium mineral dust particles, Atmos. Chem. Phys., 9, 3303–3316, doi:10.5194/acp-9-3303-2009, 2009.

Tegen, I., and Lacis, A. A.: Modeling of particle size distribution and its influence on the radiative properties of mineral dust aerosol, J. Geophys. Res., 101, 19237–19244, 1996.

Weaver, C. E.: Clays, Muds, and Shales, Elsevier, Amsterdam, The Netherlands, 1989.

Westphal, D. L., Toon, O. B., and Carlson, T. N.: A two-dimensional numerical investigation of the dynamics and microphysics of Saharan dust storms, J. Geophys. Res., 92, 3027– 3049, 1987.

Windom, H. L.: Eolian contributions to marine sediments. J. Sediment. Petrol., 45, 520–529, 1985.

Available online at www.sciencedirect.com

ScienceDirect

Geochimica et Cosmochimica Acta 72 (2008) 3883–3906

Geochimica et Cosmochimica Acta

www.elsevier.com/locate/gca

The nature and tropospheric formation of iberulites: Pinkish mineral microspherulites

José L. Díaz-Hernández [a,*], Jesús Párraga [b]

[a] *IFAPA Camino de Purchil s/n, Consejería de Innovación, Ciencia y Empresa, Junta de Andalucía, Apartado 2027, 18080 Granada, Spain*
[b] *Departamento de Edafología y Química Agrícola, Universidad de Granada, Campus de Cartuja, 18071 Granada, Spain*

Received 22 June 2007; accepted in revised form 1 May 2008; available online 29 May 2008

Abstract

The circum-Mediterranean area has one of the highest dust accretion rates in the world. We have found pinkish mineral microspherulites (here referred to as iberulites), a new type of aerosol particle formed under special atmospheric conditions in periods corresponding to the highest levels of solid additions (summer). Because these particles are labile, they have gone unnoticed until now.

Image analysis shows that these particles are spherical in shape, most commonly 60–90 μm in diameter, and show a typical depression (vortex). Iberulites are considered complex mineral assemblages with different hygroscopic characteristics and also contain biological remains (plants, silica shells, plankton and probably viruses). Their bulk mineralogy includes silicates, carbonates, sulfates, halides, oxides and phosphate-vanadates. This mineralogical composition indicates that likely source areas are the Sahara and Sahel for primary minerals (inherited), while other minerals are the result of atmospheric neoformation (gypsum and alunite-jarosite).

We thus define an iberulite as a coassociation with axial geometry, constituted by well-defined mineral grains together with non-crystalline compounds, structured on a coarse-grained core and a smectite rind, with only one vortex and pinkish color, formed in the troposphere by complex aerosol–water–gas interactions.

We suggest the aqueous interphase hypothesis as the mechanism for tropospheric formation of iberulites, mainly in summer: interactions between water droplets and aerosols create complex hydrodynamic conditions, causing possible collisions (wake and front capture) that produce the "precursor water droplets" of iberulites. Atmospheric processing is required from this stage to iberulite maturation.

To date, we do not know to what extent these iberulites are present in time and space or whether they can serve as markers for environmental or paleoclimatic analyses or even lead to uncertainty in radiative transfer models.
© 2008 Elsevier Ltd. All rights reserved.

1. INTRODUCTION

Sources and transport pathways of mineral dust play an important role in global climate, biogeochemical cycling and health. Globally, airborne particle mass mostly consists of minerals of terrestrial, marine, atmospheric and cosmic origin (Parkin et al., 1977; Keller et al., 1992; Andreae and Crutzen, 1997; Buseck et al., 2000; Arimoto, 2001). Dust from windblown soils (mainly great deserts) is an important component of the earth-atmosphere system (Simonson, 1995; Goudie and Middleton, 2001; Ramanathan et al., 2001). Many studies have evaluated such additions. Model estimates of the amount of desert dust generated by the Sahara range from 270 to 670 Tg year^{-1}, and Saharan dust transport to Europe ranges from 80 to 120 Tg year^{-1}, reaching distant regions, like South America (Swap et al., 1996), the North Atlantic-Caribbean area (Prospero, 1999), Northern Europe (Franzen et al., 1994) and perhaps as far as the Himalaya (Carrico et al., 2003).

---

* Corresponding author. Fax: +34 958 895 203.
 E-mail address: josel.diaz@juntadeandalucia.es (J.L. Díaz-Hernández).

0016-7037/$ - see front matter © 2008 Elsevier Ltd. All rights reserved.
doi:10.1016/j.gca.2008.05.037

Guerzoni and Chester (1996), Romero et al. (2003) and Jaenicke (2005) reported the presence of marine nanoplankton, pollen, diatoms and bacteria in aerosols from these areas. Great importance is attached to the role of mineral aerosols as a reactive surface in the global troposphere (Wurzler et al., 2000; Usher et al., 2003), where heterogeneous nucleation phenomena can occur with the creation of new phases (neoformations), mainly of sulfates and nitrates.

The Iberian peninsula is affected by the North Atlantic Oscillation (NAO)[1], and interannual variations in dust transport over the Atlantic Ocean and the Mediterranean Sea are well correlated with large-scale climatic variability of both atmospheric circulation and the hydrological cycle in the northern hemisphere (Moulin et al., 1997).

Dust contributes to marine sediments (Mahowald et al., 1999) or is incorporated into the pedogenic processes of soils (Rabenhorst et al., 1984; Simonson, 1995; Yaalon, 1997), affecting their biogeochemical cycles (Crutzen and Andreae, 1990; Stoorvogel et al., 1997). The soils of arid and semiarid climates typically show pedogenic features attributed to mechanical weathering and atmospheric deposition of Ca-bearing dust and clays (Ducloux et al., 1995). Several soil scientists have found that pedogenic carbonates and a portion of the clay contents of Aridisols originated in aeolian dust and precipitation-borne solutes. It is therefore important to monitor zones of direct Saharan influence in order to determine their effects on soils.

Wet or dry sediment traps (Rabenhorst et al., 1984; Goossens and Offer, 1994) are routine sampling methods that provide information on actual quantities deposited on the earth's surface or on relevant qualitative aspects. Using dry passive collectors for short periods (weekly) is an efficient method for such purposes, although handling small amounts of samples may be difficult.

The aim of this study is to characterize a group of atmospheric microspherulites, first detected in August 1999 in the airborne dust of the Southern Iberian Peninsula (Granada, Western Mediterranean), which we have dubbed iberulites, and to interpret their evolution. This may contribute to the understanding of the behavior in natural systems (Berstch and Seaman, 1999), particularly the atmosphere, of complex mineral assemblages that are hard to detect due to their fragility. To date, no information has been available regarding these particles, since standard techniques are not sensitive enough to avoid destroying such labile components, and in addition, they can only be obtained by sampling under special climatic conditions conducive to their atmospheric formation. To this end, we monitored atmospheric dust deposition for the period 1999–2005 near the city of Granada (Spain).

2. SAMPLING AND METHODOLOGY

2.1. Geographic background

The sampling site is located in the Granada Depression (37°10′N–3°31′W, 640 m ASL), surrounded by dolomitic limestone and siliceous relief. The soils in the depression are Calcareous Fluvisols (IARA-CSIC, 1989), with irrigated crops within a radius of a few tens of kilometers around the monitoring station and olive groves and forestry further away. The area is not heavily industrialized.

The mean annual temperature is 15.1 °C, ranging from 6.7 to 24.8 °C (January and July, respectively), and mean precipitation is 357 mm over the last 30 years, which corresponds to a semi-arid Mediterranean climate (data from Granada airport, Spanish Meteorological Institute, INM). From 1980 to 2005, annual precipitation for S and SE Spain has been below the century average and the mean temperature has undergone a significant rise of 0.7 °C (Staudt, 2004).

Conventional aerodynamic data show a high annual percentage (approximately 63%) of calm, with predominantly gusty winds under 5 km/h up to 10 AM, followed by an increase up to 20 km/h around midday, dropping around 4 PM to approximately 0 km/h. These values in themselves minimize the incidence of local supplies to our samplers, but they were reduced still further by placing the traps on top of a building surrounded by irrigated land.

2.2. Sample collection

Weekly samples of atmospheric dust and iberulites were taken from 1999 to 2005, mainly in the summer months, using the method described by Díaz-Hernández and Miranda Hernández (1997). This is a very flexible technique that uses passive collectors; either dry or wet collectors present similar efficiency (Goossens and Offer, 1994). We used dry dust collectors, consisting of 5 cm deep, circular porcelain trays 14.3 cm in radius. Because material only rises into the atmosphere by suspension (Tsoar and Pye, 1987; Mainguet, 1992), it was important to prevent particles from the surrounding soil from entering the samplers by roll or creep. The collectors were therefore placed on top of a building (about 10 m above the ground) surrounded by a 1-m-high perimeter wall and open so as not to restrict wind movement (Frank and Kocurek, 1994; Offer and Goossens, 1994). This rooftop is covered with coarse gravel (20–35 mm diameter), which prevents incorporation of dust particles deposited on it (Goossens, 1994). In addition,

---

[1] *Abbreviations used:* α, particle radius; ACE, aerosol characterization experiment; ASL, above sea level; BSE, back scattered electrons; CCN, cloud condensation nuclei; DMS, dimethyl sulphide; Dp, diameter equivalent; EDX, electron diffraction X-ray; EMEP, European monitoring evaluation program; FESEM, field-emission scanning electron microscopy; HIRLAM, high resolution local area model; HRTEM, high-resolution transmission electron microscopy; INM, Instituto Nacional de Meteorología; MBL, marine boundary layer; MODIS, moderate-resolution imaging spectroradiometer; NAO, North Atlantic oscillation; N_{Re}, Reynolds number; NSS, non sea salt sulfates; SAED, secondary areas electron diffraction; SAL, Saharan air layer; SE, secondary electrons; SEM, scanning electron microscopy; TEM, transmission electron microscopy; TOMS, total ozone mapping spectrometer; TSP, total suspended particles; XRD, X-ray diffraction; LITE, lidar in-space technology experiment; MINOS, main injector neutrino oscillation search; MINATROC, mineral dust and tropospheric chemistry; SAMUM, Saharan mineral dust experiment; SHADE, special handheld based applications in difficult environment; STEM, scanning transmission electron microscopy.

the plates were placed on a mast 2 m above the rooftop. The trays, washed with distilled water and dried, were checked daily mainly during the summer, obtaining varying rates of iberulite deposition. A record was kept of collection times.

The deposited dust was carefully collected using a brush, stored in glass vials and weighed to a precision of 0.1 mg. Since the porcelain surface is very smooth, the dust was not embedded and breakage of the iberulites was avoided by carefully brushing them down the deposition trays. In summer months, the atmospheric conditions of the area prevent formation of dew, so dust and iberulite adherence to the tray and brush was minimal.

Authors including Buat-Ménard et al. (1989), Pye (1992) and Drees et al. (1993) often used long and irregular sampling periods. In these conditions, rates are normally expressed on the basis of a sample weight over a certain time for a sampling surface. In this study, sampling was scheduled on a weekly basis from 2000 to 2005, and rates of dust input were converted to an equivalent $g\,m^{-2}\,day^{-1}$ basis for comparison, although the amount of sample collected was very small and could be a limiting factor for later analysis.

2.3. Sample selection criteria during the study period

Samples of events with iberulites were selected in order to better characterize the phenomenon and obtain a general overview. The selection criteria were having a sufficient amount of sample, and collection during dryfall, thus avoiding red rain to prevent dissolution and neoformation. Table 1 shows the selected events and their main weather features. Although iberulite events were recorded in 2003, the quantity of samples collected was insufficient for correct analysis, so they were not included.

In the same years that these events were recorded, TSP levels (Total Suspended Particles) were also obtained from the ambient air quality monitoring network of the European Monitoring Evaluation Program (EMEP network). These data offer a general framework for our dust collections. The monitoring station used was ES07 (Víznar), located 10 km from our sampling station and supervised by the Spanish Environment Ministry. TSP levels were obtained by weighing the aerosols collected using a high-volume sampler (MCV, Model CAV-A/HF).

2.4. Sample analysis procedures

A quarter of each sample was taken and the dust separated from the iberulites. Each fraction was weighed using a microbalance (Mettler Toledo, AX26). Amounts of mineral dust and iberulites were significantly higher than the weighing error ($d = 0.002$ mg/0.01 mg).

2.4.1. Optical observations and image analysis

Sample trays were screened using a stereo-microscope with oblique illumination at different magnifications. This routine procedure enabled us to establish the sampling periods containing iberulites and to separate the iberulites from the surrounding material (dust) by carefully hand-picking with a very thin pin, avoiding sample contamination and breakage. Color was determined by Munsell charts (1995) and natural light using an iberulite concentrate.

Morphometric features of our iberulites were determined by digital image analysis. Color photographs of iberulite concentrate were taken using a stereo-microscope, opposing mixed light and a black background to remove shadows and assist in particle selection. These images were analyzed to determine particle length, surface area, perimeter and circularity. The largest and smallest lengths of each particle were measured, representing the primary and secondary axes of the best fit ellipse; the area of each iberulite was obtained in square pixels; perimeter was measured as the length of the outside boundary of each selection; finally, circularity was defined as $4\pi \times (area/perimeter^2)$, where a value of 1.0 indicates a perfect circle.

2.4.2. Particle size distribution

The grain-size distribution of iberulite constituents and dust was obtained with a CIS-1 Galai® Laser Sizer, because they are easily dispersible. Distribution was determined three times, at 15-min intervals, in an ethanol suspension to prevent dissolution of soluble salts (mainly chlorides). Acquisition times varied depending on the suspension

Table 1
Event chosen for this study, together with weather observations and summary of main depositional and physical features

Event (date)	Sampling period	General climatological observations	Red rain	Rates ($g\,m^{-2}\,day^{-1}$)	% Iber.	Major axis (μm)	Minor axis (μm)	Roundness index
010808	5th (6:00 PM)–11th (6:00 PM)	Last day very hot, haze, threat thunderstorm	No	0.050	34	80	70	0.95
020618	13th (4:20 PM)–24th (8:15 AM)	Haze, cumulo-nimbus, threat thunderstorm	No	0.082	23	80	80	0.95
040720	16th (8:00 PM)–23th (8:00AM)	Period intensely hot and hazy	No	0.020	23	80	80	0.95
040822	20th (3:15 PM)–24th (2:15AM)	Heat, haze and threat of thunderstorms	Later	0.001	16	70	60	0.95
050401	1st (6:00 PM)–2nd (6:30AM)	Abnormal rise in temperature, cloudy	Later	0.113	47	70	60	0.95

Event code: 01-08-08 indicates year, month and central day of sampling period. Sampling period means beginning and end of said period in terms of clock time.

concentration. The suspension was previously exposed to ultrasonic dispersion in a water bath for 3 min. The size range of the instrument was 0.2–150 μm (0.3% resolution of full scale). The data were expressed in 0.5 μm ranges once the measurement limit was determined.

2.4.3. Electron microscopy techniques

Scanning Electron Microscopy (SEM) was used with selected iberulite samples to obtain morphological and chemical information. The samples and equipment were set up according to the specific aim of analysis.

A high-resolution Field-Emission Scanning Electron Microscope (FESEM, Leo 1530) equipped with a LinK INCA 200 (Oxford Instruments) microanalysis system was used for the morphological study and to identify mineral phases. For SEM/EDX mapping (Zeiss DSM950), the samples were soaked in Epon resin and cut with a diamond knife ultramicrotome (Reichter Ultracut S) to expose their interior. The same samples were used to obtain SE (Secondary Electrons) and BSE (Back Scattered Electrons) in a LEO 1430VP microscope.

Iberulites were dehydrated in pure ethanol for 15 min and then placed in an ethanol/Epon resin mixture and shaken for an hour. They were then polymerized and cut into thin sections (70–90 nm) with an ultramicrotome. This process frequently detached some large-size grains; these samples were examined using a high-resolution Phillips CM-20. Point-to-point resolution was 0.27 nm and beam sizes were 200 nm (TEM, Transmission Electron Microscopy) and 10 nm (STEM, Scanning Transmission Electron Microscopy).

Quantitative microanalyses were carried out in an EDAX system equipped with a Si (Li) detector, using a 5-nm beam diameter and a 10×20 nm scanning area. Electron diffraction patterns were obtained from selected areas (SAED) and High-Resolution Transmission Electron Microscopy (HRTEM) lattice-fringe images were obtained as suggested by Buseck et al. (1988).

2.4.4. X-ray diffraction (XRD)

The mineralogy of dust and iberulites was determined with an Enraf-Nonius Powder Diffraction System 120 (Natural History Museum, London) and a Brucker AXS D8 Advance (University of Granada), in both cases using diffracted-beam Cu-Kα. The measurement conditions were $3°–70°2\theta$, range step scan 0.02° and 8 seg/step as very little sample was available. Analysis time was about 8 h for both systems. The diagram, phase identification and profile analyses were carried out using DIFRAC^{Plus} SEARCH, Bruker® and XPowder software (Martin, 2004).

2.4.5. Electrophoretic mobility (Ue) measurements

These measurements were made using an automated electrophoresis instrument (Malvern Zetasizer, 2000, Malvern, England) at 25 ± 0.5 °C. The ζ-potential was calculated using the Smoluchowski formula (Arroyo and Delgado, 2002).

Electrophoretic mobility was carried out on dust and iberulites (from each event) and pure selected mineral patterns (albite, calcite, dolomite, gypsum, hematite, kaolinite,

muscovite, orthose, quartz, and smectite as major components of the iberulites and dust). Determinations were made in triplicate using suspensions in bidistilled water containing 0.1–0.2 g/L solids, previously exposed to ultrasonic dispersion in a water bath for 1 min. This concentration was necessarily lower for iberulites and dust.

3. RESULTS

3.1. Deposition levels and periods of appearance of iberulites

We first detected iberulites while investigating the contribution to the soils of a medium-sized forest fire on 16–18 August 1999 (Sierra de la Almijara, Granada, Spain), located some 50 km from the sampling station (Díaz-Hernández, 2000). Monitoring was carried out regularly during the months following the fire (including winter) until iberulites were again collected on 26 June 2000, with no forest-fires intervening. Dust samples were collected over the period 2000–2005 in order to exactly define the appearance patterns of iberulites, centering only on studying and monitoring iberulite events. Table 1 summarizes the dust rates and iberulite percentages in the selected event samples, although these amounts were probably somewhat higher due to the difficulty of carrying out complete separation. The amounts of iberulites obtained on 17 and 19 August (1999) was around 0.038 g m^{-2} (i.e., 0.019 g m^{-2} day^{-1}). The deposition of iberulites on these two days (iberulites were not observed on successive days) was equivalent to 10–12% of the total dust obtained on these dates. These deposition rates (including rates for 1999) suggest a close relation ($R^2 = 0.66$) between the amounts of dust and the iberulites collected on these days (higher dust rates imply higher iberulite rates).

Fig. 1 shows the distribution of dustfall rates during 1992, with maxima occurring with winds from the south (38%), contributing 50% of the total for that year. The dustfall rate for this region was thus calculated as 23.06 g m^{-2} year^{-1} (Díaz-Hernández and Miranda Hernández, 1997), with no iberulites screened in any of the samples. This annual distribution pattern shows a repetitive tendency (summer and spring maxima coincide) and is similar to that obtained in the TSP collected between 1999 and 2005 at the nearby ES07 monitoring station (Fig. 2). The value obtained falls within the range of rates described by Simonson (1995) in a global context and by Loÿe-Pilot et al. (1986), Pye (1992) and Bücher (1994) in the Mediterranean area, none of whom mentioned the presence of iberulites.

Given the difficulty of separating iberulites from dust, we evaluated the importance of the phenomenon by taking the number of days they were detected in one month as an estimate: frequency is high if detected on 15 or more days (***), medium between 5 and 15 days (**) and less than 5 days (*) the phenomenon is considered occasional (low). Fig. 2 shows that iberulites are mainly found during the summer (driest months); outside the summer months (November–February) iberulites were only rarely collected (sporadically in February or March, around springtime), probably because of the low TSP contents in the atmosphere (lower supply together with scavenging by rainfall)
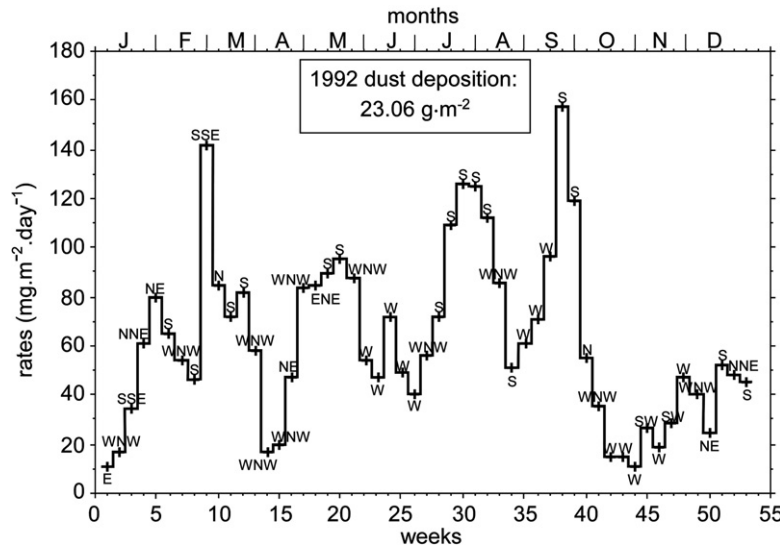
Fig. 1. Temporal distribution of dust additions to the southern Iberian Peninsula in 1992. Lines indicate atmospheric dust deposition rates and letters indicate wind direction regime. Figure data compiled weekly (dust rates and wind directions). No iberulites were collected this year. Source wind data: Granada airport, INM.
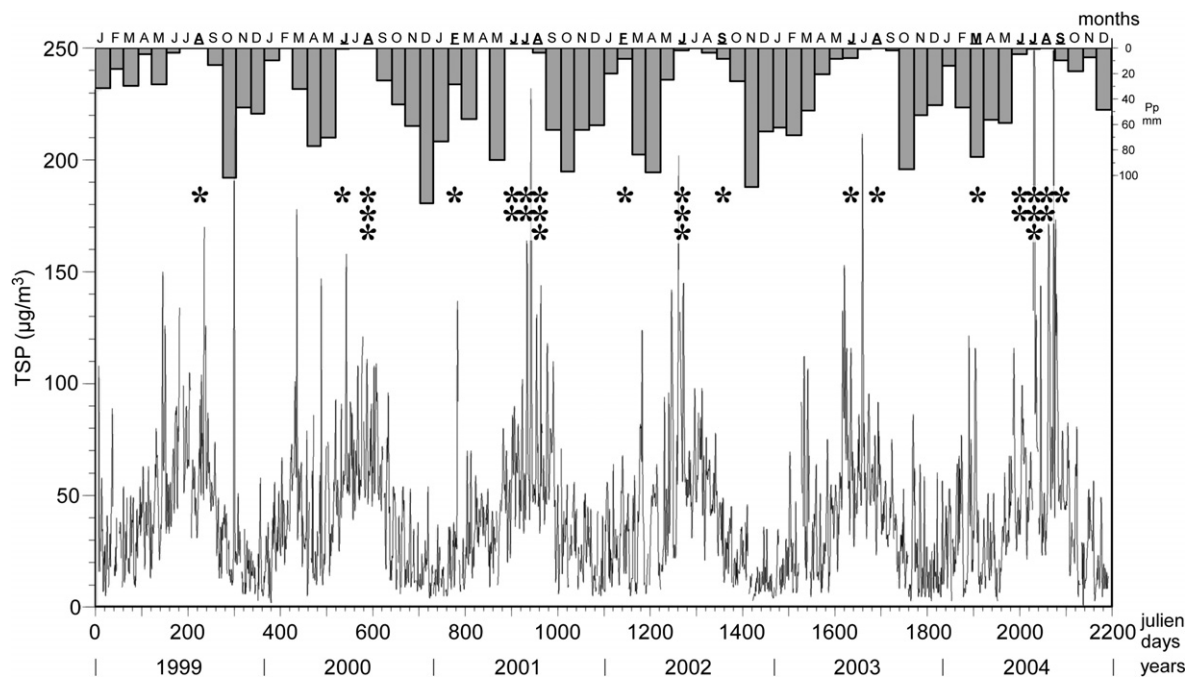
Fig. 2. Interannual iberulite additions recorded in 1999–2004, indicating low (∗), medium (∗∗) or high (∗∗∗) roughly estimated frequencies. This monitoring is accompanied by records of monthly precipitation (bars) and TSP levels (lines) obtained at station ES07 of the EMEP network (Spanish Ministry of the Environment).

and also due to disintegration caused by dew and frost. This general framework indicates that the appearance of iberulites is a discontinuous phenomenon, occurring mainly in a dryfall context corresponding to the highest levels of solid additions (Fig. 2).

In addition, iberulites sometimes coincide with red dust rains (muddy rains) in the summer period, as long as rainfall is not heavy, since this would tend to disintegrate them and only isolated mineral particles would be collected.

Some iberulites were preserved in these circumstances (Fig. 3A), but their possible chemical and physical alteration prevented their use in later analyses. Saharan red rains are related to specific synoptic situations of atmospheric circulation during periods of intense insolation. These weather patterns can be observed on the synoptic charts at 850–700 hPa during the monitoring period (synoptic surface charts and High-Resolution Local Area Model (HIRLAM) (*Source:* INM, data not shown).
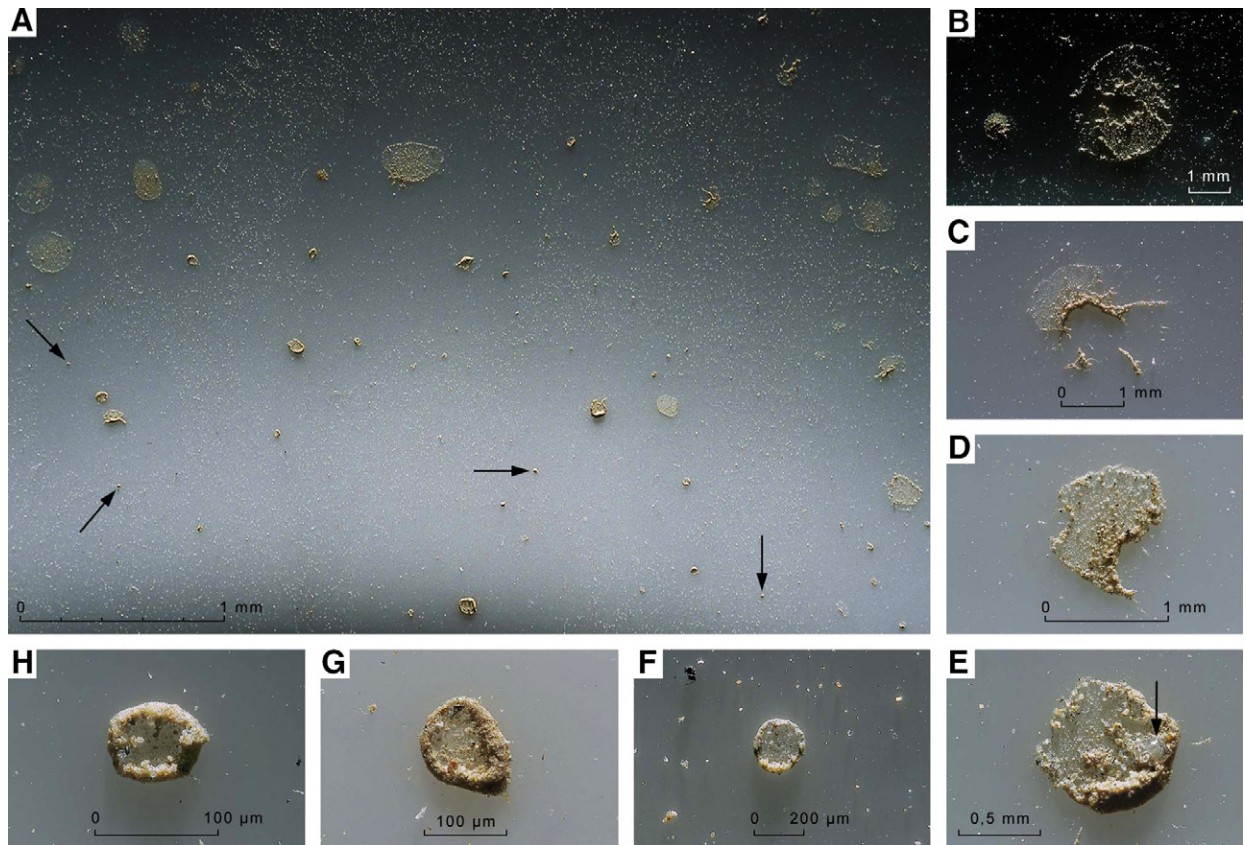
Fig. 3. Appearance of red rain episode (20 August 2005). (A) Panoramic view of raindrop impacts on part of a sampling tray; a variety of shapes and sizes is observed with variable dust content. Arrows correspond to some iberulites associated with this episode whose diameters ranged approximately from 18 to 32 μm. (B–H) Sequence of raindrop impacts ordered by decreasing size. (B) Aureole of a raindrop whose dust is concentrated in the annular ring (toroid), leaving a dustless hollow in the center (raindrop impact radius = 1.336 mm). (C and D) Irregular impacts. (E–H) Muddy raindrop impacts with radii less than 500 μm. Some blackish soot remains are visible (micrographs D–H).

As a demonstration, Fig. 3 shows the images of a typical warm red rain episode taken between 3 PM on 16 August and 7 PM on 17 August 2005. The larger micrograph represents the general appearance of the sampler, where the impacts of relatively large muddy raindrops can be seen. Some iberulites deposited in this event are also indicated. The adjoining details (micrographs B–H) show a sequence ordered according to the water content of the raindrop. The higher the water content, the larger the impact trace becomes, as well as flatter and more irregular, with higher dilution of the solid charge. On the other hand, if the water content is low, impact size is smaller, with more cohesion between its constituent particles, producing globular forms with jagged edges and hollow interiors.

3.2. Morphology

In order to avoid repetition, all the compositional patterns mentioned in this section were obtained by EDX.

3.2.1. Global morphology and image analysis

The iberulites are mostly spherical in shape and vary in size when observed with a binocular microscope (Fig. 4).

Micrograph 5 gives a panoramic view of the iberulites from the event of 1 April 2005. Details of the iberulites from the five events analyzed here can be seen in micrographs 1, 2, 3, 4 and 5-2. They are often associated with filaments of plant matter (3A, 5.1A, 5.2A and 5-2B), in which case their shape is adapted to the axis of the filament, and are sometimes associated with crystals (5-1A and 5-2A). They are basically pink (10YR6/4 color), with frequent reddish and blackish speckles. Gray and red colors (4A) have occasionally been observed. The surfaces of most of the iberulites show a typical conical depression, which we call the vortex (1A, 1B and 2A), and which can at times be so deep as to be translucent (1B and 2A). The vortex is roughly conical with the base at the surface and the vertex inside the micros45pherulite.

Morphological patterns of iberulites (Fig. 5) were obtained by image analysis of the iberulite concentrate from each event. The global sample determined from the event data obtained ($n = 5121$ iberulites) shows sphericity: roundness index = 0.95, major axis = 75 μm, minor axis = 65 μm. Ninety-six percent presented a roundness index $\geqslant 0.85$, 54% of the population had a 60- to 90-μm major axis and 61% a 60- to 90-μm minor axis (Table 1). These distribution patterns are similar across the events, although events 020618
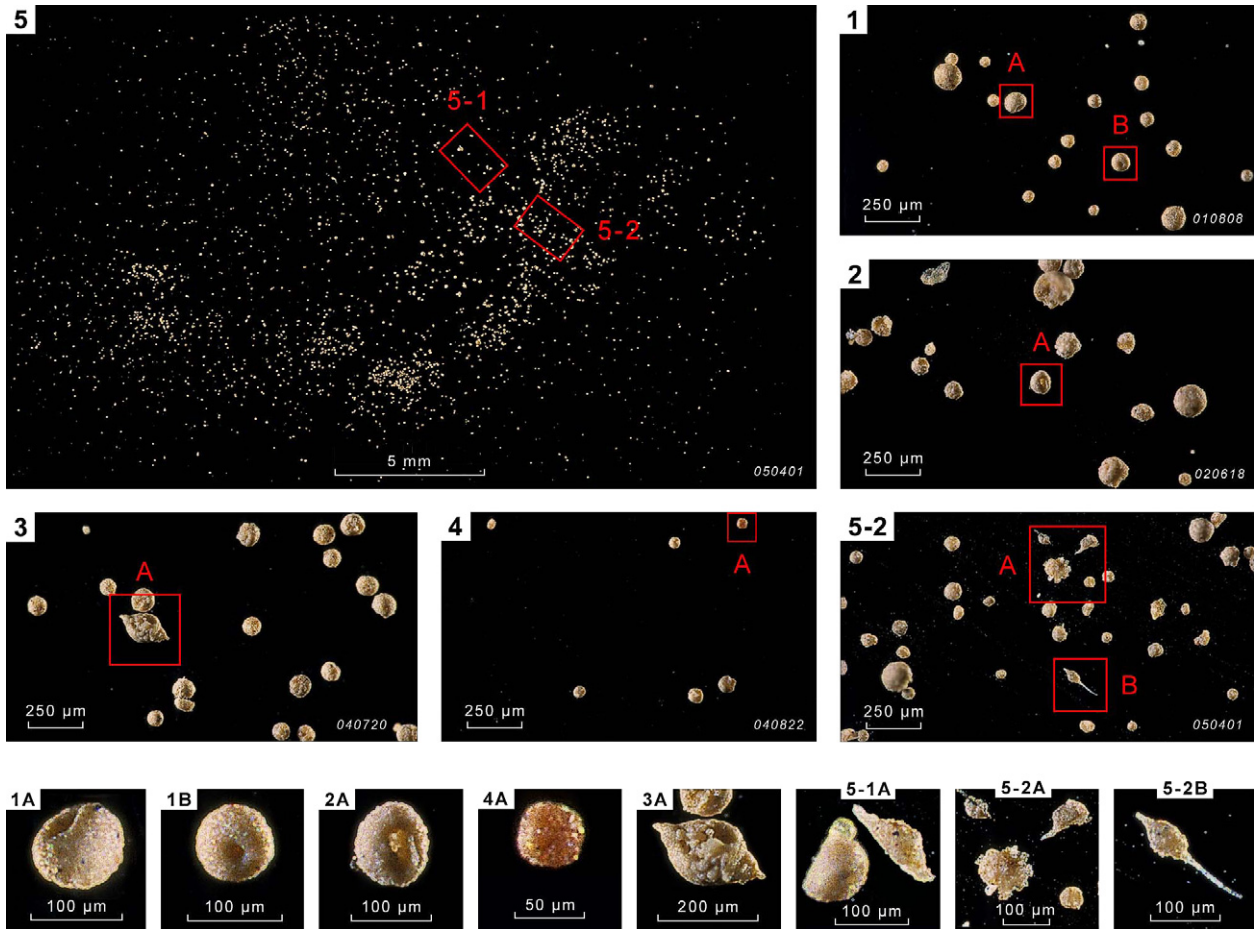
Fig. 4. Iberulite features observed by stereomicroscope at different magnifications. Micrographs 1–5 correspond (numerically also) to details of iberulite concentrate extracted from the global dust sample of each of the five events (Table 1). We have selected a general view from one of them (event 5); the other general views (not shown) are similar. The iberulites in this view resemble colored pinheads. Under greater magnification, typical features can be observed—rounded shape, vortex and color. Micrographs 1A–5.2B are enlargements of the red boxes in their respective micrographs: the first three give different details of the vortex and the others show variations in shape and color. Black spots (soot) are also seen here (micrographs 1A and 5-1A).

and 040720 showed more dispersion in their modes, although always around the same values. The values furthest from the modes were found in elongated iberulites, associated with plant filaments (4, 3A, 5-1A and 5-2B). The similarity between the radii of the two axes suggests that the iberulites are closer to spherical forms than oblate spheroids.

The equivalent volume was calculated by determining the projected area of each spherule, which allowed us to estimate a bulk density of $0.65 \, \text{g cm}^{-3}$ after determining the total weight of the iberulites in a high-precision balance. Mean porosity was estimated at around 50%, based on analysis of SEM images of nine sectioned iberulites from events in 2001, 2004 and 2005, soaked in Epon resin. We believe these values are consistent, considering the variety of constituents in iberulites and the influence of the vortex on volume calculations.

3.2.2. External and internal morphological features

The structural elements that characterize an iberulite are the vortex, the core and the rind.

SEM images (Fig. 6) of iberulites show only one vortex (micrograph A), which does not appear to be either an impact or "ejection" crater. The vortex is a typical morphological features that distinguishes them from other spheroids, especially from cosmic spherules (Fig. 7). The microspherulite surface can be relatively rough and porous, formed by assemblage linking of neighboring mineral particles, frequently with angular edges. Around the vortex, the surface is smoother, indicating a predominance of very small (<0.5 μm) laminar habit minerals. The spherical morphology of these iberulites may be distorted by adaptation to plant filaments, giving them an elliptical shape, with the axis corresponding to the filament, which can be of highly variable length (Fig. 6B).

Because iberulites are fragile, it is relatively easy to study their interiors. Fig. 6C and D shows a core formed by angular mineral particles of very variable sizes coexisting with other more rounded particles and apparently without a cementing matrix. The coarser components are concentrated in the core of the spherulite, finer particles occupy the intermediate zone and the thin, rind-like outer coating
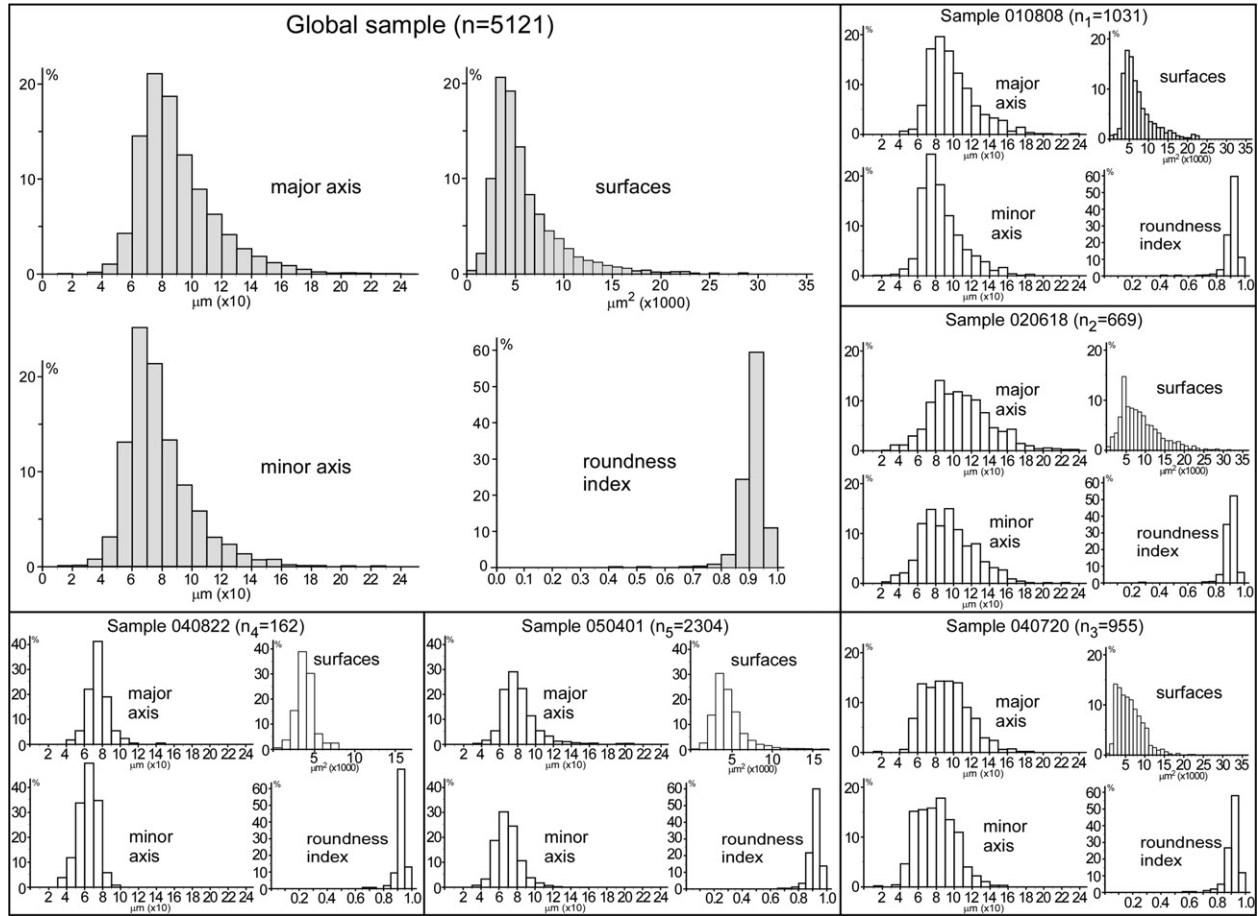
Fig. 5. Frequency distributions, expressed as percentages, of several morphological parameters obtained from image analysis of iberulites. Distributions were made for each event and for the global sample ($n = n_1 + n_2 + n_3 + n_4 + n_5 = 5121$). Distribution patterns are similar. The high roundness index is noteworthy for all events.

consists of laminar habit minerals (clays and to a lesser extent gypsum).

3.2.3. Biological constituents

Apart from plant filaments, iberulites are frequently associated with remains of skeletal structures typically made of silica (diatoms). The diatoms are distributed anywhere inside the iberulites, but are often found near the surface (Fig. 8A), beneath the rind. We also observed broken frustules with rounded edges in sectioned iberulites (Fig. 8B), apparently indicating prior erosion.

Although knowledge about fragmented biological particles in the atmosphere is very limited (Jaenicke, 2005), we have frequently found biological remains, generally linked to the outer parts of iberulites, that are probably marine planktonic forms like coccolithophores (Fig. 8C). These are biogenic skeletons, formed by calcite in this case, that present a characteristic pedunculate morphology in a very good state of conservation (Fig. 8C2). In one case (Fig. 8C1), rounded calcite forms of dubious definition were observed, in whose folds we found a specimen that could either be an unusual icosahedral capsid from a virus or an early growth stage of *Emiliana Huxleyi*.

3.2.4. Crystal growth phenomena

We detected numerous crystals with a well-defined habit with a formation related to the processes affecting the iberulites (Fig. 9), indicating that recrystallization and mineral neoformation phenomena occurred.

The halite produced well-developed crystals, probably due to its availability and facility to participate in processes of dissolution and precipitation. Micrographs A and A1 show a prismatic halite crystal on a calcium sulfate-covered filament. Micrograph B shows a halite cube attached to an iberulite; the halite cube has abundant granular deposits on three adjoining faces and no dissolution figures can be seen. The cube is anchored to the iberulite by a thin external rind, which, in this case, presents a delicate equilibrium. Micrographs C and C1 show accumulations of calcium sulfate as "toothlike" gypsum crystal growths produced from inside the vortex.

3.3. Constituent particle size

The size distribution of constituent particles of the dust and iberulites are shown in Fig. 10, in which we consider each event separately, as well as the average event. All dis-
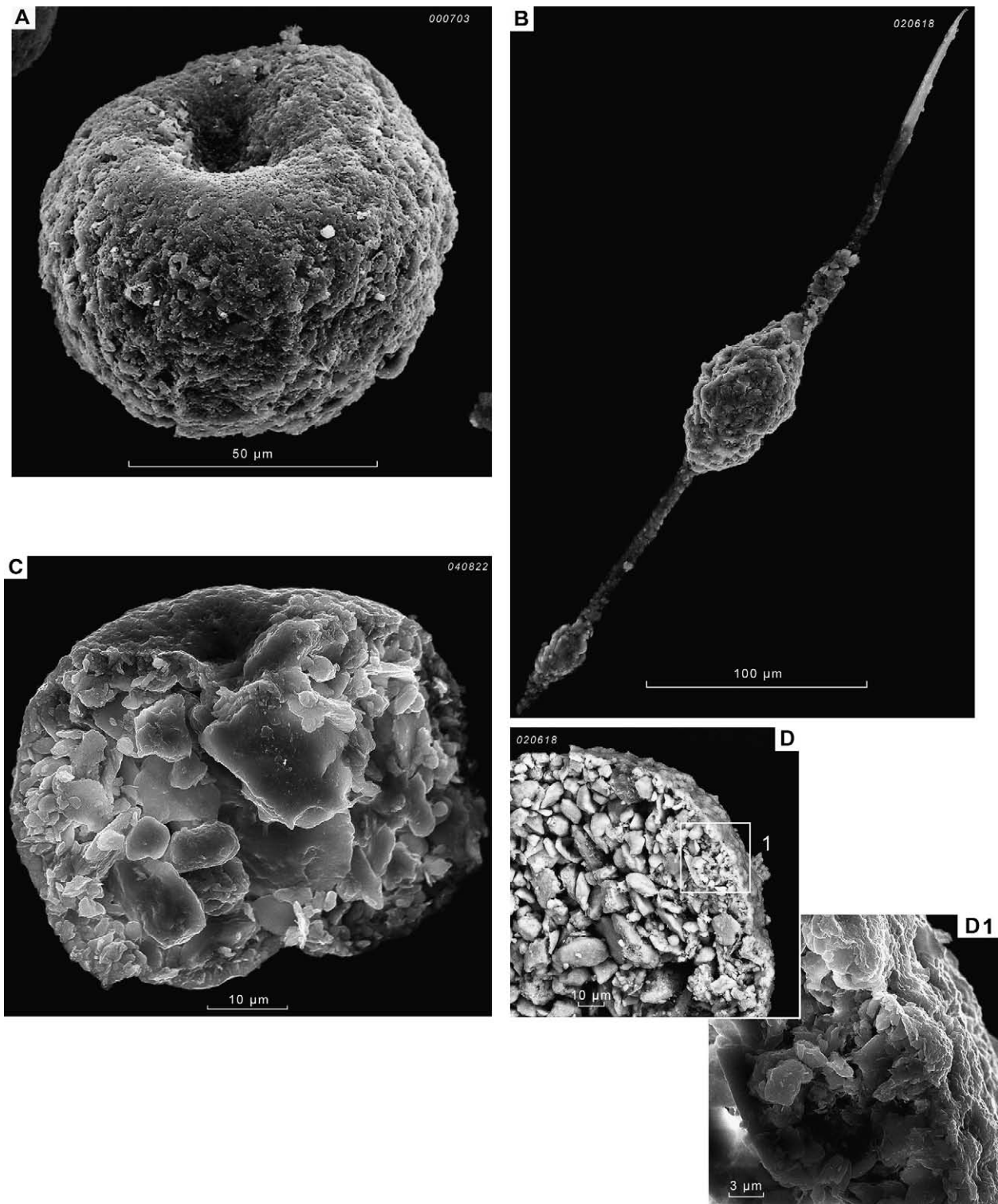
Fig. 6. SEM images showing morphological aspects of iberulites. (A) External textural differences in a single iberulite; smoothest textures are around the vortex and the rest of the surface shows adhering mineral grains. (B) Iberulite pierced by long plant filament; in this case the iberulite is ellipsoidal in shape and its body can be found either at the center or at the ends of the filament. These filaments are of plant nature and highly variable length and can deform the spherical shape. In this case, the peduncle of the iberulite presents high gypsum content. (C and D) Internal views of two iberulite halves, formed by mineral particles with angular edges, showing small spaces between them. The external surface is covered by a thin rind of laminar habit minerals. These mineral particles range gradually from large (core) to small (rind).
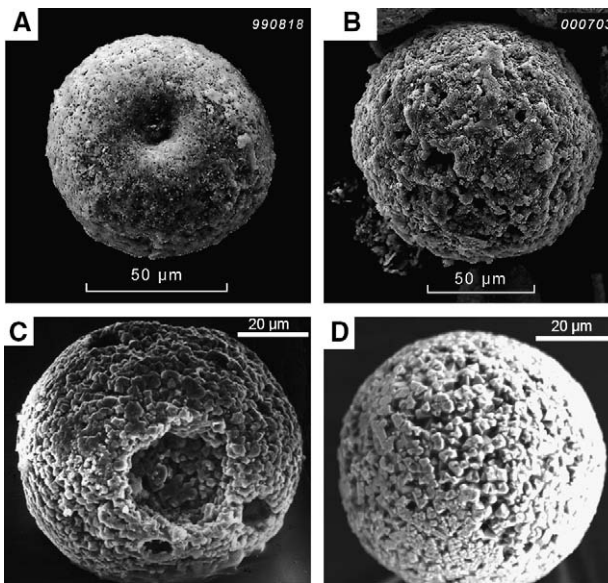
Fig. 7. Comparative SEM images of two iberulites (A and B) and two similar cosmic spherules (C and D). We have selected two cases of cosmic spherules that present the most similar appearance to iberulites. We underline that the iberulite vortex has a different shape, number and texture than the pit(s) on the cosmic spherules, and the shallow features in each micrometeorite are identical, while in each iberulite they vary. Finally the composition of iberulites and cosmic spherules are quite different. Cosmic spherules micrographs courtesy of Dr. D. W. Parkin (www.bath.ac.uk/ceos/index.html).

tributions are roughly similar for all events: events 010808 and 050401 were bimodal (for dust and iberulites), with modal radii at 1 and 3.5 μm; event 020618 was unimodal for dust (mode 3.5 μm) and bimodal for the iberulites (modes at 3 and 5 μm). Due to the lack of a dust sample, there is only a histogram for the iberulites from event 040720, but it could be considered bimodal (modal radii at 3.5 and 5 μm). Event 040822 presents roughly unimodal distributions in both cases, with modes around 3.5 μm. The average event obtained from the preceding data has very similar, slightly bimodal patterns for dust and iberulites, with modes at 1 and 3.5 μm in both cases. Generally speaking, the maximum value for all the modes of constituent particles is around 3.5 μm for both dust and iberulites, corresponding to a 12–14% range. Analysis of the results obtained with the particle analyzer found very few particles over 10 μm for any of the events, with the exception of 040720, where 2.5% of particles were this size.

The amount of fine particles found for the dust events (2002, 2004 and 2005) was practically identical at 30% (Fig. 10). In the 2001 event, the amounts were 45% fine and 55% coarse. All the iberulite events had higher range variations for fine particles (24–42%). Since the measurement technique is probably biased, we compared the measured sizes of constituent particles with SEM and TEM images (Fig. 6C, D and D1), obtaining an acceptable fit between both techniques, because the fine particles are mainly concentrated on the thin rind, whereas the coarser are in the core: their relative volume abundances are different.

The average dust and iberulite events had similar compositions of fine particles (32% and 30%, respectively) and coarse particles (68% and 70%, respectively) with a very similar distribution pattern (Fig. 10). The particles making up the iberulites and dust would thus be included in the clay (<2 μm) and fine silt (2–20 μm) fractions.

The abundance of coarse particles (close to the fine size limit) indicates that these particles are mainly generated by mechanical processes from soils in and around the Sahara, whereas the fine particles have different sources (Seinfeld and Pandis, 2006), and could originate in part from friction and collision of coarse particles both on the ground and in the atmosphere. The fine fraction (mainly < 100 nm, Pruppacher and Klett, 1997) would assist the formation of cloud droplets as cloud condensation nuclei (CCN).

3.4. Electrophoretic mobility

Electrophoretic mobility was measured to estimate the degree of aggregation of iberulites. The ζ-potential measured for iberulite particles and dust was similar for each event and approximately similar taken together. The extreme values for these potentials corresponded to the iberulites of the 2004 (−39 mV) and 2005 (−24 mV) events, possibly due to mineralogical differences. The ζ-potential measured for iberulite particles and dust is the average of those of their main constituent minerals, which were all negative, ranging from −43 mV (muscovite) to −23 mV (kaolinite).

3.5. Mineralogical composition

3.5.1. Iberulite bulk mineralogy (XRD)
The bulk mineralogical composition of the dust in all events (Fig. 11) consists largely of dolomite and quartz (>30%), accompanied by calcite, gypsum, halite and illite in lower proportions (12–2%); minor phases included beidellite, hematite, kaolinite, montmorillonite and albite (<2%). The bulk mineralogical composition of iberulites in all events consists largely of quartz (>30%), accompanied by calcite (7–38%); gypsum, dolomite and halite (3–10%); and illite, beidellite and hematite (2–4%); in lower proportions, minor phases included kaolinite, montmorillonite and feldspars. The extremely small amount of iberulite samples prevented the identification of other phases, especially in iberulite sample 040822.

All the events had a rather similar mineralogical composition in both dust and iberulites. However, the iberulites contained higher amounts of phyllosilicates than the dust: the iberulites in any event contained between two and four times as much beidellite (and hematites) as the dust, and the kaolinite contents of the iberulites are consistently twice those of the dust.

The high proportion of dolomite in the dust of all events is noteworthy (over 36%), whereas the most found in iberulites was 7%, probably due to local Iberian inputs. This dolomite contribution to the dust would explain the relative decrease of the other minerals, in which case they would present very similar quantitative compositions. Moreover, the iberulites collected in the 2002 event showed a high
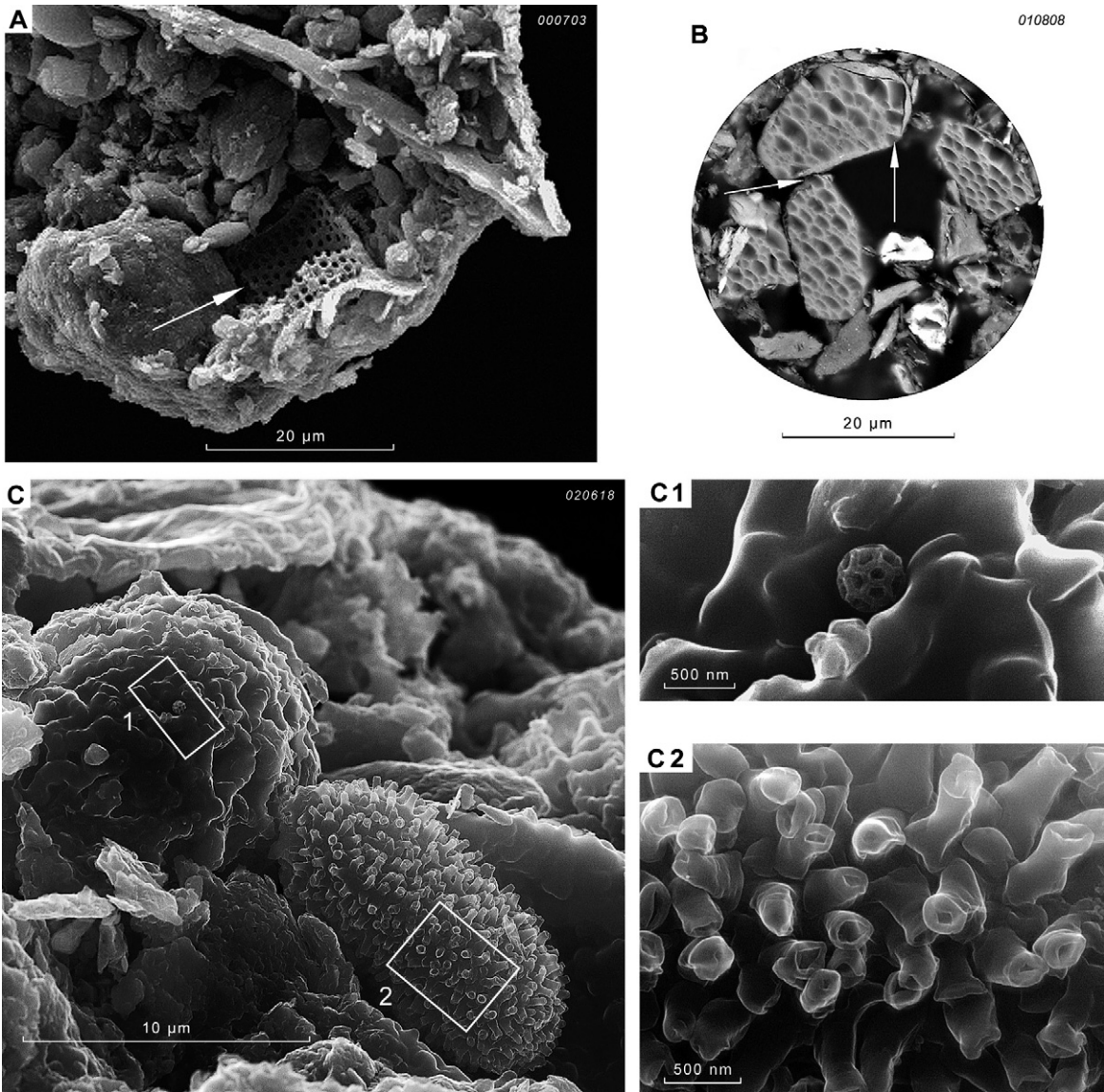
Fig. 8. SEM images of biological components of iberulites. (A and B) SEM images of diatoms included in the bodies of two iberulites collected during different events. (B) Iberulite sections, after soaking spherule in Epon resin. We observe a number of eroded diatoms, with the chambers frequently broken. (C) Remains of carbonate skeletons, possibly belonging to marine plankton. The skeletons are all found on the outer surface of the iberulite and belong to the same event. The excellent conservation of these extremely labile forms and the similarity between them is noteworthy. (C1) Biological specimen (virus or planktonic form) and (C2) detail of peduncular morphology of a biogenic skeleton.

(38%) calcite content, probably from the source area. It should be noted that the percentages of beidellite (and hematites) could be slightly higher through loss of crystallinity (amorphization detected by TEM).

3.5.2. Iberulite electron microscopy analysis

EDX analysis of the surface (rind) indicates that the major constituents are O, Si, and Al; Ca, Mg and S contents are also noteworthy. The minor constituents are Fe, K, Cl, Na, Ti and Sr in decreasing order of abundance, and more rarely V and Ba. The spectra suggest a great abundance of clay minerals (phyllosilicates), accompanied by sulfates (Ca, Na, K, Mg and Al) and halides (Na, Ca, K and Mg) (Fig. 9). In some cases, phosphate-vanadate, baritine and celestine were detected as well.

EDX analysis of the core (Fig. 6) showed the major constituents to be O, Si, Ca and Al (in decreasing order of abundance); Mg, Na, K and Fe were present in intermediate amounts, and S, Cl, and P in very minor amounts, but not in all the iberulites. On the basis of the clear morphological features of many mineral grains, we identified the larger ones as calcite, dolomite, quartz, feldspars, micas, and iron oxides, and occasionally clay minerals, rutile, ilmenite and apatite, among others.

In order to gain a more comprehensive view of the element distribution, we performed EDX mapping (Al, Ca,
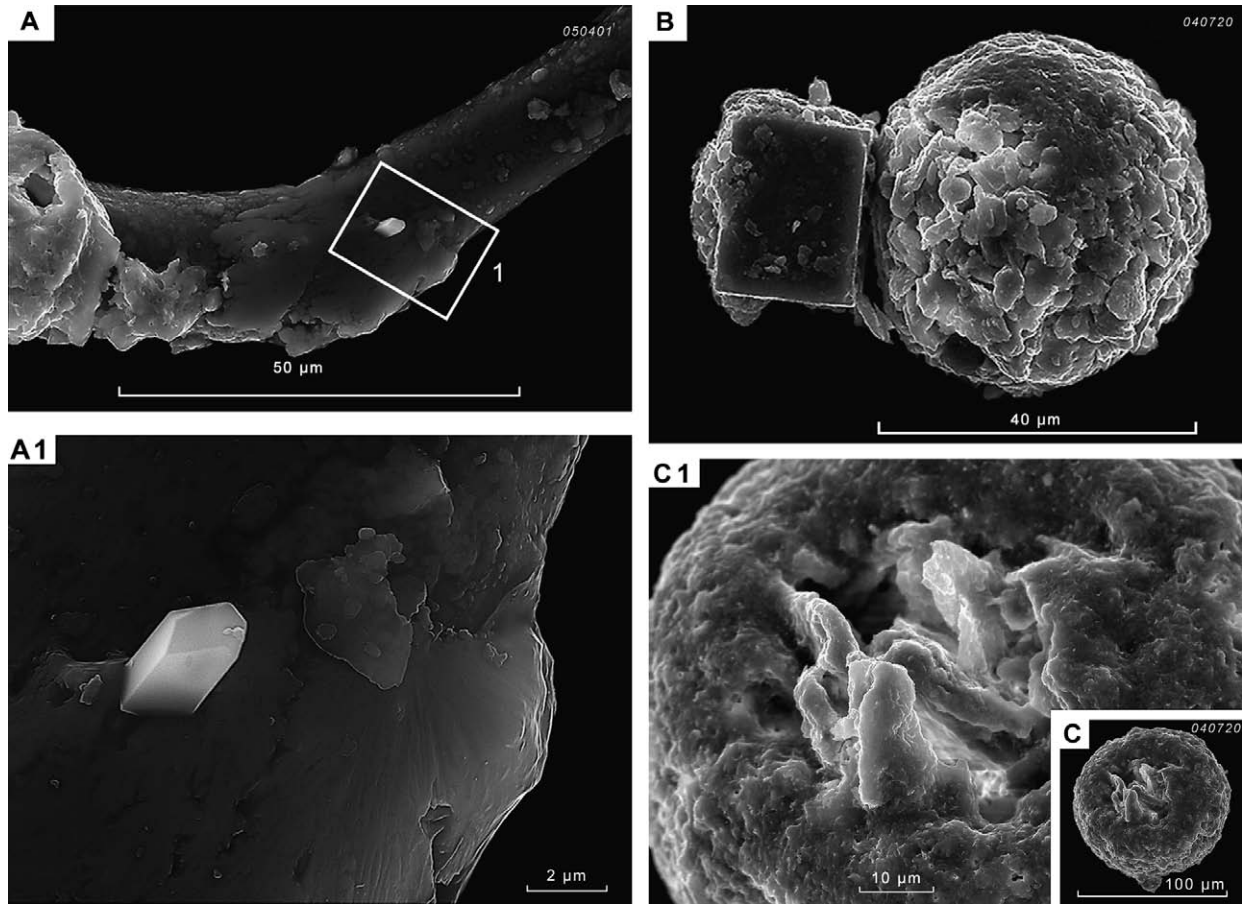
Fig. 9. SEM images of halite and gypsum crystalline growths on microspherulite surface. (A and B) Different sodium chloride crystal habits. (A and A1) Part of a plant filament of an iberulite covered in gypsum flakes, on which an idiomorphous sodium chloride crystal has developed. (B) One face of a well-developed cube adhered to an iberulite. (C) "Toothlike" gypsum crystals inside a vortex.

Cl, Fe, K, Mg, N, Na, S and Si). Fig. 12 shows that gypsum mainly occurs in the rind of the iberulites in all the events examined, generally associated with phyllosilicates and occasionally with carbonates. This is corroborated by the halo shown in S mapping and by the yellow halo resulting from the superposition of the S (green) and Ca (red) spectra. The maps of N, Cl and Na gave poor resolution images. The maps of Si, Fe, Mg and K do not show preferential distribution in the body of the iberulite.

TEM-EDX analyses were carried out on all events. The individual minerals indicated that major constituents were O, Si, and Al, followed by Ca, Mg, Na, K, Fe, Ti, Cl and S; minor constituents were P, Sr, Ba, Ce, La, Y, V, Ni, Mn, Br, Pb, Mo, and Cr, with the first three (P, Sr and Ba) being detected on more than one occasion.

This analysis gave similar mineralogical characteristics to those found by SEM, which agrees with the zonation observed in the sections of iberulites (core, intermediate zone and rind). However, based on the results of TEM-EDX spectra and SAED, we identified some mineral grains more precisely, in particular from the rind and adjacent zones (more external areas of the intermediate zone), thus establishing the typology of phyllosilicates presented in Table 2. The most frequent spectra were those of beidellite and

montmorillonite, while those of paragonite, pyrophyllite and chlorite were very rare. From all the structural formulae calculated, we selected those we considered most representative of the species concerned. These were classified following the criteria of Weaver and Pollard (1973), Borchardt (1989) and Meunier (2005).

Other minor minerals are of interest as they indicate both the origins of the aerosols and the atmospheric alteration processes of either individual dust grains or iberulite genesis. We thus have some minerals considered primary, which are resistant to alteration and probably originated in highly weathered soils (rutile, ilmenite, grossular, hematites, aluminum oxide-hydroxide and amorphous iron oxides), or which may be related to volcanic rocks (calcium amphibole, monticellite). Another group of minerals could be related to phosphate deposits in the Western Sahara (Bu-Craa).

HRTEM micrographs of iberulite rinds from each event show an important quantity of small individualized crystallites of several minerals smaller than 0.5 μm. Fig. 13 shows iberulite rinds of an event. In these images, smectite particles can be observed whose crystallites are arranged in a more or less disorderly stacking (tactoids or quasicrystals), forming the relatively thick walls of a polygonal network. Micrograph A shows honeycomb smectite (triangular net-
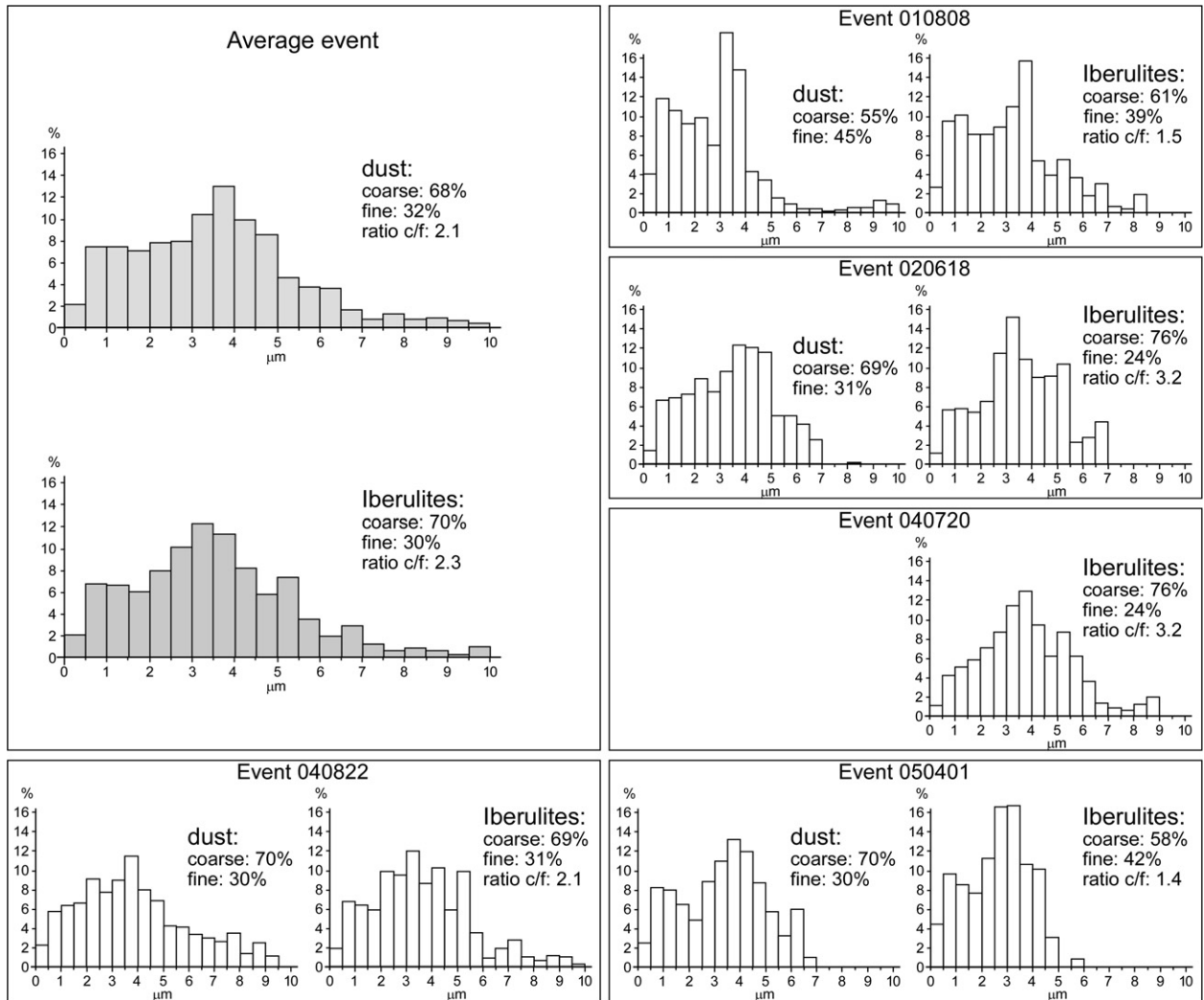
Fig. 10. Particle size distribution of iberulite constituents and dust Average event was obtained by averaging the data of the other events. Fine particles are Dp < 2.5 μm, and coarse particles Dp > 2.5 μm, based on the volume distribution (Seinfeld and Pandis, 2006).

work), where incipient alteration of smectite to amorphous silica and gypsum can be inferred and chlorides can also be seen, while micrograph B1 shows smectite or amphibole alteration to alunite.

4. DISCUSSION

Iberulites were first encountered in August 1999 (Díaz-Hernández, 2000) and continue to be collected at the time of writing. This indicates that their appearance is not accidental, but responds to discontinuous natural phenomena. The lack of previous references to iberulites may be due to (1) the most commonly used sampling methods; (2) the fact that they are exclusive to the study region and/or (3) because previously non-existent environmental conditions are conducive to their formation. Loÿe-Pilot et al. (1986) and Guerzoni and Chester (1996) presented papers focusing on African dust transport and impact centering on the Mediterranean basin, but did not mention iberulites, or anything similar. None of the LITE, MINOS, MIN-

ATROC, SAMUM and SHADE field experiments have reported any descriptions of particles similar to iberulites.

Satellite imagery (MODIS for example) can only monitor the evolution of Saharan air masses loaded with dust (plumes) over large sampling periods (Fig. 14) because the satellites only retrieve total optical thickness from the measured radiances.

On the other hand, it is well known (e.g., Alarcón et al., 1995; Díaz-Hernández and Miranda Hernández, 1997; Moulin et al., 1998; Escudero et al., 2005) that in the western Mediterranean basin, the highest levels of airborne dust additions to soils generally occur when powerful, advective, high-dust Saharan air masses penetrate into the troposphere and are transported over the Iberian Peninsula (many times across the eastern Atlantic Ocean, Fig. 14) mainly from May to September, induced by anticyclonic activity over the eastern or southeastern Iberian Peninsula, and more sporadically in January, February and October (Figs. 1 and 2). During this transport, atmospheric processing of this material could occur, because these periods coin-

		Qz.	Dol.	Cal.	Gyp.	Hal.	Illi.	Beid.	Hem.	Kaol.	Mont.	Feld.
010808	D.	31	45	12	4	1	2	1	1	1	1	1
	Ib.	63	7	7	5	4	4	3	3	2	1	1
020618	D.	39	36	11	4	2	3	1	1	1	1	1
	Ib.	32	4	38	8	5	2	4	3	2	1	1
040720	D.	33	45	9	4	2	2	1	1	1	1	1
	Ib.	53	6	17	5	5	4	3	3	2	1	1
040822	D.	32	42	7	6	4	2	2	2	1	1	1
	Ib.											
050401	D.	44	43	3	2	1	3	1	1	1	1	1
	Ib.	61	3	7	6	10	4	2	3	2	1	1
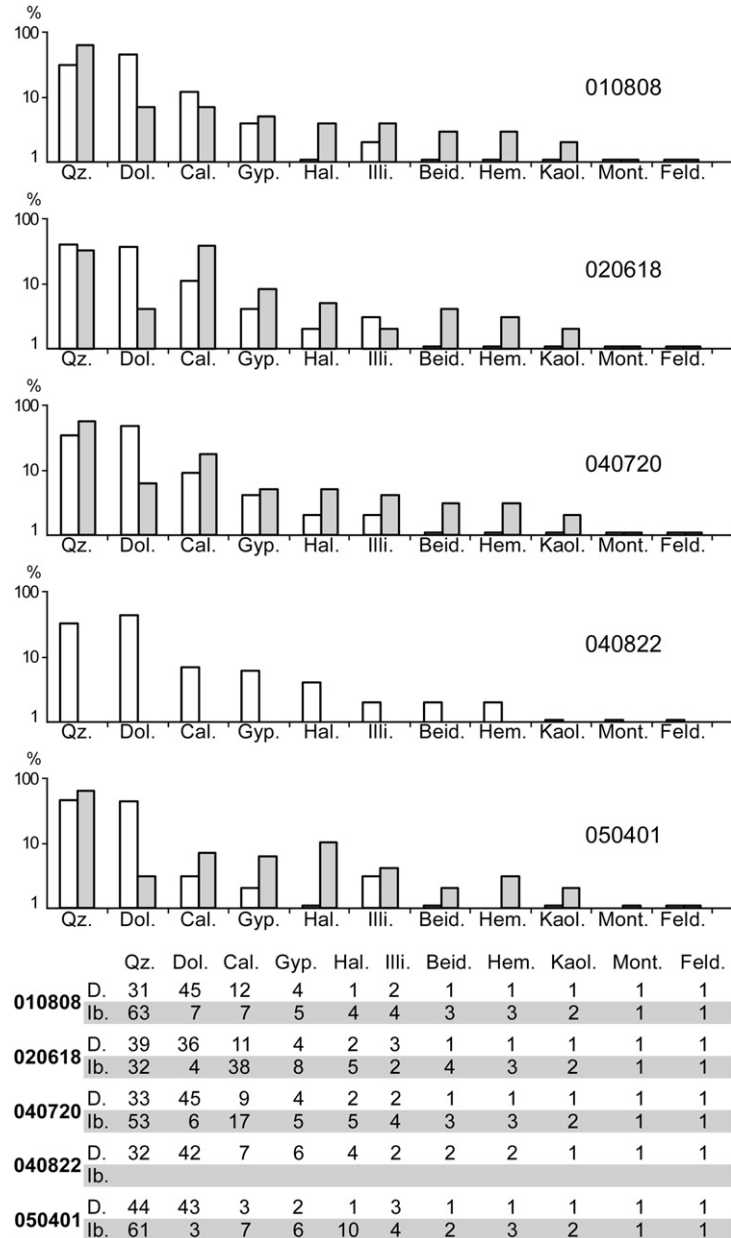
Fig. 11. Mineralogical composition (XRD) of iberulites (Ib) and associated dust (D) from each event. Contents are given on a logarithmic scale. Qz, quartz; Dol, dolomite; Ca, calcite; Ill, illite; Ka, kaolinite; Ha, halite; Gy, gypsum; Mon, montmorillonite; Hm, hematite; Ab, albite; Bei, beidellite.

cide with the collection times of iberulites. In the January–June period, this dust transport is mainly caused by cyclonic activity over western or southern Portugal (Rodríguez et al., 2001; Alpert et al., 2004; INM).

In addition, a considerable increase of red rain episodes has been recorded in the western Mediterranean basin since the 1980's (Quereda et al., 1996; Avila and Peñuelas, 1999; Avila et al., 2007). We too have recorded this phenomenon between 2000 and 2006, with the following variability: 2000 (3 episodes), 2001 (7), 2002 (7), 2003 (1), 2004 (10), 2005 (11) and 2006 (7). Fig. 3 shows microscope images of drop impacts from one of these rain episodes, with 2005 in particular being the driest year in Spain since 1887 (INM).

We have also observed that all the red rain episodes were closely associated with hazes, although not all the hazes were accompanied by red rain, and the iberulites were collected during this warm weather. These hazes were not local or even regional, but coincided with Saharan heat waves affecting at least all of the southern Iberian Peninsula. The water for these red rains generally comes from thermal lows or summertime extratropical convective precipitations (one of the major moisture sources) due to evaporation from the land surface (Barry and Chorley, 1998; Fig. 14A and B). However, in spring or autumn, the water can occasionally come from cooler, moister Atlantic fronts (Avila et al., 1998; Fig. 14C).
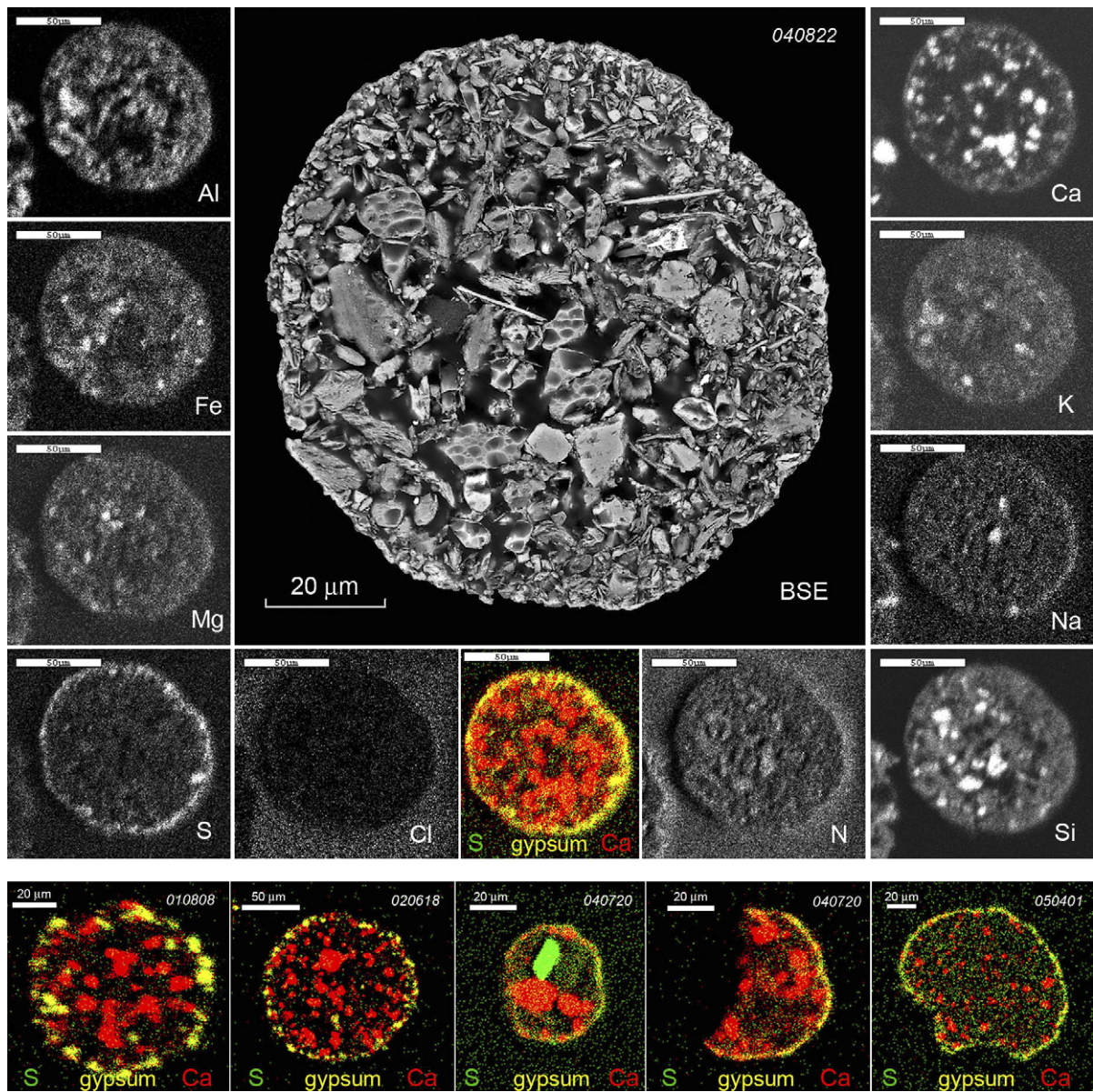
Fig. 12. Element (Al, Ca, Cl, Fe, K, Mg, N, Na, S and Si) fingerprints of a polished iberulite (central backscattered electron image) using microprobe X-ray mapping. Note that Cl and N do not present fingerprints, and S + Ca fingerprints would give the calcium sulfate (gypsum) distribution. Bottom line shows the fingerprints of gypsum in the studied events. Note that the central micrograph presents a lazurite crystal (green color).

The iberulites collected in all the events were produced in both wet deposition (red rain) and dryfall contexts. The images in Fig. 3 show a possible connection between the specimens collected during a red rain episode (dust, muddy raindrops and iberulites). The micrograph sequence shown (B–H) indicates a decrease in water content of the muddy raindrops, which would be minimal in the case of the iberulites (which, together with the dust, would be the smallest objects in micrograph A). The muddy raindrops in photos E–H could have become iberulites if their water had evaporated before reaching the ground. All of this could indicate physical interaction between soil particles and water droplets.

4.1. Hypothesis

Our interpretation of the morphological, structural and compositional properties of iberulites will lead to an understanding of their formation mechanisms.

4.1.1. Morphology of the Iberulites

Iberulite morphology shows that sphericity is a common feature, similar to that found in other types of particles produced in different media. Regarding the atmosphere, particle aggregation phenomena are common, occurring as irregular, internally mixed minerals of terrestrial and marine origin with no patterns of structural organization

Table 2
Phyllosilicates in iberulite rind detected by TEM-EDX microanalysis[a]

Species	Elemental composition	Structural formulae
Phyllosilicates from smectite rind		
Beidellite	Si, Al, Mg, Fe, Na, Ca, K	$[Si_{3.79}Al_{0.21}] O_{10} (Al_{1.83} Mg_{0.03} Fe_{0.17}) (OH)_2 Ca_{0.10} Na_{0.12}$
Montmorillonite	Si, Al, Mg, Fe, K, Ca	$[Si_{3.98}Al_{0.02}] O_{10} (Al_{1.23} Mg_{0.55} Fe_{0.31}) (OH)_2 Ca_{0.03} K_{0.19}$
Di-trioctahedral smectites	Si, Al, Mg, Fe, Ca, K	$[Si_{3.66}Al_{0.34}] O_{10} (Al_{0.50} Mg_{0.99} Fe_{0.88}) (OH)_2 Ca_{0.09} K_{0.07}$
Magnesian smectites	Si, Al, Mg, Fe, Ca, K	$[Si_{3.80}Al_{0.20}] O_{10} (Al_{0.68} Mg_{1.53} Fe_{0.32}) (OH)_2 Ca_{0.03} K_{0.02}$
Magnesic-ferric smectites	Si, Al, Mg, Fe, K	$[Si_{3.76}Al_{0.24}] O_{10} (Al_{0.68} Mg_{0.80} Fe_{0.85}) (OH)_2 K_{0.09}$
Illite	Si, Al, Mg, Fe, K	$[Si_{3.65}Al_{0.35}] O_{10} (Al_{1.62} Mg_{0.18} Fe_{0.14}) (OH)_2 K_{0.50} Na_{0.17}$
Paragonite	Si, Al, Mg, Fe, Na, K	$[Si_{3.66}Al_{0.34}] O_{10} (Al_{1.61} Mg_{0.07} Fe_{0.21}) (OH)_2 Na_{0.39} K_{0.32}$
Pyrophyllite	Si, Al, Mg, Fe	$[Si_{3.97}Al_{0.03}] O_{10} (Al_{1.96} Mg_{0.03} Fe_{0.02}) (OH)_2$
Kaolinite[b]	Si, Al, Mg, Fe, K	
Chlorite + Smectite[b]	Si, Mg, Al, Fe, Ca	

[a] Major minerals are not shown as they were previously recognized by XRD and SEM-EDX.
[b] Formulae not determined because of Al volatilization in the first case, and because the second is a mixture.
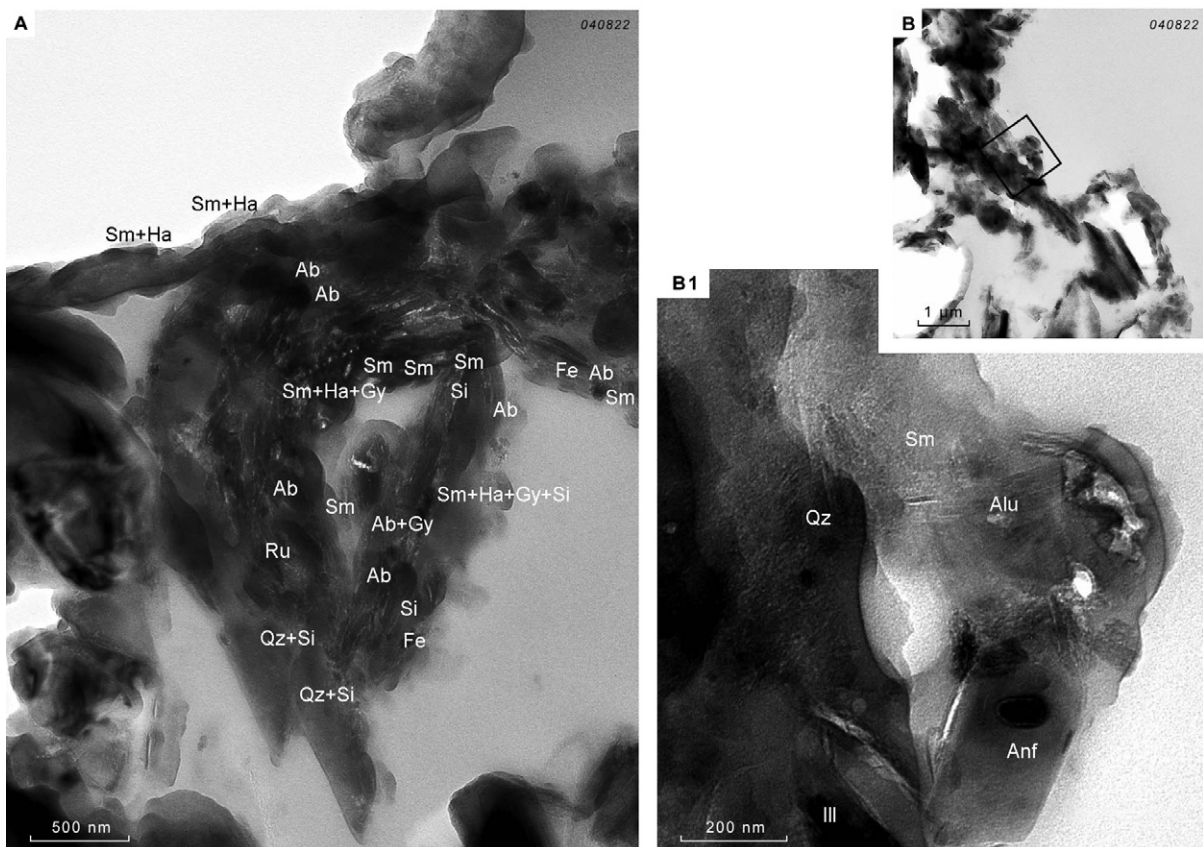
Fig. 13. Arrangement of smectite particles and other minerals in the rind, observed using HRTEM images of iberulite sections. The A microfabric shows moderate alteration with atmospheric neoformation products: the inner part of the rind is more altered (gypsum and amorphous silica) than the outer (only halite), while the B1 microfabric is strongly altered: an incipient alunite crystallite emerges by starting to crystallize in an amorphous smectite (gel). Qz, quartz; Si, amorphous silica; Sm, smectites; Ab, albite; Fe, iron oxides; Ha, halite; Gy, gypsum; Alu, alunite; Ill, illite; Ru, rutile; Amp, amphibole.

(e.g., Andreae et al., 1986; Buseck et al., 2000). All of these forms are different from iberulites. One distinctive feature of iberulites separating them from all of these spheroids and aggregates is the vortex, whose origin is not due to the random nature of other phenomena (erosion, impact, ejection, etc.), but is related to iberulite genesis and is common to all of them.

Beard and Chuang (1987), Beard et al. (1989) and Pruppacher and Klett (1997) studied morphologies with similar vortices to those of iberulites in the context of airflow around circulating water droplets: this suggests that water droplets could act as precursors for iberulites, together with the associated mechanisms. These authors examined the drop shapes and established that the drops clearly maintained their sphe-
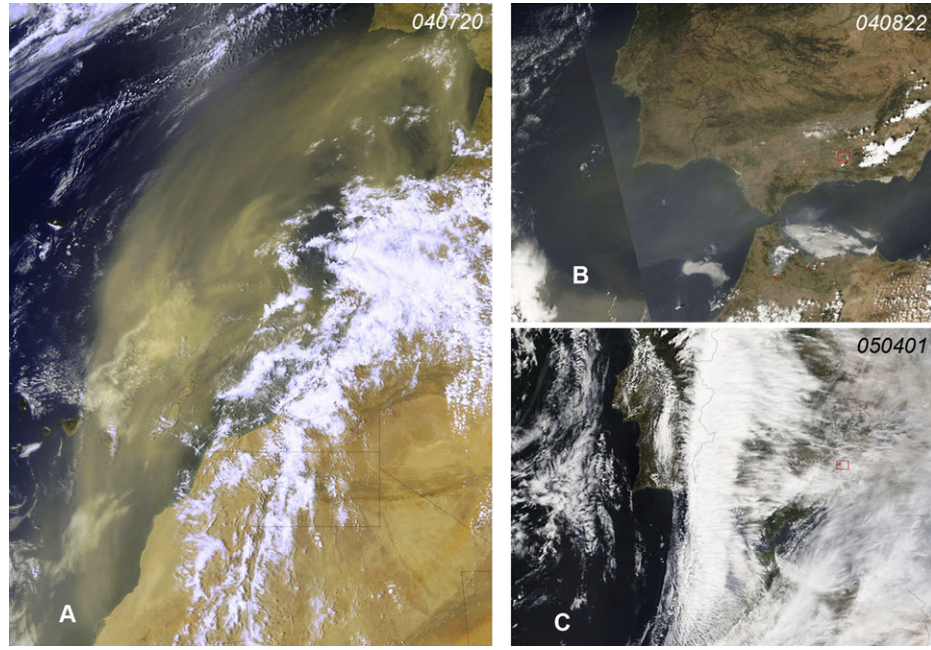
Fig. 14. MODIS images of the transport of Saharan dust towards the Iberian Peninsula. These images represent three types of dust intrusion, with different densities of aerosols and different cloud cover. The image with highest cloud cover (April 2005) gave the highest deposition rate and preceded a red rain episode. Image courtesy of MODIS Rapid Response Project at NASA/GSFC (Dr. J. Schmaltz); see http://visibleearth.nasa.gov/Atmosphere/Aerosols/Dust_ash_2.html (MODIS: Moderate-resolution Imaging Spectroradiometer). Squares show the sampling zone. (A–C) Events of the date labels (see Table 1).

ricity up to a radius of $a = 500$ μm, when a breakup mechanism started, beginning with drop base flattening and an increasingly large concave depression until the equivalent radius reached 4.5 mm. This can be observed in the raindrop impacts shown in Fig. 3. Micrograph A presents a large variety of impacts, with varying sizes and subcircular shapes; all are less than 1 mm in diameter. Sequences E–H shows the traces of raindrops decreasing in size, with the smallest having equidimensional axes.

As iberulite sphericity is high, their formation mechanisms could be linked to the processes undergone by water droplets not passing the aforementioned 500 μm radius threshold. On the basis of the studies of Le Clair et al. (1970, 1972), Pruppacher and Beard (1970) and Lin and Lee (1973), we understand that the precursor water drops of the iberulites should have a size range of 150 μm < a < 500 μm (Reynolds number regimes 20 < N_{Re} < 300), corresponding to the conditions in which the standing eddy at the downstream end of the water drop (rear) forms as a result of the wake produced by the drop in free fall. In this setting, a water sphere falling in air has vigorous internal circulation with a stagnation ring slightly upstream of the equator; a simultaneous reverse circulation towards the rear of the sphere develops for 100 < N_{Re} < 300 (i.e., 300 < a < 500 μm). In these conditions, a vortex could form in the tail of a falling precursor water drop, and in both its formation and its fall it could trap dust and other drops. The extent of development of this vortex would be conditioned by the strength and size of the wake, which increases according to the Reynolds number. The iberulite in Fig. 6A shows an example of this vortex.

Although the average diameter of the specimens collected is 60–90 μm, the larger sizes were probably deposited before reaching the sampling station.

4.1.2. Structure and particle-size distribution in iberulites

SEM images show that most of the iberulites from all events have the same structural pattern of three different parts, following the model shown in Fig. 15: the core (tens of microns), a medium layer, and a thin (a few microns) outer rind, considering particle size, the thickness of each layer and its composition.

Beard and Grover (1974) and Grover and Pruppacher (1985) suggested that for $N_{Re} \geqslant 30$ ($a \approx 200$ μm) droplets, small particles (<1 μm) captured by the standing eddy on the downstream side of the drop are favored by gravity pulling them toward the rear of the drop (wake capture), whereas relatively large particles (>1 μm) may be captured on the upstream lower side of a falling drop (front capture). Both capture effects would strongly increase with increasing collector radius of precursor water drops and so trap other dust particles and drops (Pinsky et al., 2001). This is consistent with our observations, as the highest concentration of fine particles is found on the upper hemisphere of the iberulites, acting as a crust or rind around the vortex. On the other hand, coarse particles concentrate more on the lower hemisphere, mainly trapped by the lower side of the iberulite (Fig. 6A,C and D).

It therefore appears that the iberulites collected represent the last stage in precursor water drop evolution. Once the water drop–dust grain (colloidal suspension) system is set up, the hydrodynamic phenomena affecting the precursor

	Smectite rind (1)	Granular body (2)
Quartz	□	**
Carbonates	○	**
Clay minerals	**	○
Aluminosilicates	*	**
Sulfates	**	□
Halures	*	□
Iron oxides	**	*

□	rare
○	occasional
*	frequent
**	very frequent
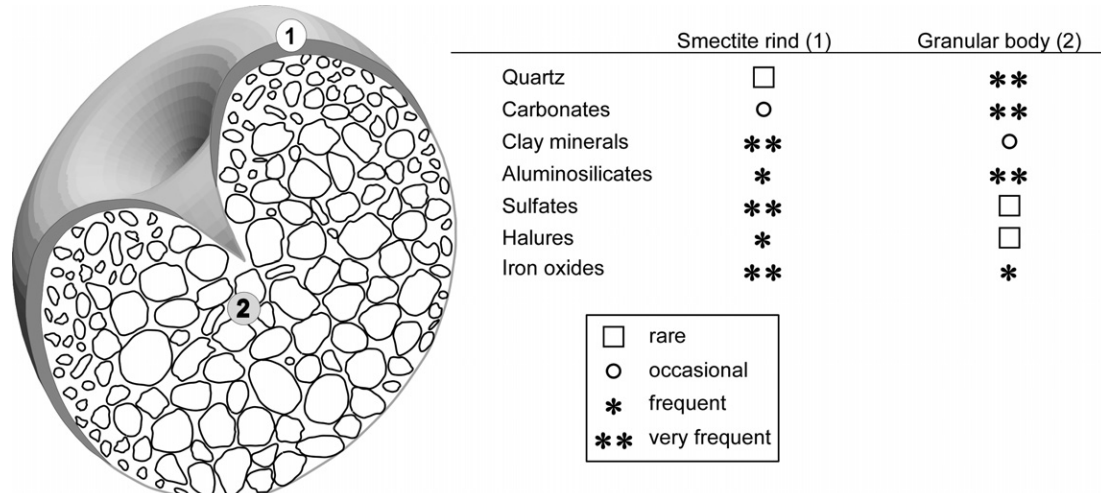
Fig. 15. Sketch of a cross-sectioned pinkish mineral microspherulite (iberulite) showing its internal organization based on morphological features, mineralogy and the types of microfabrics. Three zones are distinguished: smectite layer (rind) and granular body (core and intermediate zone).

water drops during fall produce important regimes of internal circulation inside them (Le Clair et al., 1972; Pruppacher and Klett, 1997), reaching maximum internal velocity near the drop surface. These regimes move the constituent particles according to their inertia: the most mobile are the smallest, tending to become located in the rind, while the largest and heaviest remain in the core and intermediate zone. The components of the core and intermediate zone have no cementing matrix, but, because of their colloidal nature, have moderate ζ-potential surface charges, so that when new particles are captured by a water drop, electrical repulsion exists between them due to this interfacial charge, although this may not prevent weak flocculation in the drop (Hunter, 2000). This explains the high porosity and the ease with which the iberulite disintegrates when manipulated or wetted. Nonetheless, the rind does have a cementing matrix consisting of minerals of laminar habit (phyllosilicates) connecting small mineral grains; amorphous and crystalline iron oxides are also linking agents of the rind constituents.

We can thus define an iberulite as a coassociation with axial geometry, made up of well-defined mineral grains together with non-crystalline compounds, structured on a coarse-grained core and a pinkish smectite rind with only one vortex.

4.1.3. Mineralogical transformation processes on the smectite layer (rind) of the iberulites

EDX spectra and images taken of each of the iberulite parts show a greater abundance of mineral species in the rind than in the core. This could be attributed to a profusion of heterogeneous and multiphase reactions in the smectite rind, which has a special distribution due to the thinness and flexibility of the crystallites. Their aggregates form "honeycombed" structures in which water can be found in various states (Meunier, 2005). These clay suspensions become true gels trapping large amounts of water in the pores of the alveolar structure (Figs. 6A and D1, and 13A).

The successive processes described below would occur in a final stage of the evolution of precursor water drops to iberulites, when they are already structured and formed, with an aqueous phase restricted to the more hygroscopic smectite coating, as opposed to an almost dry core.

The non-silicate minerals found in the rind are mainly sulfates (gypsum and to a lesser extent alunite-jarosite and other mixed sulfates), sodium and calcium chloride, amorphous silica and amorphous iron oxihydroxide. The SEM images show the chlorides to be generally well crystallized (idiomorphs) (Fig. 9A1 and B), whereas the sulfates (except for those shown in Fig. 9C) are present as pulverulent masses, flakes or, in most cases, impregnations (Fig. 13). The occurrence of chlorides and sulfates in the core is minimal. This leads us to think that the presence of these minerals could be the result of two distinct, consecutive processes in the atmosphere: first H_2SO_4 attack, and second the incorporation of sea salt into the outermost layer of the iberulite rind.

In our case, the H_2SO_4 could have three origins: (a) condensation of gaseous sulfuric acid on iberulite surface; (b) absorption of atmospheric SO_2 into liquid water droplets in clouds, which would be deposited directly on the iberulite surface; and (c) SO_2 could be both absorbed onto some particle surfaces (such as quartz grains, feldspars and calcites; Fig. 13), and spread to alveolar smectite compartments, whose water would have an alkaline pH (data not shown). This would provide a suitable chemical environment for the aqueous-phase conversion to H_2SO_4 (Seinfeld and Pandis, 2006). In addition, due to the ease with which smectites swell, the SO_2 could enter more easily into the interlaminar space since the surface area of the smectites increases (Borchardt, 1989). Adsorption of SO_2 to active sites with hydroxyl groups (octahedral sheets) would occur in the hydrated interlaminar space and on the edges of the clays, causing irreversible oxidation to sulfuric acid. Ozone and metal components (Fe and Ti) would act as catalyzers and the high pH would make the oxidation reaction proceed at a

substantial rate (Usher et al., 2003). This would lead to the rapid transformation of some primary minerals into products of atmospheric neoformation (secondary minerals): the gypsum crystals would be mainly the product of H_2SO_4 attack on the interlayer cations of the smectites (Table 2). Once these cations are consumed, acid attack could continue to destroy the octahedral and tetrahedral sheets of the smectites and other phyllosilicates (illite and kaolinite, among others), creating mixed sulfates (Andreae et al., 1986). The alunite-jarosite found in the smectite rind would be of similar origin. The alunite could also come from acid attack on orthose or amphibole grains (Fig. 13B1), while the jarosite could be produced by acid attack on Fe- and K-rich phyllosilicates. If acid attack progresses further, the phyllosilicate grains would be completely destroyed, producing the amorphous silica and Fe observed in the TEM-SAED. The lazurite could come from the source area or could also have been formed in the atmosphere by sulfuric acid attack on a grain dust silicate (Fig. 12, central micrograph in the bottom row).

The incorporation of sea salt into the outermost layer of the rind would probably occur at the same time as that of biogenic planktonic exoskeletons. Since these have no signs of corrosion, they must have been incorporated after the acid attack described above (Fig. 8C, C1 and C2). As observed in Fig. 9A and B, the sea salts are adhered to the iberulite surfaces and thus are not the result of atmospheric neoformation reactions on other components, nor are they the result of internal mixing of NaCl and original dust particles (they do not appear in the core).

4.1.4. Space–time sequence of iberulite formation in the troposphere

Satellites provide an excellent picture of dust transport on the global scale (Prospero et al., 2002). The most prominent features in Fig. 14 are the large plumes stretching from the Sahara and Sahel towards the west coast of Africa and then shifting towards the Azores, Gulf of Cadiz and southern Iberian Peninsula. The MODIS images chosen correspond to summer 2004 and spring 2005 and are the most representative of the events associated with iberulite formation. The MODIS image in Fig. 16 clearly illustrates the framework of the process, even though only a few iberulite specimens were collected at the monitoring station during this event (5–8 March 2004) (Fig. 2). Other trajectories exist (Fig. 14), but this one is frequently observed.

Mineralogical composition enables us to establish the relationship with the likely source areas (Fig. 16, label 1), which are the same as those established by other authors in North Africa, mainly consisting of arid soils and standing out as the strongest and most persistently active dust sources (Glaccum and Prospero, 1980; Goudie and Middleton, 2001; Prospero et al., 2002 and references therein).

The major minerals of the arid soil surface on a global scale (Claquin et al., 1999) are quartz, feldspars, illite, smectite, carbonates, gypsum, and iron oxides both for the clay and silt fractions, as well as our iberulites. The presence of mineral assemblages like quartz, dolomite and calcite is a good indication of Saharan origin (Avila et al., 1997), while a composition of mainly smectites and illite suggests an origin in the Aridisols of central Algeria and eastern Morocco,
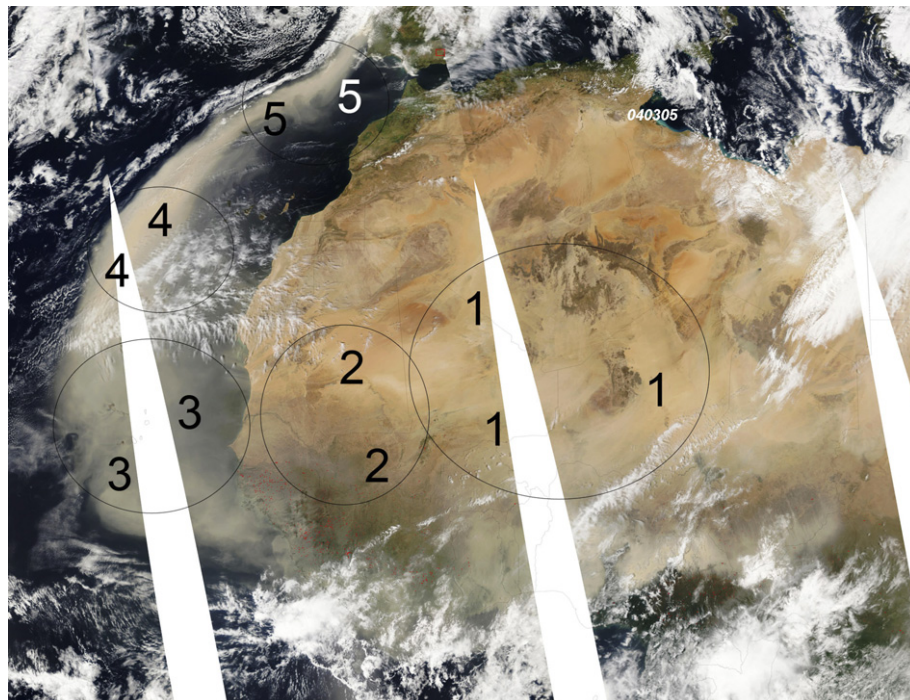
Fig. 16. MODIS image of a dust plume trajectory (pink) from its source area (Central Sahara-Sahel) towards the Iberian Peninsula, over the Atlantic Ocean. This is one of a sequence of images taken over four days during which the evolution of this aerosol mass was followed. The dust mass passed above the clouds between Cape Verde and the Canary Islands and, on descent, converged with the depression centered west of the Iberian Peninsula at a similar altitude, finally shifting towards the Mediterranean. In this case only small amounts of iberulites were collected. For additional details about labels, see text. Image courtesy of Dr. J. Schmaltz, NASA/GSFC.

including the southern slopes of the Saharan Atlas Mountains (Paquet et al., 1984; Prospero, 1999). Kaolinite is more abundant in dust from the lower latitudes of West and Central Africa. Bearing in mind these references, the mineral components of the iberulites studied in this paper may have the same origins. The higher dolomite content in the dust compared to the iberulites suggests possible local contamination of this mineral, suggesting that the iberulites formed before reaching the sampling station.

The coatings of iron oxides and iron oxide domains in the internal mixtures of iberulites must proceed from the soils (Ferralsols) of the source area as free oxides (hematite) or as oxides adhering to the clay minerals, calcite and quartz (Lafon et al., 2004). North African dust contains appreciable quantities of iron (Jickells et al., 2005): the pinkish color can be attributed to these iron coatings.

Pokras (1991) and Romero et al. (2003) reported remains of silica diatom shells in dust samples. Their presence in the interior of iberulites establishes different source areas, like the Central and Western Sahara and Sahel, especially the northern region in the Bodelé Depression (Washington et al., 2006). Dry lake beds around Lake Chad contain fine particulate matter (particulate organic matter, minerals and diatoms) that is easily picked up, eroded and transported by wind.

Dust is carried from the Sahara within a mixed layer called the Saharan Air Layer (SAL), which typically rises to 500 mb (6 km, Kishcha et al., 2003; Alpert et al., 2004). Its base is near the surface over the Central to West Sahara, but it rises rapidly in a westward direction (Fig. 16, label 2) to be transported far offshore.

During transit in the atmosphere (several days, often a week or more, Prospero (1999) and MODIS), the dust can be transported thousands of kilometers by winds. Studies of dust mobilization in soils from arid regions show that particles <10 μm in diameter can be released in large numbers, but the 5-μm mode is attributed to long-distance transport (Gillies et al., 1996). This is our case (Fig. 10).

Once over the Atlantic Ocean, these large, dense masses of dust fly towards the Canary and Azores archipelagoes (Fig. 16, label 3). Because of the high concentration of dust (our average event has 32% fine and 68% coarse), many small cloud droplets nucleate that coalesce inefficiently into raindrops (Rosenfeld, 2000; Rosenfeld et al., 2001), i.e., the more cloud droplets there are, the smaller they will be and also much less likely to collide with each other and create precipitation (Toon, 2003). However, this would not prevent some cloud droplets of about 2–30 μm radius from coalescing (the minimum size required for the onset of precipitation is about 20 μm; Pruppacher and Klett, 1997). These authors determined that 12–24 min are necessary to form raindrops with radii of about 100 μm, starting from a droplet spectrum centered at about 10 μm. The water droplets formed in these circumstances would be precursors of iberulites, as explained in Sections 4.1.1 and 4.1.2. This implies that the cloud droplets contain very fine dust grains partly originating in nucleation (CCN), but that this load can increase by impaction scavenging. During fall, they would reach terminal speed with a more or less acute horizontal component (Fig. 16, label 3). According to Andreae

et al. (1986), droplets in marine cumuli have lifetimes ranging from 17 min to 3 h, which allows for the incorporation of new mineral particles. It is likely that in this stage, local (marine) muddy rain can occur, similar to that described in Fig. 3.

Simultaneously, there could be interaction between conducting water drops, charged aerosols and the atmospheric electric field in a fair weather situation (<150 Vm^{-1}, Harrison (2004)). Complex hydrodynamic and electrostatic interactions occur affecting the collision efficiency of $150 \leqslant a \leqslant 600$ μm water drops in air and aerosol particles of up to 3 μm radius (Grover and Beard, 1975). Thus, rear collision through the vortex between electrically charged drops and particles is more likely. Gay et al. (1974) found that 300 μm water drops falling in an electrified field between 25 and 40 Vm^{-1} at 20 °C and 1013 mb experienced upward motion (experiencing a combined gravitational and electrical force of mg ± QE, where m = mass, Q = drop charge and E = vertical electrical field). This increases the atmospheric residence time. Also during fall, the water in the drop evaporates, which is a *sine qua non* condition for iberulite formation; the loss of mass would cause a gradual loss of speed. Evaporation can occur either because the precursor water drop leaves a cloudy region or because it falls to lower, warmer levels of the troposphere. When it is practically dry (in a matter of minutes), only the weakly bound mineral components remain, many of them highly porous (Fig. 8B), with a thin layer of laminar minerals on the periphery, mainly on the hemisphere containing the vortex and with the structural configuration caused by the hydrodynamic phenomena explained above. Overall, their bulk density is very low (0.65 grains/cm^3 and porosity about 50%), so they could act as flying spheres, possibly able to remain in the air for a long time and cover large distances (Fig. 16, label 4). During this transport, the smectite rind may retain some water or rehydrate because of its high degree of hygroscopicity. At this point, the iberulites would be completely formed, but would have not yet acquired the compositional maturity observed after collection due to the absence of mineral species later detected in the smectite layer. According to Glaccum and Prospero (1980), the dust does not contain any primary halite or gypsum. During the precursor water droplet stage, water action could cause the virtual dissolution of mineral cations. However, since the initial mineral phase (mainly silicates and carbonates) has low solubility, and environmental humidity should not, in theory, supply a high saline load at high altitudes as it is still above the marine boundary layer (MBL), it could be expected that these iberulites would not yet have the peripheral saline minerals observed. Otherwise, these salts would be evenly distributed throughout the microspherulite body and not in specific areas. However, we can see that the salts are preferentially located in the rind, particularly in the case of sulfates and chlorides, with the former beneath the latter (see 4.1.3 and Figs. 9 and 13).

The non-sea-salt sulfates (NSS: gypsum, alunite-jarosite, among others) were probably not incorporated into the iberulites like the conventional sea-salt sulfates, but would be neoformed minerals in the iberulite rind before deposition of the sea salt: they are mainly found as an outer fringe

on all iberulites in all events (Fig. 12, bottom row of micrographs) with identical distributions on the smectite rind. The process causing this sulfate fringe would occur on the outside of immature iberulites by gas-iberulite transfer reactions and heterogeneous oxidation of SO_2 (see Section 4.1.3). As the carbonate planktonic skeletons are well preserved, they would not yet have been incorporated into the iberulite surface at the time of the reaction. The minerals of the iberulite interior (especially the carbonates) would therefore not undergo acid attack, as the core is already dry (no corrosion or coating has been observed).

The presence of NSS in the iberulites of all the events studied requires transit through areas with high content of atmospheric sulfur species (Fig. 16, **label 4**). We must discard anthropogenic emissions due the geographic context in which the immature iberulites are moving. Alternatively, there are two main sources of sulfur: the volcanic context of the Canary, Madeira and Azores archipelagoes, which supplies a background of diffuse and continuous emissions, and oceanic dimethyl sulfide (DMS). However, Wang et al. (1995), Thornton et al. (1997) and Raes et al. (2000) suggest that DMS contributes only 1–10% of the SO_2 in the upper troposphere in the Northern Hemisphere. Given that the trajectory of the immature iberulites carries them over the MBL at altitudes of around 5 km, they would come into contact with the SO_2 emissions from these archipelagoes, which in most cases concentrate in the upper part of or far above the MBL (Graf et al., 1997).

SO_2 accumulation is therefore probable in the vicinity of the Teide stratovolcano (3710 m ASL). During the ACE-2 campaign over the Canary Islands area, de Reus et al. (2000) observed a marked decrease in ozone concentration linked to high mineral dust concentrations. This means that dust surfaces provide a sink for the direct removal of ozone; ozone depletion would in turn boost SO_2 oxidation (Gobbi et al., 2000; Usher et al., 2003). In our case, the iberulite smectite rind would appear to be the most efficient sink, as the sulfate content of iberulites is higher than that of dust (Fig. 11).

Having flown over the Canary Islands, the plume would continue to descend gradually towards the MBL (850 mb, ~1.5–2 km, Formenti et al., 2003; Alpert et al., 2004). This would imply a 22% increase in collision efficiency of drops with sea salts for a change in ambient conditions (995 mb, 14 °C to 800 mb, 25 °C, De Almeida, 1977), reaching their final maturation (Fig. 16, label 5).

These chlorides could therefore originate in the sea-salt particles that either precipitated onto the iberulite surface or adhered to the smectite layer as idiomorphous crystals because of their hygroscopicity (Fig. 9A and B). Redissolution processes have also been observed in these salts (data not shown). Sea-salt supply would thus occur at the same time as the incorporation of the planktonic organisms found on the iberulite surfaces (Fig. 8C), adding weight. We do not detect any signs of acid attack on these biogenic skeletons because the SO_2 concentration in the MBL (from the DMS) must be much lower than in label 4.

This stage (iberulite maturation) could take place over the triangle formed by the Canary Islands, the Azores and the Iberian Peninsula. Specifically, we have observed (Figs. 14 and 16) that masses of dust frequently enter and

remain stationary in the Gulf of Cadiz before entering the Iberian Peninsula.

Finally, in the atmosphere of the southern Iberian Peninsula, these dust plumes containing iberulites could both produce a dryfall or become associated with local red rains (wet deposition) when supplied with more humidity from summer cumulo-nimbus formation. The muddy raindrops of the red rains observed in Fig. 3 would form over the sampling station and could be considered aborted potential iberulites, lacking many of the attributes mentioned above. It is possible that gravitational settling may have sedimented larger iberulites before reaching the sampling station.

As already suggested, the mechanisms most likely to produce iberulite morphology are based on the theory of fluid mechanics (Pruppacher and Klett, 1997). However, other alternative hypotheses, single or combined (electrorotation, Kelvin–Helmholtz and Von Karman vortices), could be considered to cause these vortex morphologies, although we believe that they do not fully explain these features.

5. CONCLUDING REMARKS

An iberulite is a new type of spherical aerosol particle collected in the southern Iberian Peninsula. It is internally mixed and structured, mechanically generated, with a diameter ranging from about 30 to 190 μm, with a low density ($0.65 \, \mathrm{g \, cm^{-3}}$) and about 50% mean porosity. Iberulites are different from classic atmospheric aerosols (<20 μm) (Seinfeld and Pandis, 2006). Because of their features, they probably have different physical and chemical characteristics than do other aerosol particles.

One of the important features of iberulites is that, together with the dust from which they are formed, they provide reaction sites for many heterogeneous reactions involving SO_2, HO_x, O_3, etc., bringing together other components and forming other minerals, as well as permitting aggregation.

On the basis of these facts, our interpretation is that iberulites are the result of atmospheric processing that could last several days. Their stages of formation, maturation and deposition can be summarized as follows:

1. Dust outbreak and elevation to the upper layers of the troposphere by the SAL.
2. Transport, size selection and flight over land and the Atlantic Ocean.
3. Formation of precursor water drops and gradual descent to lower tropospheric levels. This implies several processes that can be either simultaneous or consecutive (coalescence, formation of vortex, incipient downdraught).
4. Flight over areas with volcanic sulfur emissions (Canary Islands). Incorporation of SO_2 into the iberulite surface.
5. Descent to the MBL of the Iberian-Moroccan Atlantic and incorporation of sea-salt particles and plankton.
6. Final sequenced fall of mature iberulites onto the southern Iberian Peninsula.

The foregoing processes would give rise to the pinkish mineral microspherulites (iberulites), which can be consid-

ered complex (mixed) mineral assemblages formed in the atmosphere, are different from those found in other natural or anthropic ecological environments, and provide a particularly good opportunity to investigate relevant reactions in the atmosphere.

We consider that iberulites are tangible evidence of hydrodynamic theory applied to the interaction of water drops and dust particles, giving rise to shapes with a vortex that have until now been confined to and explained in laboratory studies.

6. FINAL CONSIDERATIONS

The key question is whether the newly recognized microspherules are abundant and/or distinctive enough to require changes in existing models for atmospheric dust deposition (at least in areas around the Mediterranean). For example, is there evidence that their formation has been increasing since 1992? Is there evidence that they accelerate the deposition of dust in unexpected ways, or do mass flux calculations indicate that they might? Alternatively, if iberulites do not influence the flux in a major way, do (or could) they play an important role in some other way, e.g. as a marker for environmental or paleoclimatic analyses (as long as they can be found fossilized in the stratigraphic record)?

Because the quantities of iberulites obtained in the sampling station range from 11% to 47%, could they have a non-negligible direct impact on the radiation budget at any point of their trajectory?

We do not know the frequency and magnitude of the processes involved in iberulite formation in the past and thus do not know if these additions of iberulites to the soils, particularly those of the Mediterranean, are another reason for their being different.

ACKNOWLEDGMENTS

This work benefited from discussions with Prof. B.M. Simonson (Department of Geology, Oberlin College, Ohio, USA), Dr. E. Reyes (Department of Isotopic Biogeochemistry, Consejo Superior de Investigaciones Científicas, Granada, Spain), Prof. A. Delgado (Department of Applied Physics of the Granada University, Spain), Prof. D. Martin (Department of Mineralogy and Crystallography of the Granada University, Spain) and Dr. J. Cuadros (Department of Mineralogy, the Natural History Museum, London). We thank the Technical Services of Granada University for the SEM and TEM images, especially Drs. M. Abad, I. Guerra and A. González, as well as A. Romero for extensive assistance with the illustrations .We are grateful to Prof. D. W. Parkin (Bath University, UK) for permission to reproduce micrometeorite images. We also wish to thank the Instituto Nacional de Meteorología for access to its database and the Spanish Ministry of the Environment for providing the records of station ES07. MODIS is a NASA project. Finally, the authors thank the associate editor and the anonymous reviewers for their constructive suggestions.

REFERENCES

Alarcón M., Alonso S. and Cruzado A. (1995) Atmospheric trajectory models for simulation of long-range transport and diffusion over the Western Mediterranean. *J. Environ. Sci.* **39**, 1973–1994.

Alpert P., Kishcha P., Shtivelman A., Krichack S. O. and Joseph J. H. (2004) Vertical distribution of Saharan dust on 2.5-year model predictions.. *Atmos. Res.* **70**, 109–130.

Andreae M. O. and Crutzen P. J. (1997) Atmospheric aerosols: biogeochemical sources and role in atmospheric chemistry. *Science* **276**, 1052–1058.

Andreae M. O., Charlson R. J., Bruynseels F., Storms H., Van Grieken R. and Maenhaut W. (1986) Internal mixture of sea salt, silicates, and excess sulphate in marine aerosol. *Science* **232**, 1620–1623.

Arimoto R. (2001) Eolian dust and climate: relationships to sources, tropospheric chemistry, transport and deposition. *Earth Sci. Rev.* **54**, 29–42.

Arroyo F. J. and Delgado A. V. (2002) Electrokinetic phenomena and their experimental determination: an overview. In *Interfacial Electrokinetics and Electrophoresis* (ed. A. V. Delgado). Marcel Dekker, New York, pp. 1–54.

Avila A. and Peñuelas J. (1999) Increasing frequency of Saharan rains over northeastern Spain and its ecological consequences. *Sci. Total Environ.* **228**, 153–156.

Avila A., Queralt-Mitjans I. and Alarcón M. (1997) Mineralogical composition of African dust delivered by red rains over Northeastern Spain. *J. Geophys. Res.* **102D18**, 21977–21996.

Avila A., Alarcón M. and Queralt-Mitjans I. (1998) The chemical composition of dust transported in red rains. Its contribution to the biogeochemical cycle of a holm oak forest in Catalonia (Spain). *Atmos. Environ.* **32**, 179–191.

Avila A., Alarcón M., Castillo S., Escudero M., Orellana J., Masque P. and Querol X. (2007) Variation of soluble and insoluble calcium in red rain related to dust sources and transport patterns from North Africa to northeastern Spain. *J. Geophys. Res.* **112**(D5), D05210.

Barry R. G. and Chorley R. J. (1998) *Atmósfera, Tiempo y Clima.* Omega, Barcelona, 441 pp.

Beard K. V. and Chuang C. (1987) A new model for the equilibrium shape of raindrops. *J. Atmos. Sci.* **44**, 1509–1524.

Beard K. V. and Grover S. N. (1974) Numerical collision efficiencies for small raindrops colliding with micron size particles. *J. Atmos. Sci.* **31**, 543–550.

Beard K. V., Feng J. Q. and Chuang C. (1989) A simple perturbation model for the electrostatic shape of falling drops. *J. Atmos. Sci.* **46**, 2404–2418.

Berstch P. M. and Seaman J. C. (1999) Characterization of complex mineral assemblages: implications for contaminant transport and environmental remediation. *Proc. Natl. Acad. Sci. USA* **96**, 3350–3357.

Borchardt G. (1989) Smectites. In *Minerals in Soil Environments* (eds. J. B. Dixon and S. B. Weed). Soil Sci. Soc. Am., Madison, WI, pp. 675–727.

Buat-Ménard P., Davies J., Remoudaki E., Miquel J. C., Bergametti G., Lambert C. E., Ezat U., Quetel C., La Rosa J. and Fowler S. (1989) Non-steady-state biological removal of atmospheric particles from Mediterranean surface waters. *Nature* **340**, 131–134.

Bücher A. (1994) Etude en Europe des retombées de poussières d'origine saharienne. *Rev. Geomorphol. Dyn.* **43**, 23–25.

Buseck, P. R., Cowley, J. M. and Eyring, L. (eds.) (1988) *High-resolution Transmission Electron Microscopy and Associated Techniques.* Oxford University Press, New York, 645 pp.

Buseck P. R., Jacob D. J., Pósfai M. and Anderson J. R. (2000) Minerals in the air: an environmental perspective. *Int. Geol. Rev.* **42**, 577–593.

Carrico C. M., Bergin M. H., Shrestha A. S., Dibb J. E., Gomes L. and Harry J. M. (2003) The importance of carbon and mineral

dust to seasonal aerosol properties in the Nepal Himalaya. *Atmos. Environ.* **37**, 2811–2824.

Claquin T., Schulz M. and Balkanski Y. J. (1999) Modeling the mineralogy of atmospheric dust sources. *J. Geophys. Res.* **104**, 22243–22256.

Crutzen P. J. and Andreae M. O. (1990) Biomass burning in the tropics: impacts on atmospheric chemistry and biogeochemical cycles. *Science* **250**, 1669–1678.

De Almeida F. C. (1977) Collision efficiency, collision angle and impact velocity of hydrodynamically interacting cloud drops: a numerical study. *J. Atmos. Sci.* **34**, 1286–1292.

de Reus M., Dentener F., Thomas A., Borrmann S., Ström J. and Lelieveld J. (2000) Airborne observation of dust aerosol over the North Atlantic Ocean during ACE 2: indications for heterogeneous ozone destruction. *J. Geophys. Res.* **105**(D12), 15263–15275.

Díaz-Hernández J. L. (2000) Aportaciones sólidas a la atmósfera originadas por un incendio forestal en el ámbito mediterráneo. *Est. Geol.* **56**, 153–161.

Díaz-Hernández J. L. and Miranda Hernández J. M. (1997) Tasas de deposición de polvo atmosférico en un área semiárida del entorno mediterráneo occidental. *Est. Geol.* **53**, 211–220.

Drees L. R., Manu A. and Wilding L. P. (1993) Characteristics of aeolian dust in Niger, West Africa. *Geoderma* **59**, 213–233.

Ducloux J., Delhoume J. P., Petit S. and Decarreau A. (1995) Clay differentiation in Aridisols of northern Mexico. *Soil Sci. Soc. Am. J.* **59**, 269–276.

Escudero M., Castillo S., Querol A., Avila A., Alarcón M., Viana M. M., Alastuey A., Cuevas E. and Rodríguez S. (2005) Wet and dry African episodes over eastern Spain. *J. Geophys. Res.*. doi:10.1029/2004JD004731.

Formenti P., Elber W., Maenhaut W., Haywood J. and Andreae M. O. (2003) Chemical composition of mineral dust aerosol during the Saharan Dust Experiment (SHADE) airborne campaign in the Cape Verde region, September 2000. *J. Geophys. Res.* **108**(D18), 8576. doi:10.1029/2002JD002648.

Frank A. and Kocurek G. (1994) Effects of atmospheric conditions on wind profiles and aeolian sand transport with an example from White Sands National Monuments. *Earth Surf. Proc. Land.* **19**, 735–745.

Franzen L. G., Hjelmroos M., Karllberg P., Brorstrom-Lunden E., Juntto S. and Savolainen A. (1994) The yellow snow episode of northern Fennoscandia, March 1991: a case study of long distance transport of soil, pollen and stable organic compounds. *Atmos. Environ.* **22**, 3587–3604.

Gay M. J., Griffiths R. F., Latham J. and Saunders C. P. R. (1974) The terminal velocities of charged raindrops and cloud droplets falling in strong electric fields. *Quart. J. Roy. Meteor. Soc.* **100**, 682–687.

Gillies J. A., Nickling W. G. and McTainsh G. H. (1996) Dust concentration and particle size characteristics of an intense dust haze event: inland delta region, Mali, West Africa. *Atmos. Environ.* **30**, 1081–1090.

Glaccum R. A. and Prospero J. M. (1980) Saharan aerosols over the tropical North Atlantic. *Mineral. Mar. Geol.* **37**, 295–321.

Gobbi G. P., Barnaba F., Giorgi R. and Santacasa A. (2000) Altitude-resolved properties of a Saharan dust event over the Mediterranean. *Atmos. Environ.* **34**, 5119–5127.

Goossens D. (1994) Effect of rock fragments on eolian deposition of atmospheric dust. *Catena* **23**, 167–189.

Goossens D. and Offer Z. Y. (1994) An evaluation of the efficiency of some eolian dust collectors. *Soil Technol.* **7**, 25–35.

Goudie A. S. and Middleton N. J. (2001) Saharian dust storms: nature and consequences. *Earth Sci. Rev.* **56**, 179–204.

Graf H. F., Feichter J. and Langmann B. (1997) Volcanic sulfur emissions: estimates of sources strength and its contribution to the global sulfate distribution. *J. Geophys. Res.* **102**(D9), 10727–10738.

Grover S. N. and Beard K. V. (1975) A numerical determination of the efficiency with which electrically charged cloud drops and small raindrops collide with electrically charged spherical particles of various densities. *J. Atmos. Sci.* **32**, 2156–2165.

Grover S. N. and Pruppacher H. R. (1985) The effect of vertical turbulent fluctuations in the atmosphere on the collection of aerosol particles by cloud drops. *J. Atmos. Sci.* **42**, 2305–2318.

Guerzoni S. and Chester R. (1996) The Impact of Desert Dust Across the Mediterranean. Kluwer, Dordretch, The Netherlands, 389 pp.

Harrison R. G. (2004) The global atmospheric electrical circuit and climate. *Surv. Geophys.* **25**, 441–484.

Hunter R. J. (2000) Double layer interaction and particle coagulation. In *Foundations of Colloid Science*. Oxford University Press, Oxford, pp. 581–637.

IARA-CSIC, (1989) Mapa de suelos de Andalucía, E. 1:400.000, 96 pp.

INM (Instituto Nacional de Meteorología). Available from: <http://www.inm.es>. Valores climatológicos normales, Granada (Aeropuerto).

Jaenicke R. (2005) Abundance of cellular material and proteins in the atmosphere. *Science* **308**, 73.

Jickells T. D., An Z. S., Andersen K. K., Baker A. R., Bergametti G., Brooks N., Cao J. J., Boyd P. W., Duce R. A., Hunter K. A., Kawahata H., Kubilay N., laRoche J., Liss P. S., Mahowald N., Prospero J. M., Ridgwell A. J. and Torres R. (2005) Global iron connections between desert dust, ocean biogeochemistry and climate. *Science* **308**, 67–71.

Keller L. P., Thomas K. L. and McKay D. S. (1992) An interplanetary dust particle with links to CI chondrites. *Geochim. Cosmochim. Acta* **56**, 1409–1412.

Kishcha P., Alpert P., Barkan J., Kirrchner I. and Machenhauer B. (2003) Atmospheric response to Saharan dust deduced from ECMWF reanalysis increments. *Tellus* **55B**(4), 901–913.

Lafon S., Rajot J. L., Alfaro S. C. and Gaudichet A. (2004) Quantification of iron oxides in desert aerosol. *Atmos. Environ.* **38**, 1211–1218.

Le Clair B. P., Hamielec A. E. and Pruppacher H. R. (1970) A numerical study of the drag on a sphere at low and intermediate Reynolds number. *J. Atmos. Sci.* **27**, 308–315.

Le Clair B. P., Hamielec A. E., Pruppacher H. R. and Hall W. D. (1972) A theoretical and experimental study of the internal circulation in water drops falling at terminal velocity in air. *J. Atmos. Sci.* **29**, 728–740.

Lin C. L. and Lee S. C. (1973) Transient state analysis of separated flow around a sphere. *Comput. Fluids* **1**, 235–250.

Loÿe-Pilot M. D., Martin J. M. and Morelli J. (1986) Influence of Sahara dust on the rain acidity and atmospheric input to the Mediterranean. *Nature* **321**, 427–428.

Mahowald N., Kohfeld K., Hanson M., Balkansky Y., Harrison S. P., Prentice I. C., Schulz M. and Rodhe H. (1999) Dust sources and deposition during the last glacial maximum and current climate: a comparison of model results with paleodata from ice cores and marine sediments. *J. Geophys. Res.* **104**, 15895–15916.

Mainguet M. (1992) Système expert pour l'évaluation de la dynamique éolienne et la protection contre les effects traumatisants du vent. *Rev. Geomorphol. Dyn.* **41**, 113–136.

Martin J. D. (2004) XPowder. Quantitative and Qualitative Powder X-ray Diffraction Analysis, version 2004.04. Orion Network Communication: Granada. Available from: <http://www.XPowder.com>.

Meunier A. (2005) Clays. Springer, Berlin, 472 pp.

Moulin C., Lambert C. E., Dulac F. and Dayan U. (1997) Control of atmospheric export of dust from North Africa by the North Atlantic Oscillation. *Nature* **387**, 691–694.

Moulin C., Lambert C. E., Dayan U., Masson V., Ramonet M., Bousquet P., Legrand M., Balkanski Y., Guelle W., Marticorena B., Bergametti G. and Dulac F. (1998) Satellite climatology of African dust transport in Mediterranean atmosphere. *J. Geophys. Res.* **103**, 13137–13144.

Munsell Color Company (1995) *Munsell Soil Color Charts*, Baltimore, MD.

Offer Z. Y. and Goossens D. (1994) The use of topographic scale models in predicting eolian dust erosion in hilly areas: field verification of a wind tunnel experiment. *Catena* **22**, 249–263.

Paquet H., Coudé-Gaussen G. and Rognon P. (1984) Étude minéralogique des poussières sahariennes le long d'un itinéraire entre 19° and 35° de latitude Nord, Rev. *Geol. Dyn. Geogr. Phys.* **25**, 257–265.

Parkin D. W., Sullivan R. A. L. and Andrews J. N. (1977) Cosmic spherules as rounded bodies in space. *Nature* **266**, 515–517.

Pinsky M., Khain A. and Shapiro M. (2001) Collision efficiency of drops in a wide range of Reynolds numbers: effect of pressure on spectrum evolution. *J. Atmos. Sci.* **58**, 742–764.

Pokras E. M. (1991) Source areas and transport mechanisms for freshwater and brackish water diatoms deposited in pelagic sediments of the Equatorial Atlantic. *Quat. Res.* **35**, 144–156.

Prospero J. M. (1999) Long-range transport of mineral the dust in the global atmosphere: impact of African dust on the environment of the southeastern United States. *Proc. Natl. Acad. Sci. USA* **96**, 3396–3403.

Prospero J. M., Ginoux P., Torres O., Nicholson S. E. and Gill T. E. (2002) Environmental characterization of global sources of atmospheric soil dust identified with the Nimbus 7 total ozone mapping spectrometer (TOMS) absorbing aerosol product. *Rev. Geophys.* **40**, 1002. doi:10.1029/2000RG000095.

Pruppacher H. R. and Beard K. V. (1970) A wind tunnel investigation of the internal circulation and shape of water drops falling at terminal velocity in air. *Quart. J. Roy. Meteor. Soc.* **96**, 247–256.

Pruppacher H. R. and Klett J. D. (1997) Microphysics of clouds and precipitation. *second ed.* Kluwer Academic Publishers, Dordrecht, p. 954.

Pye K. (1992) Aeolian dust transport and deposition over Crete and adjacent parts of the Mediterranean sea. *Earth Surf. Proc. Land.* **17**, 271–288.

Quereda J., Olcina J. and Montón E. (1996) Red dust rain within the spanish mediterranean area. *Climatic Change* **32**, 215–228.

Rabenhorst M. C., Wilding L. P. and Girdner C. L. (1984) Airborn dusts in the Edwards Plateau region of Texas. *Soil Sci. Soc. Am. J.* **48**, 621–627.

Raes F., Van Dingenen R., Vignati E., Wilson J., Putaud J. P., Seinfeld J. H. and Adams P. (2000) Formation and cycling of aerosols in the global troposphere. *Atmos. Environ.* **34**, 4215–4230.

Ramanathan V., Crutzen P. J., Kiel J. T. and Rosenfeld D. (2001) Aerosol, climate and the hydrological cycle. *Science* **294**, 2119–2124.

Rodríguez S., Querol X., Alastuey A., Kallos G. and Kakaliagou O. (2001) Saharan dust contributions to PM10 and TSP levels in Southern and Eastern Spain. *Atmos. Environ.* **35**, 2433–2447.

Romero O. E., Dupont L., Wyputta U., Jahns S. and Wefer G. (2003) Temporal variability of fluxes of eolian-transported freshwater diatoms, phytoliths, and pollen grains off Cape Blanc as reflection of land–atmosphere–ocean interactions in northwest Africa. *J. Geophys. Res.* **108**(C5), 3153, doi: 101029/2000JC00375.

Rosenfeld D. (2000) Suppression of rain and snow by urban and industrial air Pollution. *Science* **128**, 1793–1796.

Rosenfeld D., Rudich Y. and Lahav R. (2001) Desert dust suppressing precipitation, a possible desertification feedback loop. *Proc. Natl. Acad. Sci. USA* **98**, 5975–5980.

Seinfeld J. H. and Pandis S. M. (2006) *Atmospheric Chemistry and Physics From Air Pollution to Climate Change*. Wiley-Interscience, New York, p. 1326.

Simonson R. W. (1995) Airborne dust and its significance to soils. *Geoderma* **65**, 1–43.

Staudt M. (2004) Detección de cambios térmicos en la Península Ibérica con datos homogéneos regionales. Ph.D. Thesis, Granada University, Spain, p. 559.

Stoorvogel J. J., Breemen N. V. and Hansen B. H. (1997) The nutrient input by Harmattan dust to a forest ecosystem in Côte d'Ivoire, Africa. *Biogeochemistry* **37**, 145–157.

Swap R., Garstang M., Macko S., Tyson P., Maenhaut W., Artaxo P., Kallberg P. and Talbot R. (1996) The long range transport of southern African aerosols to the tropical South Atlantic. *J. Geophys. Res.* **101**, 23777–23791.

Thornton D. C., Bandy A. R., Blomquist B. W., Bradshaw J. D. and Blake D. R. (1997) Vertical transport of sulphur dioxide and dimethyl sulphide in deep convection and its role in new particle formation. *J. Geophys. Res.* **102**, 28501–28509.

Toon O. B. (2003) African dust in Florida clouds. *Nature* **424**, 623–624.

Tsoar H. and Pye K. (1987) Dust transport and the question of desert loess formation. *Sedimentology* **34**, 139–153.

Usher C. R., Michel A. E. and Grassian V. H. (2003) Reactions on mineral dust. *Chem. Rev.* **103**, 4883–4939.

Wang C., Crutzen P. J., Ramanathan V. and Williams S. F. (1995) The role of a deep convective storm over the tropical Pacific Ocean in the redistribution of atmospheric chemical species. *J. Geophys. Res.* **100**, 11509–11516.

Washington R., Todd M. C., Engelstaedter S., M'bainayel S. and Mitchell F. (2006) Dust and the Low Level Circulation over the Bodelé Depression, Chad: observations from BoDEx 2005. *J. Geophys. Res.* **111**, D03201. doi:10.1029/2005JD006502.

Weaver C. E. and Pollard L. D. (1973) *The chemistry of clay minerals*. Elsevier, Amsterdam p. 213.

Wurzler S., Reisin T. G. and Levin Z. (2000) Modification of mineral dust particles by cloud processing and subsequent effects on drop size distributions. *J. Geophys. Res.* **105**, 4501–4512.

Yaalon D. H. (1997) Soils in the Mediterranean region: what makes them different ? *Catena* **28**, 157–169.

Associate editor: David J. Vaughan

Atmospheric Environment 120 (2015) 160–172

Contents lists available at ScienceDirect

Atmospheric Environment

journal homepage: www.elsevier.com/locate/atmosenv
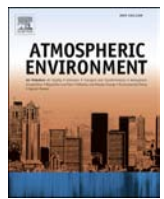
Role of clay minerals in the formation of atmospheric aggregates of Saharan dust

Javier Cuadros [a, *], José L. Diaz-Hernandez [b], Antonio Sanchez-Navas [c], Antonio Garcia-Casco [c]

[a] Department of Earth Sciences, Natural History Museum, Cromwell Road, London SW7 5BD, United Kingdom
[b] IFAPA, Área de Recursos Naturales, Consejería de Agricultura, Pesca y Medio Ambiente, Junta de Andalucía, 18080 Granada, Spain
[c] Departamento de Mineralogía y Petrología-IACT, Universidad de Granada-CISC, 18071 Granada, Spain

HIGHLIGHTS

- Iberulites are >100 μm aggregates of Saharan dust described in SE Spain.
- Iberulites contain quartz, feldspar, carbonate, clay, sulphates and Fe oxyhydroxides.
- Clay appears to be enriched in the iberulites with respect to the aerosol.
- Clay morphology and hygroscopicity are important in shaping the iberulites.
- Variable gypsum in iberulites linked to anthropogenic SO_2 emissions.

ARTICLE INFO

Article history:
Received 13 May 2015
Received in revised form
29 July 2015
Accepted 26 August 2015
Available online 29 August 2015

Keywords:
Clay
Iberulite
Mineral aerosol

ABSTRACT

Saharan dust can travel long distances in different directions across the Atlantic and Europe, sometimes in episodes of high dust concentration. In recent years it has been discovered that Saharan dust aerosols can aggregate into large, approximately spherical particles of up to 100 μm generated within raindrops that then evaporate, so that the aggregate deposition takes place most times in dry conditions. These aerosol aggregates are an interesting phenomenon resulting from the interaction of mineral aerosols and atmospheric conditions. They have been termed "iberulites" due to their discovery and description from aerosol deposits in the Iberian Peninsula. Here, these aggregates are further investigated, in particular the role of the clay minerals in the aggregation process of aerosol particles. Iberulites, and common aerosol particles for reference, were studied from the following periods or single dust events and locations: June 1998 in Tenerife, Canary Islands; June 2001 to August 2002, Granada, Spain; 13–20 August 2012, Granada; and 1–6 June 2014, Granada. Their mineralogy, chemistry and texture were analysed using X-ray diffraction, electron microprobe analysis, SEM and TEM. The mineral composition and structure of the iberulites consists of quartz, carbonate and feldspar grains surrounded by a matrix of clay minerals (illite, smectite and kaolinite) that also surrounds the entire aggregate. Minor phases, also distributed homogenously within the iberulites, are sulfates and Fe oxides. Clays are apparently more abundant in the iberulites than in the total aerosol deposit, suggesting that iberulite formation concentrates clays. Details of the structure and composition of iberulites differ from descriptions of previous samples, which indicates dependence on dust sources and atmospheric conditions, possibly including anthropic activity. Iberulites are formed by coalescence of aerosol mineral particles captured by precursor water droplets. The concentration of clays in the iberulites is suggested to be the result of higher efficiency for clay capture than for the capture of larger mineral grains. The high hygroscopicity of clay minerals probably causes retention of water in the evaporation stage and some secondary minerals (mainly gypsum) are associated with clays.

* Corresponding author.
E-mail addresses: j.cuadros@nhm.ac.uk (J. Cuadros), josel.diaz@juntadeandalucia.es (J.L. Diaz-Hernandez), asnavas@ugr.es (A. Sanchez-Navas), agcasco@ugr.es (A. Garcia-Casco).

http://dx.doi.org/10.1016/j.atmosenv.2015.08.077

1. Introduction

Mineral aerosols originating from soils and surface sediments are complex mixtures of particles lofted into the atmosphere by

eolian processes affecting mainly arid and semi-arid lands. The Sahara produces an enormous quantity of aeolian dust that influences climate and soil composition in vast and distant areas. Saharan dust is transported at great distances along relatively well-known trajectories connecting North Africa with Europe and the Americas (Swap et al., 1992; Franzen et al., 1994; Shinn et al., 2000). The North Atlantic Oscillation controls the evolution of Saharan air masses loaded with dust or plumes and therefore the dust transport over the Atlantic Ocean and the Western Mediterranean Sea (Moulin et al., 1997; Rodwell et al., 1999; Bout-Roumazeilles et al., 2007). Large dust outbreaks during the summer reach the South of the Iberian Peninsula, where the duration of individual Saharan plume events is estimated to vary between 2 and 3 days (Rodríguez et al., 2001).

The particles from the dust of the Saharan plumes are mainly composed of silicates, a characteristic that they share with those from dust storms in the Gobi and Arizona deserts (Goudie and Middleton, 2001). The average chemical composition of the dust from these sources is similar to that from all world dust storms and to the mean composition of the Earth's surface rocks (Goudie and Middleton, 2001; Lawrence and Neff, 2009). Mineral aerosols consist of particles with typical size of less than 20 μm, which can undergo long-range transport (Seinfeld and Pandis, 2006). Particularly, atmospheric aerosols with particle size <2 μm may reside one week in the atmosphere (Tegen and Lacis, 1996; Miller et al., 2006; Kok, 2011). These long residence times in the atmosphere cause interaction with atmospheric components (water, gases, other aerosols). Given their small particle size, clays are abundant components in atmospheric dust, especially in longed-lived aerosols (Engelbrecht and Derbyshire, 2010). All clays have large surface areas of predominantly hydrophilic character. Besides, smectite and vermiculite have swelling layers that admit large proportions of water between them. As a result, the clay component of dust interacts strongly with atmospheric water, which is retained by the clay in variable amounts.

In some studies, dust has been found to consist of large aggregates (Díaz-Hernández and Párraga, 2008; Jeong et al., 2014). The aggregates investigated by Díaz-Hernández and Párraga (2008) were from the Sahara, often reaching sizes > 100 μm, and were interpreted to form by a complex process of aerosol inclusion into water droplets, from which they inherited their external morphology. They were termed "iberulites" because they are a very rare phenomenon first described by Díaz-Hernández and Párraga (2008) and found in the Iberian Peninsula. They are a new type of aerosol particle forming in the atmosphere, during Saharan dust plume events under very specific atmospheric conditions. The aggregates found by Jeong et al. (2014) were from Asia, different in shape, no larger than 60 μm, and interpreted as generated in the source area.

In this paper we study iberulites and common aerosols from the Sahara, with special emphasis on clay minerals and their role in the formation of iberulites and in the physico-chemical processes taking place within them. The clay mineralogy of Saharan dust has been addressed in numerous occasions and shown to depend on sources, trajectory and sampling location (Goudie and Middleton, 2001; Bout-Roumazeilles et al., 2007, and references therein). Recently, chemical and mineralogical investigation of clay minerals from iberulites (Díaz-Hernández and Párraga, 2008) and common aerosols from similar dust sources (Díaz-Hernández et al., 2011) show the presence of smectite, illite, kaolinite and chlorite. Our mineralogical, textural and compositional data indicate that, due to their particle size, hygroscopicity and physical flexibility, clay minerals are essential for the formation of these large mineral aggregates within water droplets in the atmosphere. They appear to be concentrated in the iberulites with respect to the other mineral

phases in the aerosol. Clays influence the fabric and porosity of the aggregates. In addition, they influence the drying process of the aggregate and thus salt precipitation within it.

The clay minerals mentioned above have the following characteristics that are used for their mineralogical and chemical identification. Smectite has two tetrahedral sheets and one octahedral sheet in each layer (TOT layer). A small negative layer charge is compensated by hydrated cations in the interlayer space. Smectite is unequivocally recognized by the expansion of the distance between layers to ~17 Å when treated with ethylene glycol. Illite has also TOT layers with high negative charge and interlayer K compensating for it. Interstratified illite-smectite is a group of minerals in which layers of one and the other mineral stack together within crystals. Kaolinite has TO layers with no charge and no interlayer cations. Chlorite has TOT layers intercalated with hydroxyl layers (total layer unit TOTH). Contrary to smectite, illite, kaolinite and chlorite do not change their interlayer space with ethylene glycol treatment.

2. Material and methods

The four studied samples were selected from a collection of atmospheric dust obtained by dry passive collectors from 1998 to 2014 (Table 1). It must be emphasized that all correspond to atmospheric dry deposition. Sample TF6-98 consists of common aerosol particles with no large aggregates, collected during June of 1998 at the south western slope of the Teide mountain, in the Tenerife island, Canary archipelago, off the northwest coast of north Africa. The other samples contain a range of iberulite proportions (Table 1). All of them were collected in the Granada basin, an intra-mountain depression in the Betic Cordilleras, southern Spain. Sample GR6-14 corresponds to an iberulite-rich deposition (Fig. 1). Sample GR8-12 consists only of iberulites (2.5 mg total weight) separated from the total aerosol. In all cases, medium-sized trays (0.064 m² of surface area and 5 cm deep) were used to obtain quantities suitable for analysis. They were placed in rural areas, on the roof of buildings ~8 m above the ground, and on structures ~2 m above the roof (total height ~10 m). In Granada, the dust collectors were further protected from local dust contribution by surrounding irrigated land and by a dense tree barrier (Díaz-Hernández and Miranda, 1997).

Samples were carefully examined under a stereomicroscope and classified according to presence and abundance of aggregates. In the case of sample GR8-12 the iberulite aggregates were hand-picked under the stereomicroscope. The isolated iberulites were studied using SEM and EPMA. High-resolution secondary electron (SE) images and microanalysis of carbon-coated samples of iberulites from sample GR8-12 were obtained with a field-emission SEM Auriga (Carl Zeiss) equipped with a LinK INCA 200 (Oxford Instruments) analytical system. During sample preparation, carbon coating was carefully performed to avoid or minimize the generation of artifacts at nanometer scale. The interior of the iberulites was also investigated by embedding them in resin, their preparation as polished sections and carbon coating. Back-scattered electron (BSE) images and energy-dispersion X-ray (EDX) spot analyses (200 nm of diameter) were performed on the polished sections with the same instrument.

X-ray chemical-element maps were obtained for iberulites in polished sections from samples GR6-14 and GR8-12, with an EPMA apparatus CAMECA SX100 operated at 15 kV of acceleration voltage and 5 nA of probe current. Spot size was 1 μm. X-ray images were obtained by moving the polished section while maintaining the beam in a fixed position. The step-to-step displacement and acquisition time were 1 μm and 500 ms respectively. Element maps were processed with the software DWImager (Torres-Roldán

Table 1
Location and time of collection of the studied samples, as well as proportion of iberulites in the aerosol.

Sample	Location	Coordinates	Altitude (m ASL)	Time of collection	Iberulite proportion
TF6-98	Teide mountain, Tenerife	28°5.983′N 16°40.837′W	628	June 1998[a]	No iberulites
GR01-02	Granada basin, Spain	37°10′N 3°31′W	640	June 2001—August 2002	Low
GR8-12	Granada basin, Spain	37°10′N 3°31′W	640	13—20 August 2012[a]	Only iberulites[b]
GR6-14	Granada basin, Spain	37°10′N 3°31′W	640	1—6 June 2014[a]	~30% wt.

[a] Single dust event.
[b] Separated from the overall aerosol. The original aerosol had an iberulite proportion of ~20% wt.
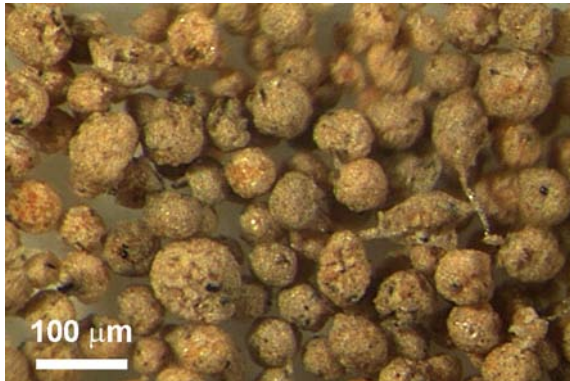
Fig. 1. Pinkish, round aggregates of aerosol particles (iberulites) from sample GR6-14 as seen under the stereoscopic microscope. (For interpretation of the references to colour in this figure legend, the reader is referred to the web version of this article.)

and García-Casco, unpublished) to obtain images where minerals are identified. Colour mineral-phase maps overlie a grey-scale base-layer that represents the texture of the analysed surface. This gray-scale layer is calculated with the formula $shade\ of\ grey = \Sigma\ (counts_i \cdot A_i)$, (where A is atomic number and i is Si, Ti, Al, Fe, Mg, Ca, Na, and K).

Further analyses were performed using aerosols with no iberulites (sample TF6-98), aerosols containing diverse amounts of iberulites (GR01-02 and GR6-14) and the sample containing exclusively iberulites (GR8-12). They were milled with an agate mortar and pestle for one minute for powder X-ray diffraction (XRD) analysis. Only samples TF6-98, GR01-02 and GR6-14 were sufficiently large to carry out powder analysis. Their powders were deposited on a zero-background holder and the XRD diagrams recorded at the University of Granada using a PANalytical X'Pert Pro diffractometer (Cu-Kα radiation, 45 kV, 40 mA) equipped with an X'Celerator solid-state linear detector. This detector covers an angle of 2.1° and integrates the diffracted intensity over this angle dynamically as it scans. The diffraction patterns were obtained by a continuous scan between 3 and 50°2θ, with a 0.01°2θ resolution, and 15 min total scan time (equivalent to 20 s counting time per 0.01°2θ). Sample GR8-12 (2.5 mg) was prepared as an oriented mount, which enhances the intensity of basal diffraction peaks of clays. The powder was suspended in water, deposited on a zero-background sample holder and analysed first as air-dried and later as a glycolated oriented mount (60 °C overnight in an ethylene-glycol atmosphere). In this sample the resulting oriented mount was an extremely thin film. The mount was analysed in the Natural History Museum (London) with a PANalytical X'Pert Pro diffractometer with the following experimental conditions: continuous scan between 3 and 50°2θ, resolution of 0.0167°2θ, and scanned for 25 h (equivalent to 67 min per 0.0167°2θ).

For samples TF6-98, GR01-02 and GR6-14, the fraction < ~2 μm was extracted from the whole powders by suspending them in distilled water, decanting the suspension for 8 h and pipetting the upper 10 cm of the suspension. The clay was concentrated from the supernatant by centrifugation, oven-dried and ground. Suspensions of the ground clay were deposited onto circular glass slides to generate oriented mounts. They were analysed as air-dry samples only, at the University of Granada, using the conditions indicated above for the powder samples. All XRD data were processed using the XPOWDER program (Martín-Ramos et al., 2012) for visualization of the XRD patterns and mineral identification.

The <2 μm size fraction from sample TF6-98 (that did not contain iberulites) and a few iberulites from sample GR8-12 were studied by TEM. The powders or a few iberulite aggregates were embedded in an epoxy resin and sectioned with a diamond ultra-microtome (<100 nm thick slides) that were deposited on a copper grid and coated with carbon. TEM and STEM (HAADF: high-angle annular dark field) images, selected area electron diffraction (SAED) patterns, single spot microanalyses and X-ray chemical-element maps were obtained with a FEI TITAN G2 TEM apparatus operated at 300 kV and equipped with four energy dispersive X-ray (EDX) detectors (SuperX system). Fully quantitative analyses (analytical electron microscopy, AEM) of clays were also obtained with this instrument in STEM mode using a beam of 5 nm in diameter and a scanning area of 20 × 100 nm. These EDX analyses were corrected by the thin-film method of Lorimer and Cliff (1976). The k-factors were determined using muscovite, albite, biotite, spessartine, olivine, and titanite standards.

3. Results

3.1. XRD mineralogical analysis

The bulk mineralogy of the powders from samples TF6-98, GR01-02 and GR6-14 is shown in Fig. 2A. In the samples from Granada (GR01-02 and GR6-14), the most prominent phases are quartz, dolomite and calcite. Feldspars are prominent in sample TF6-98. Halite is only observed in the sample from Tenerife. Gypsum occurs in low amounts in all samples. Illite is present in the three samples, in the order GR01-02 > GR6-14 > TF6-98. Kaolinite is clearly observable in the three samples. A smectite-like phase is present in GR01-02 as a small, narrow peak, and possibly also as a wide peak in the same area. Sample GR6-14 may also present a wide smectite peak.

The XRD patterns of the oriented mounts of the fraction <2 μm (Fig. 2B) are similar but the proportion of clay minerals is enhanced. Smectite becomes more obvious in sample GR01-02 (small, sharp peak at 14.5 Å), but cannot be positively identified in the other two samples (the hump in the background at low angle, caused by X-ray cut-off, interferes with a positive detection). Gypsum and quartz are also present in this fine fraction of the three samples. Feldspar, halite and polyhalite are present in TF6-98, and dolomite in GR01-02.

Sample GR8-12, consisting exclusively of iberulites and with no particle size separation, was prepared as an oriented mount. The XRD patterns in air-dry state and after glycolation (to identify smectite) are shown in Fig. 3. There is a prominent peak at ~13 Å
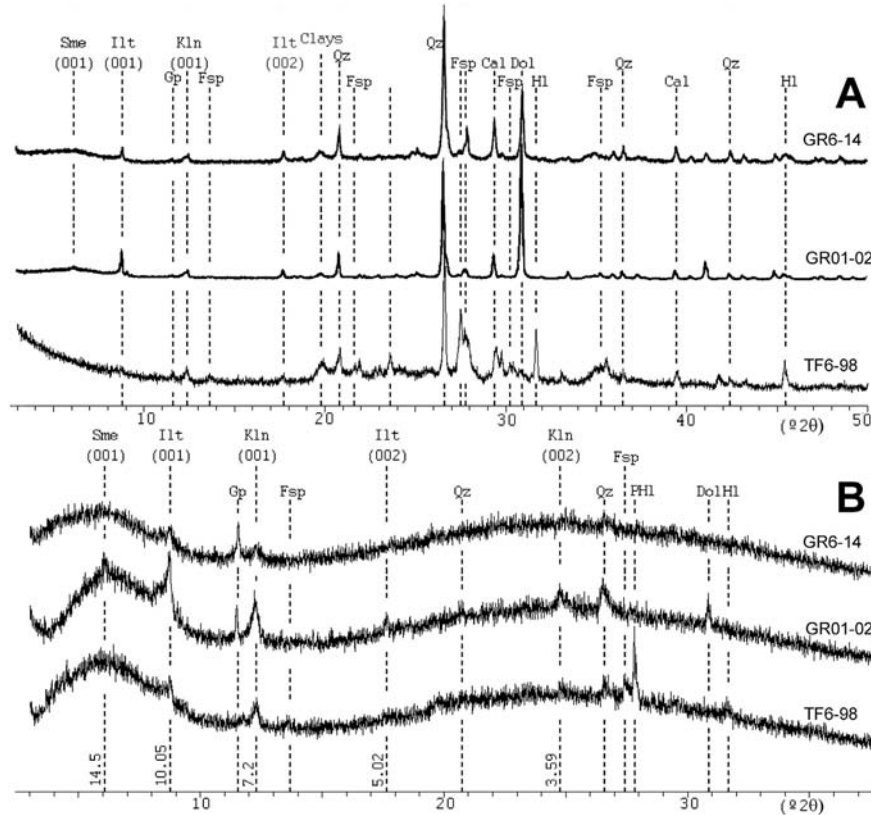
Fig. 2. Mineralogical composition of aerosol samples from the XRD patterns: A) Powder patterns of the whole samples (common aerosol plus iberulites). B) Oriented aggregates of the <2 μm size fraction. The intensity increase at 3—6°2θ (in B) is partially caused by X-ray cut-off at very low angle. The hump at 15—40°2θ (in B) is caused by the glass slide supporting the oriented mount. The figures on the dash lines are *d*-spacing values in Å. (Mineral abbreviations: Cal = calcite; Dol = dolomite; Fsp = feldspars; Gp = gypsum; Hl = halite; Ilt = illite; Kln = kaolinite; PHl = polyhalite; Qz = quartz; Sme = smectite).

that corresponds to a smectite-like phase. Contrary to what should be expected, there is no displacement of this peak after glycolation to ~17 Å. However, there are other changes that indicate that this peak does correspond to a smectite-like phase: 1) the peak sharpens and becomes more intense; 2) a wide band between 7.5 and 9°2θ in the air-dry sample disappears in the glycolated sample (arrow in Fig. 3). These changes indicate that the wide band is a smectite-like phase and that glycolation shifts the *d*-spacing of these layers to 13.33 Å. The lack of expansion to

~17 Å is most likely due to the fact that the corresponding mineral phase is vermiculite or smectite with a high layer charge, which causes only partial expansion with ethylene glycol to ~13 Å (MacEwan and Wilson, 1984). The 001 peaks of illite and kaolinite are also observed, together with the two most prominent quartz peaks.

3.2. SEM study of iberulite aerosols

Observation of the surface of iberulites with secondary electrons (Fig. 4A), showed spherical to near spherical objects several tens of μm wide, with a rough surface on which μm-sized particles were present. EDX microanalysis of the surface shows S and Ca (likely indicating the occurrence of gypsum) together with the usual chemical elements corresponding to clays (Fig. 4B). In a more detailed observation, the surface of the iberulites appeared coated by clay platelets arranged with their basal surfaces tangential to the surface of the iberulite (Fig. 4C). Higher magnification images of the coating clays showed a very rough surface texture, and the occurrence of aggregates of nanoparticles adhered to the clays (Fig. 4D). Most possibly, the nanoparticles are the calcium sulfate detected by EDX.

BSE images from polished sections of the iberulites (Fig. 5) shows that in their interior there are grains of quartz several μm in diameter (no spectra shown), feldspar grains (spectrum 4; the morphology and chemistry of this grain is interpreted as feldspar, with the EDX analysis including also surrounding or coating kaolinite and a sulfate phase), very fine-grained aggregates of clay platelets more abundant towards the surface of the iberulites
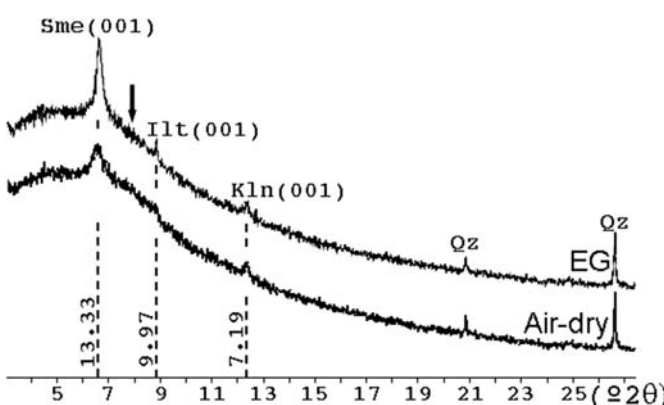
Fig. 3. XRD patterns of air-dried and glycolated (EG) oriented mounts for clay mineral identification in sample GR8-12, containing only iberulites. The figures on the dot lines are *d*-spacing values in Å. The arrow indicates a wide peak in the air-dry specimen that disappears in the EG specimen (see text).
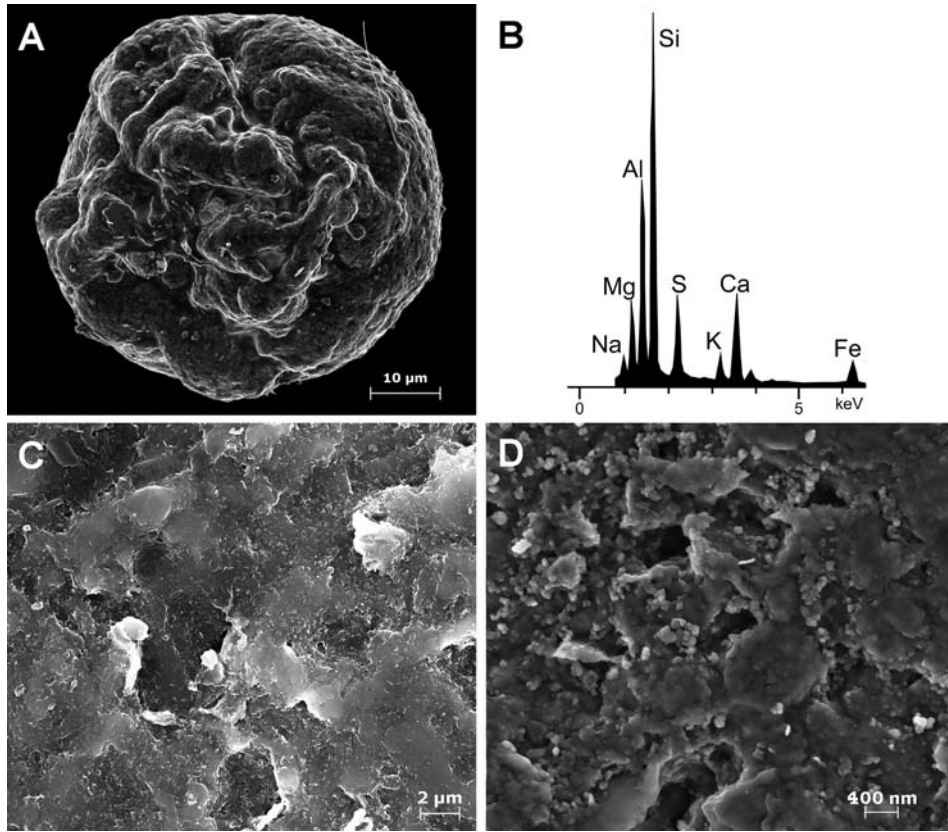
Fig. 4. SEM secondary electron images and EDX microanalysis of iberulites from sample GR8-12. A) Low magnification image of an iberulite showing an irregular surface formed by the assemblage of mineral particles. B) EDX spectrum representative of the average composition of the iberulite surface in A, interpreted as clay and gypsum. C) Closer view of the surface of an iberulite, which appears covered by platy clay particles. D) Close-up image of the surface showing the presence of aggregates of round mineral particles of nanometre size, interpreted to be gypsum, on the clay particles.

(Fig. 5B and D, spectrum 1), Fe oxides (not shown) and coarser mica flakes. Mica particles have variable composition, from phengite (spectrum 2) to muscovite (spectrum 3). Clay packets usually have sizes <1 μm in length and 100 nm in thickness (Fig. 5B and D). EDX microanalyses indicate that clays are illite or smectite (spectrum 1) and kaolinite (spectrum 5; this analysis collected X-rays from several mineral grains, but the prominence of the Si and Al peaks, and the relative Si/Al intensities indicate kaolinite). Medium to low intensity S and Ca peaks appear frequently in the spectra (spectra 1, 4 and 5), probably corresponding to gypsum. Other detected mineral phases include monazite (spectrum 5) and Ti oxides (not shown).

3.3. Mineral distribution and chemistry of iberulite aerosols by EPMA

A detailed compositional and mineralogical study of the iberulite aggregates was performed by EPMA for GR8-12 and GR6-14 samples. Mineral identification was based on chemistry and supported by morphology. The ideal structural formulas of the phyllosilicates found in the iberulites are provided here to clarify the basis of the identifications. The octahedral cations are in parenthesis. Smectite interlayer cations are in square brackets. Muscovite $Si_3Al_1(Al_2)$ $K_1O_{10}(OH)_2$; phengite $Si_3Al_1(AlMgFe)_2K_1O_{10}(OH)_2$; illite $Si_{3.3}Al_{0.7}(AlMgFe)_2K_{0.8}O_{10}(OH)_2$; smectite $Si_{3.8}Al_{0.2}(AlMgFe)_2[CaMgNa]_{0.2}O_{10}(OH)_2$; kaolinite $Si_2Al_2O_5(OH)_4$; Fig. 6 shows texture images (where the gray shade is a function of the average atomic number, Z, with lighter shades corresponding to higher Z) and Fe, Ti and S X-ray maps of four

iberulites. Iron is widely distributed in the mineral aggregate whereas Ti is highly concentrated in small particles. The most intense signal of Fe and Ti Kα X-rays of Fig. 6B and C corresponds to particles of Fe- and Ti-oxides and mica (elongated particles). The less intense Fe signal in Fig. 6B is attributed to Fe in smectite and illite. Sulphur is distributed across the aggregates, most likely in gypsum. A few particles, with very intense S Kα signal, apparently consist exclusively of S (e.g., arrow in Fig. 6D).

Mineral phase maps show that the coarser components of the iberulites are quartz, feldspars, carbonates and minor amounts of some other aluminosilicate (Fig. 7A and B). Illite and smectite particles (it is not possible to distinguish them chemically in the images) are distributed within the entire aggregates (yellow in Fig. 7C). Small kaolinite particles and coarser mica particles with laminar habit of several tens of μm in length are less abundant and also distributed across the grains. Interestingly, kaolinite appears as alteration rims in some coarse aluminosilicate grains with composition Al_2SiO_5 (arrow in middle grain, Fig. 7A). Also, some muscovite plates appear completely altered to illite + smectite (arrow in Fig. 7C), and a feldspar grain (arrow in top grain, Fig. 7A) partially altered to sericite (K- and Al-rich illite; appears as muscovite in Fig. 7C). The area of each of the detected mineral phases in these four iberulites is an approximation to their relative abundance in the aggregates. Averaging the four iberulites studied, illite + smectite are the most abundant phases with 48% of the area, followed by calcite (19%), quartz (18%), mica (6%), kaolinite (4%), feldspars (3%), dolomite (1%) and an Al_2SiO_5 mineral phase (1%). The average total clay content is 52%. The illite + smectite area in the four iberulites is fairly constant, 47–49%. The kaolinite content
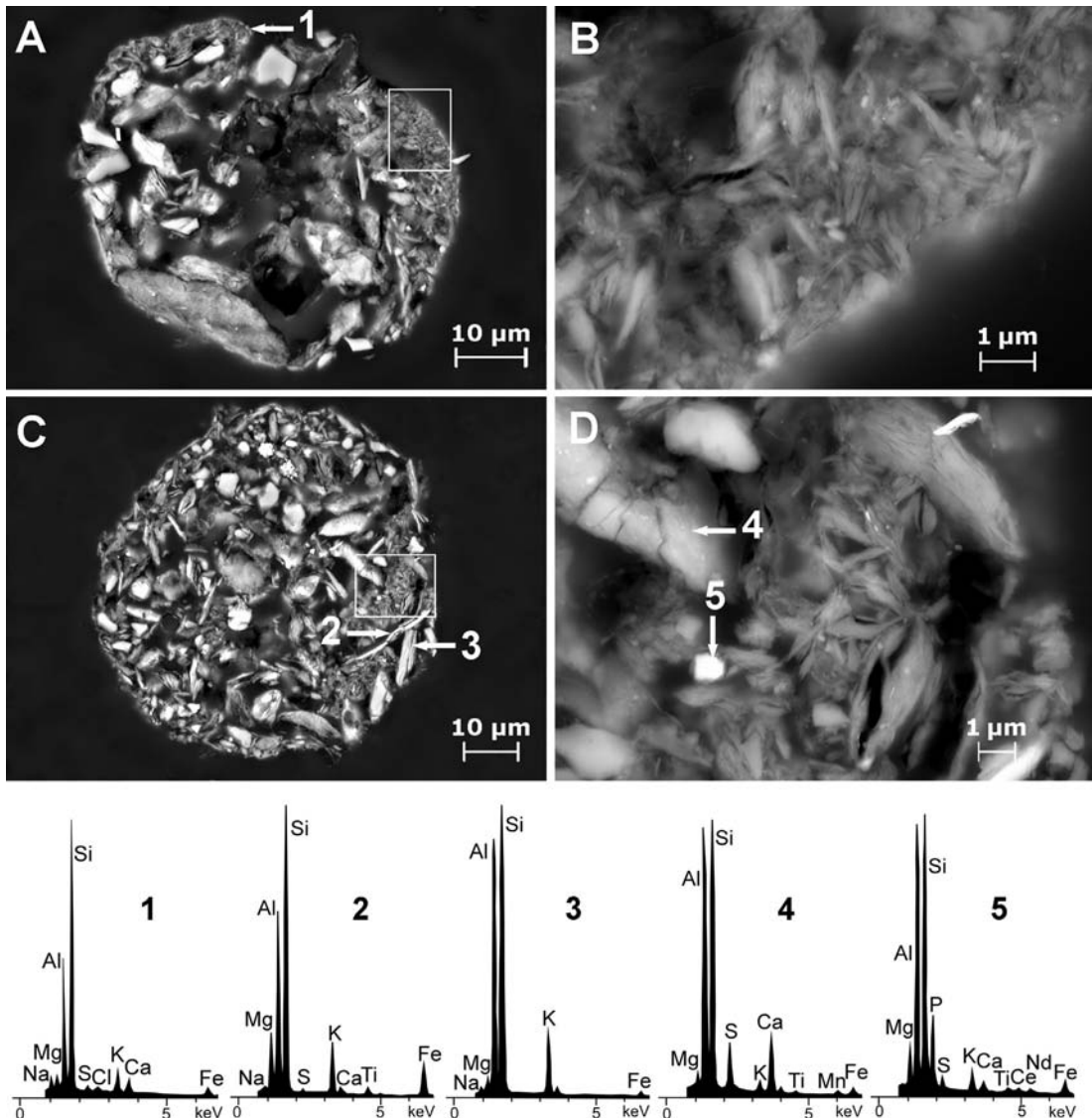
Fig. 5. SEM back-scattered electron images and EDX microanalyses obtained from iberulites in polished sections from sample GR8-12. A) Low magnification image of an iberulite containing mineral particles of several μm with angular shapes (mainly quartz), as well as masses of finer particles (clays) that appear located next to the surface (composition in spectrum 1). The large void in the centre is most likely caused during sample preparation. B) Detail of the region in the box in A, mainly composed by fine-grained minerals of laminar habit (clays). C) Iberulite with a well-preserved core, showing the arrangement of mineral particles with very different size and morphology. Large mica flakes are observed (*e.g.* spectra 2 and 3). D) High magnification image of box in C, showing the arrangement of clay particles in a clay-rich region. Spectrum 4 most probably corresponds to a feldspar grain, although contamination with kaolinite and a sulfate phase is likely. Spectrum 5 includes sulfate(s), an LREE phosphate and clay (probably kaolinite).

varies from 2% in the three iberulites from the 2014 event (three upper aggregates in Fig. 7) and 10% in the iberulite from the event in 2012.

The compositional ranges of the several identified minerals is shown in Fig. 7D–F. The mica composition varies from muscovite (region 1 in Fig. 7D) to phengite (region 2 in Fig. 7D), in agreement with SEM-EDX results (Fig. 5, spectra 2 and 3). A Ti-rich phengite also occurs in the iberulites (Fig. 5F, spectrum 2, and elongated particle in Fig. 6C). The illite plus smectite composition ranges widely. Presumably, illite occupies the region between fields 1 and 2 (Fig. 7E), and smectite has the greater compositional variation reaching the Fe + Mg-rich region 3. The compositional range of kaolinite may reflect the presence of kaolinite-rich interstratified kaolinite-smectite or kaolinite derived from smectite pedogenically, which preserve some Fe and Mg from smectite (Fig. 7F).

3.4. TEM and AEM study of clays from aerosols

Given that the clay mineralogy of all samples is similar (smectite, illite and kaolinite), two samples were selected for the TEM study, the <2 μm size fraction of aerosols with no iberulites (sample TF6-98), and iberulites (sample GR8-12). Low-magnification STEM images and X-ray maps from sample TF6-98 (Fig. 8) show a mixture of nanometre-sized mineral particles as illite (bright elongated particle in Fig. 8F), plagioclase (spectrum 3), Fe oxy-hydroxides (small bright particles in Fig. 8E), montmorillonite (spectrum 1), nontronite (spectrum 2) and either beidellite or albite partially altered to kaolinite (spectrum 4). Most of the material contains Si, Al, Mg and Fe, corresponding to montmorillonite (Fig. 8B–D). Iron enrichment is observed in small and irregular parts of the map (Fig. 8E), corresponding to Fe oxy-hydroxides. There is also Fe accumulation in a clay-like particle corresponding to nontronite
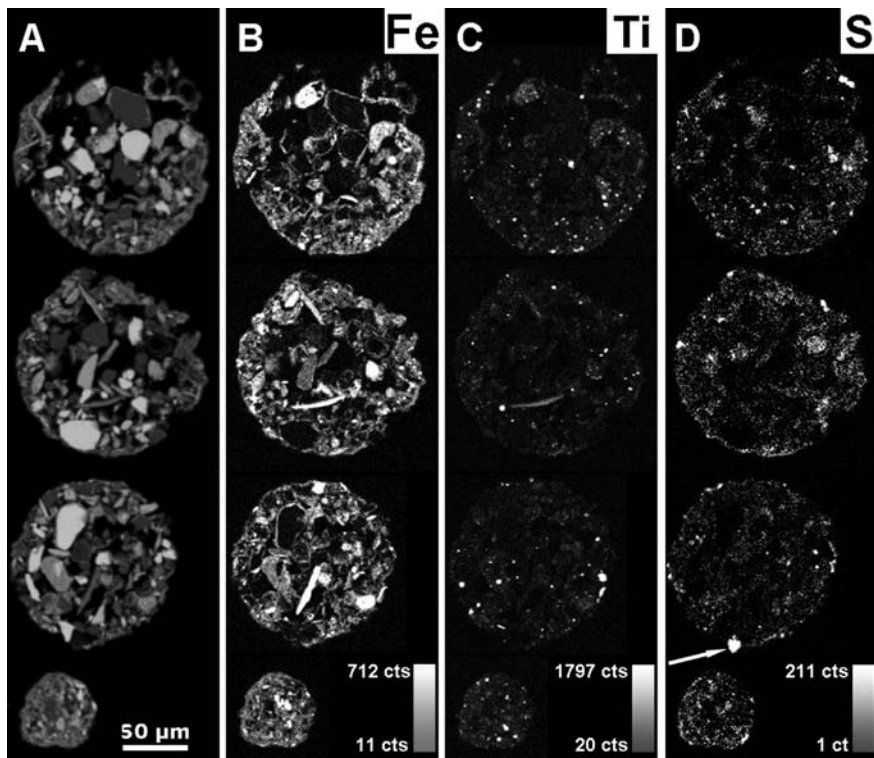
Fig. 6. Chemical maps of iberulite sections from EPMA. The three large iberulites are from sample GR6-14 and the small one from GR8-12. A) Grey-scale base-layer or Z image containing the basic textural information. B) to D) Element X-ray maps of Fe, Ti and S. Lighter shades represent more intense X-ray signals (see count scales). The arrow in D indicates a grain apparently containing only S.

flakes (Fig. 8E). Potassium enrichment is associated with illite plates (Fig. 8F). Very low amounts of gypsum are detected on one of the smectite particles (spectrum 1). There is no positive detection of kaolinite particles in the TEM study carried out on aerosols without iberulites (TF6-98). The reason for this is not clear, since XRD analysis displays a noticeable kaolinite peak (Fig. 2). Perhaps Fe and
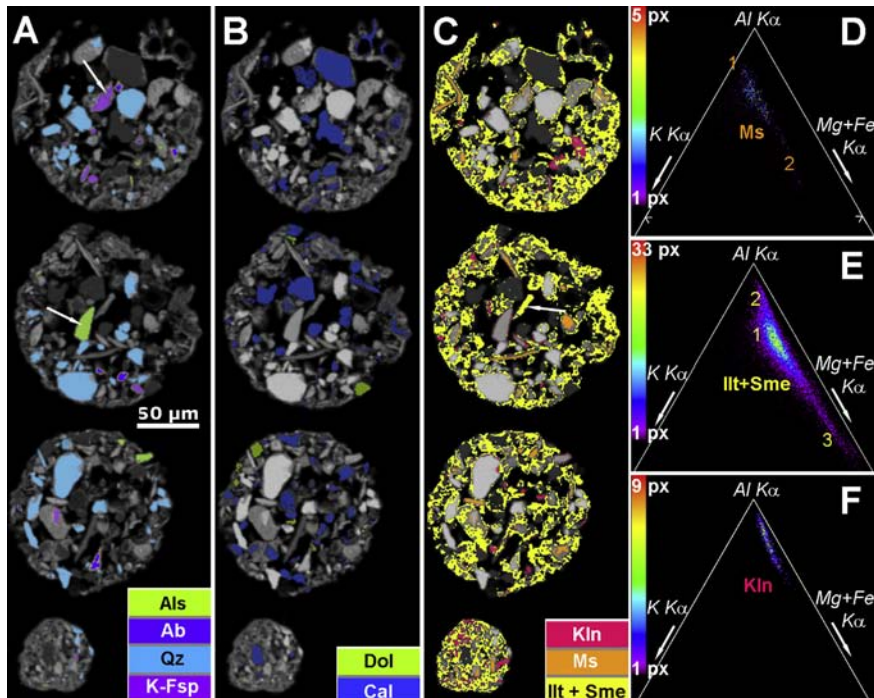
Fig. 7. Chemistry and distribution of mineral grains within the iberulites shown in Fig. 6, from EPMA data. A–C) Mineral phase maps obtained from grain composition. Illite and smectite cannot be resolved and they appear together. Arrows in A point to a K-feldspar and one aluminosilicate (Als) particle with their surface altered to clay minerals (see text for details). There are also grains of albite (Ab) composition. Arrow in C points to a large plate of muscovite completely altered to illite + smectite. D–F) Chemical variations of muscovite, illite + smectite and kaolinite within the K−Al−Fe + Mg field. Colours in D−F indicate the number of pixels with the corresponding composition (following the scale on the left). (For interpretation of the references to colour in this figure legend, the reader is referred to the web version of this article.)
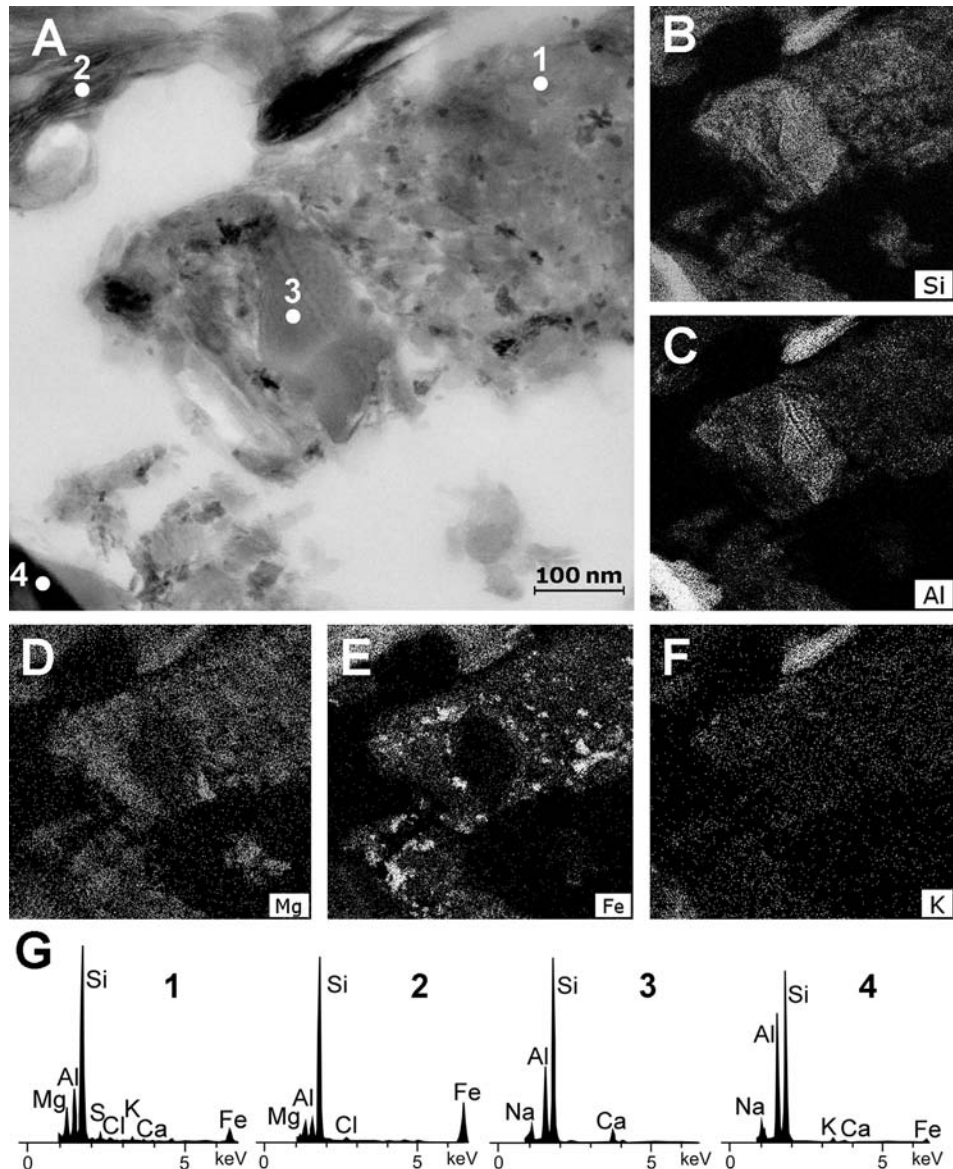
Fig. 8. TEM image and chemical maps of the <2 μm size fraction of sample TF6-98. A) STEM image (type HAADF) with the spots analysed by AEM (spectra in G). B)–F) Si, Al, Mg, Fe and K X-ray maps. The spectra and the chemical distribution of elements indicate the presence of montmorillonite (spectrum 1), nontronite (spectrum 2), illite (bright particle in F), plagioclase (spectrum 3), beidellite or albite partially altered to kaolinite (spectrum 4) and iron oxy-hydroxides (bright areas in E).

Mg substitution or mixed-layering with smectite mask the expected kaolinitic composition.

In the TEM study special attention was given to illite and smectite because they were the most frequently observed phases with this technique. In sample TF6-98, illite occurs as packets 20–100 nm thick (Fig. 9A) that sometimes are partially altered to smectite flakes (Fig. 9B). Smectite appears in curved packets of variable size from 3 to 50 nm thick, with imperfect layer terminations and variable fringe contrast (Fig. 9B–D). Smectite packets sometimes include particles of iron oxy-hydroxides with a marked dark contrast (Fig. 9C). In some few cases, smectite occurred as unoriented aggregates of very small packets including nanometre-sized salt particles containing S and Cl (dark-contrast particles in Fig. 9D and inset). Compositionally, smectites show a broad range from beidellite to Fe + Mg-rich montmorillonite, equivalent to the regions 2 and 3 in Fig. 7E, respectively. TEM-AEM analyses of individual particles showed that Fe is higher than Mg in the cases of high Fe + Mg content, so that some analysed particles could be

defined as nontronite. The TEM study of iberulites from sample GR8-12 provided results similar to those described above, with the only difference that it was possible to detect kaolinite. The low magnification TEM image in Fig. 10A corresponds to a clay rich area of an iberulite of sample GR8-12. There are kaolinite and illite particles up to 100 nm thick and 400 nm long. The lattice image of one of the kaolinite packets shows the typical 0.7 nm *d*-spacing corresponding to kaolinite layers (Fig. 10B). In some areas the lattice fringes of kaolinite disappear due to electron damage. The K X-ray map (Fig. 10E) indicates the location of illite crystals on the right of the region in Fig. 10A. The Si-rich grains of Fig. 10C correspond to very small quartz grains with less than 200 nm in diameter (see that these two grains have no Al, K or Fe). There are Fe oxy-hydroxides within the clay as indicated by the bright areas in the Fe X-ray map (Fig. 10F).

The chemical AEM analyses of samples TF6-98 and GR8-12 were transformed into structural formulas and their values plotted in the Al-(Fe + Mg)-K field (Fig. 11). This plot compares well with that
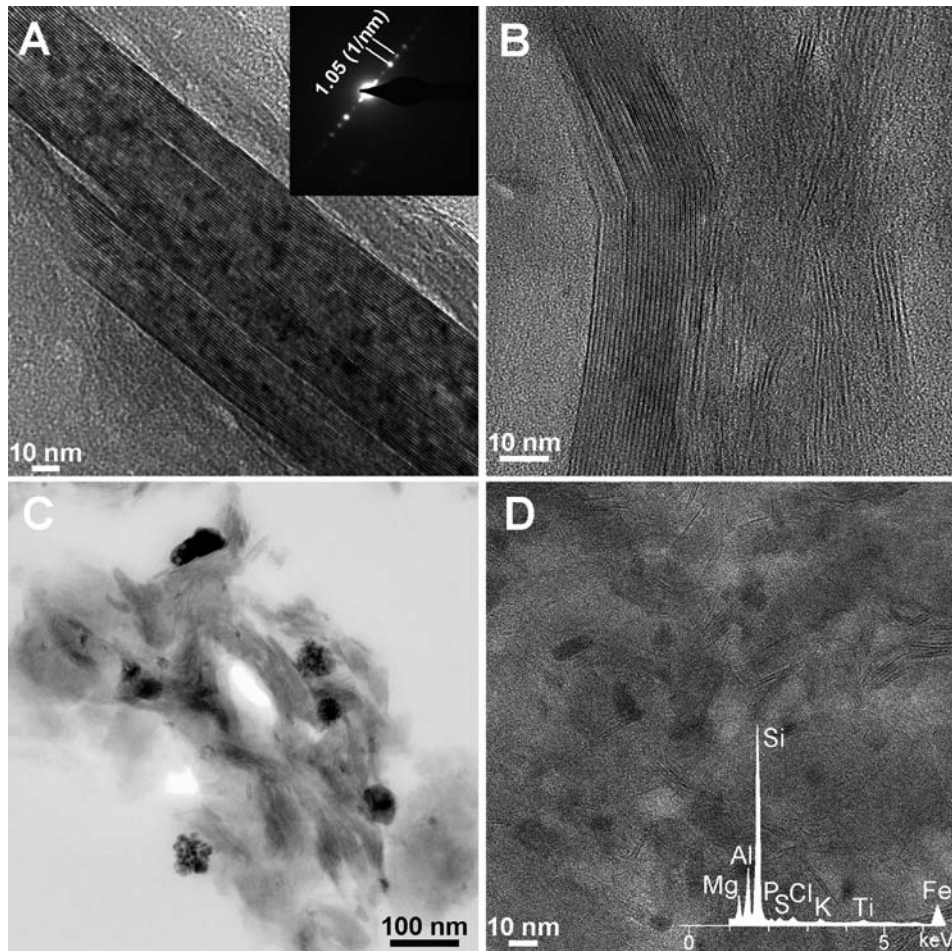
Fig. 9. TEM lattice-fringe images of clay minerals and associated phases from aerosol sample TF6-98. A) Illite packet and its SAED pattern (inset) indicating an average *d*-spacing of 1.05 nm^{-1} in the reciprocal lattice, *i.e.*, of 0.95 nm in the original lattice. B) Curved clay platelets of illite (left) and smectite (right), interpreted as an illite packet that has been opened and altered. C) Iron oxy-hydroxides (dark contrast) within smectite particles. D) Randomly oriented smectite nanoparticles with dark-contrast nanocrystals. The S and Cl detected by EDX (inset) indicate that the nanocrystals could be gypsum, halite or polyhalite, all of them detected by XRD.

from Fig. 7E. According to the structural formulas, most analysed particles are smectitic, because their layer charge does not reach 0.6 per half formula unit. Only two crystals displayed a layer charge >0.6, at 0.61 and 0.73 per half formula unit, both of them from sample GR8-12. No analysis reached a K content of 0.8 atoms per half formula unit, a typical value for illite. However, these chemical values could correspond to mixtures of illite and smectite. Kaolinite crystals, only detected in sample GR8-12, showed the presence of some Fe and Mg (data point marked with an arrow in Fig. 11).

4. Discussion

4.1. Mineral composition of iberulite aggregates

The mineralogy of the studied aerosol samples, both iberulites and common aerosols, matches well previous studies of Saharan dust (Table 2). Quartz, plagioclase, K-feldspar and carbonates are always present, and clays are represented by illite, kaolinite and smectite, with the frequent addition of chlorite. Other phases identified are salts such as gypsum and halite.

In this contribution, the focus is on the iberulites, and mineralogical results from concurrent aerosols are used to contextualize the composition of iberulite aggregates. It is widely recognized that the composition of the Saharan dust has a decreasing influence of the specific source area with increasing distance of transportation

(Chamley, 1989), which means that there is a process of dust mixing from several sources as it travels. The atmospheric processing by gravitational settling causes the relative mineral proportions to change as the travelled distance increases, with the finer-sized minerals becoming more abundant. This is reflected in Table 2, which shows a clear increase in the relative proportion of clay minerals in Saharan dust with increasing distance of travel. Within clay minerals, Table 2 shows a great variation of composition depending on plume events and no apparent correlation to travelled distance. Such differences are probably linked to dust sources and preferential aggregation and deposition during transport.

The mineralogical description of dust aerosols and, in particular, iberulites, is not exhausted with the major phases that can be detected and quantified using XRD. In particular, Díaz-Hernández and Párraga (2008) describe hematite and amorphous Fe oxy-hydroxides in iberulites using TEM. We also found Fe oxy-hydroxide phases of very small size (20–50 nm) clearly discernible only using TEM (Figs. 8E, 9C and 10F) and possibly with EPMA (small grains in white in the two bottom aggregates in Fig. 6B). Although these phases are below detection limit for macroscopic techniques, they may be of importance in aerosols in general and in iberulites in particular. Most likely, they cause the pinkish colour of iberulites (Fig. 1) and the reddish colour frequently observed in Saharan dust. In such a case, Fe oxy-hydroxides would control light absorption and play an important role in the thermal behaviour of
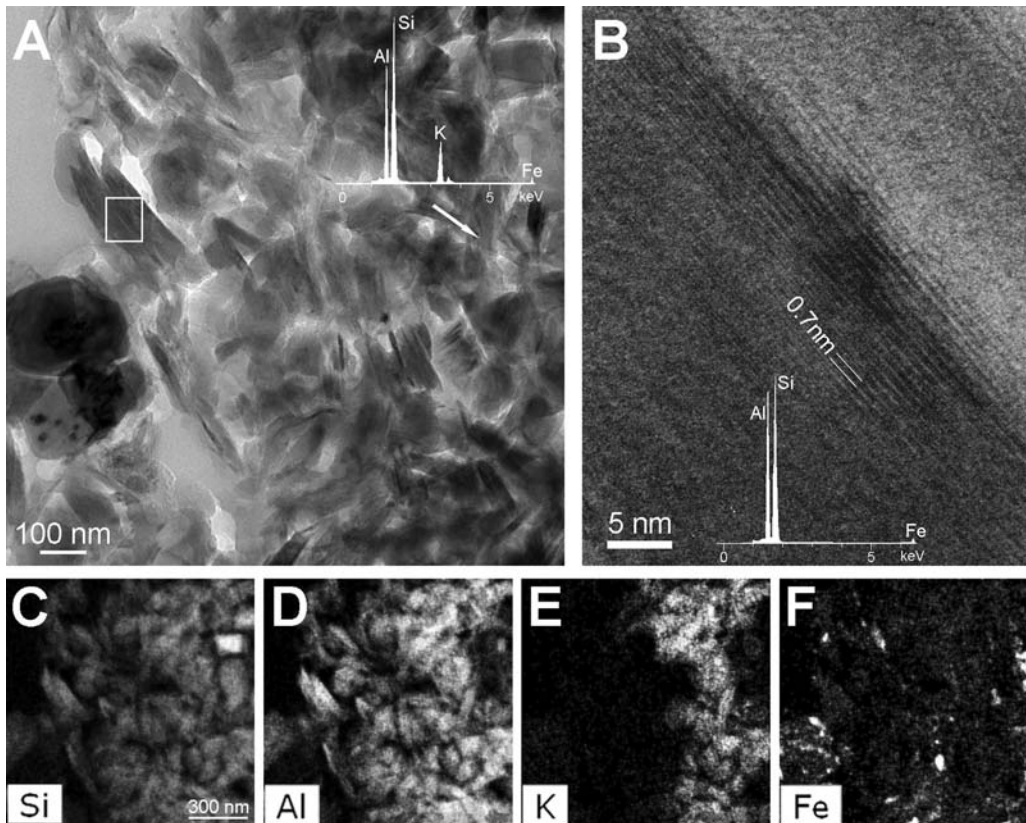
Fig. 10. TEM images and chemical data of an iberulite from sample GR8-12. A) Low magnification image of illite and kaolinite crystals. The EDX spectrum corresponds to illite. B) Lattice fringe image and EDX spectrum of the two kaolinite packets within the box in A. The incomplete fringe contrast in the central area is due to electron damage to the crystal structure. C) to F) Si, Al, K and Fe X-ray maps of the area shown in A.
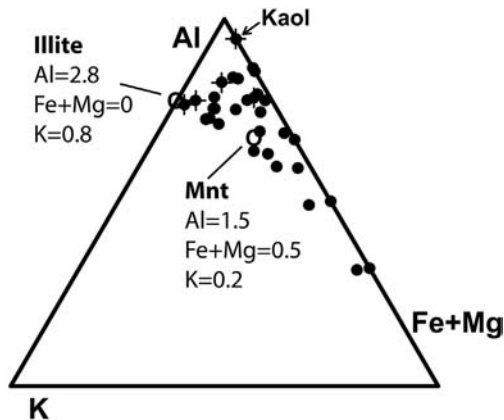
Fig. 11. Composition of smectite and illite particles and one kaolinite particle (arrow) from samples TF6-98 (common aerosols) and GR8-12 (iberulites; crosses superimposed on the dots), plotted in the ternary diagram Al−K−(Fe + Mg), from TEM-EDX data. Two reference compositions are provided (open dots) on the basis of half formula unit (or $O_{10}[OH]_2$), corresponding to an end-member illite with no Fe or Mg, and to a typical montmorillonite.

these dust aerosols in the atmosphere (Sokolik and Toon, 1999; Balkanski et al., 2007).

No quantification of the mineral phases was carried out in our study because the sample containing only iberulites (from GR8-12) was so small that no XRD powder analysis could be performed. Its corresponding XRD study was on an oriented mount that enhances clay 00l peak intensities and precludes quantification. An approach to mineral phase quantification was carried out on the mineral maps developed on EPMA data (Fig. 7) by measuring the surface area corresponding to each type of mineral phase identified in the analyses. In order to test whether this result from four iberulite aggregates is representative there is the need to carry out similar analyses in many others, which are not available at the moment. In addition, the cross section of the grains within the aggregate observed in preparations for EPMA analysis is not identical to their volume. However, it can be assumed that the volume and cross section of mineral particles are approximately proportional because particles with large aspect ratios (e.g., dimension perpendicular to the image/cross section) will be uncommon. Finally, the density of all minerals involved is not the same although very similar as the values are within 2.5–2.84 g cm^{-3}, so that ignoring density differences is a good approximation. Possibly, then, the main uncertainty in the mineral proportion assessment is the representativity of the small statistical sample studied, where three aggregates are from an event in 2014 and one from 2012 (bottom one in Fig. 7).

The differences in total clay content found between the four individual iberulites is small (standard deviation of 5.4%) and provide an argument in support of a representative statistical sample. It can be observed that the clay mineral content of the Saharan dust collected in Granada during the entire year 1992 is ~33%, very close to the values of dust collected in the Sahara (28–29%) and approximately half of that in dust collected in distant areas (Table 2). As the iberulites were collected in Granada, our assessment of ~52% clay in iberulites is significantly higher than the ~33% content in total dust. This large difference suggests that clays are concentrated in iberulites with respect to the total mineral aerosol sample. This implies that the formation of

Table 2
Mineralogy (wt%) of Saharan dust collected in-situ and at different distances from the Sahara. Unless indicated otherwise, the samples were collected on specific plume events.

Place of collection	Event	Sme	Ilt	Kln	Plg	Chl	Qz	Fsp	Cal	Dol	Hl	Gp	Am[a]	Total	Clay	References
NE Spain	1987	10	39.5	7.5	8.5		15	6	7.5	6				100	65.5	Avila et al. (1997)
NE Spain	1988	12	40.5	9	8.5		15	5	5.5	5				100.5	70	Avila et al. (1997)
NE Spain	1991	17.5	26.5	4.5	7		17.5	3.5	19.5	6				102	55.5	Avila et al. (1997)
NE Spain	1992	33.5	27.5	13	6.5		13	4.5	1.7	1.2				100.9	80.5	Avila et al. (1997)
Cape Verde	1974	8	32	18	4.9	9	16.5	2	4.4			6		100.8	67	Glaccum and Prospero (1980)
SE Spain	1992 (all year)	10.2	10.8	8.1		3.7	27.6	0.8	12.5	13.7	4.5	4.5	4	100.4	32.8	Diaz-Hernandez et al. (2011)
Africa 20-27°N 5°E	4—23 May 1974	6	8	8	4	2	32	17	20			3		100	28	Paquet et al. (1984)
Africa 27-35°N 5°E	4—23 May 1974	7.25	7.83	4.93	4.35	5.8	20	10	40					100.2	29	Paquet et al. (1984)

[a] Am: non-crystalline substances.

iberulites in the atmosphere (Díaz-Hernández and Párraga, 2008) selects clay minerals preferentially within the dust plume. We suggest that this may be due to their higher hygroscopicity or small particle size, both of which facilitate capture by water droplets.

It is also clear that gypsum is depleted in the iberulites studied here as compared to the total aerosol content. XRD patterns of the latter (Fig. 2) show obvious gypsum peaks, whereas XRD traces of the iberulites do not display them (Fig. 3). Gypsum or other calcium sulfate phases are present in the iberulites as detected by SEM-EDX (Fig. 4) and EPMA S-element analysis (Fig. 6D), although the relative proportion of such phases is obviously very small and consistent with being below the detection limit of XRD. However, Díaz-Hernández and Párraga (2008) did detect gypsum in iberulites from other events using XRD. A most common origin of gypsum in mineral aerosols is interaction of atmospheric SO_2 with (mainly) calcite (Glaccum and Prospero, 1980; Gieré and Querol, 2010). However, gypsum derived from the source is a possibility (Table 2, data from aerosols collected in Africa by Paquet et al., 1984). In our case, gypsum may have its origin in the aerosol before iberulite formation, in the iberulite while it forms, and in the dust source. The variable gypsum content in iberulites from different events may be due to different atmospheric conditions (in the most broad sense) affecting the formation of sulfate minerals in the iberulite or in the transported aerosol before iberulite formation starts. The presence of gypsum and other sulfate phases and its relation to the abundant clays observed in the iberulites is further discussed below.

4.2. Role of clay in the formation of the iberulites

Figs. 4, 5 and 7 illustrate the structure of the iberulite aggregates. The SEM micrographs of their surfaces show that they are covered by a layer of clay minerals (Fig. 4) with overlapping flakes parallel to the surface. Even if large non-clay mineral grains are located next to the surface, the iberulites are typically covered by a thin clay layer (Figs. 5C and 7). Clay coatings surrounding some K-feldspars and other aluminosilicate grains (arrows in Fig. 7A) as well as sericite pseudomorphs after muscovite (arrow in Fig. 7C) formed during chemical weathering in the source soils, and they are not related to the particle arrangement of the iberulites. On the clay cover there are multiple sulfate particles (probably gypsum), typically <100 nm across (Fig. 4D). Inside the aggregates, there seems to be a rather random distribution of mineral particles, with clays providing a matrix of variable thickness surrounding other mineral grains in an irregular fashion. Such structure is evident in Figs. 7 and 5C. The empty space in the centre of Fig. 5A was produced during sample preparation. Gypsum is also distributed within the iberulites, seemingly in connection with the clay matrix (Fig. 6D). There are a few S-rich particles of relatively large size (Fig. 6D), notably that marked with an arrow, near to the iberulite surfaces. These particles appear to contain only S, which can be interpreted as that they

consist of ammonium sulfate for two reasons. First, this salt has been reported in dust aerosols. Recent analysis of Asian dust with X-ray absorption near-edge structure has demonstrated the presence of ammonium sulfate as a major sulphur species (Ma et al. (2013) and references therein). Also, ammonium sulfate has been identified in Saudi Arabia aerosols (Posfai et al., 2013). The second reason is that our EPMA apparatus is not equipped to detect N. Thus, the textural features shown in this paper for the distribution of clays and sulfates in the iberulites, both homogeneously distributed within the iberulites, are different from those originally described by Díaz-Hernández and Párraga (2008), who located both the clay minerals and the sulfates mainly in the outer part of the aggregates.

Díaz-Hernández and Párraga (2008) found a preferential distribution of sulfates in the outer part of the iberulites using S-Ca maps from SEM-EDX, in contrast with our uniform distribution obtained with EPMA S maps (Fig. 6D). They studied iberulites collected between 1999 and 2005, whereas those studied here were collected in 2012 and 2014. Gypsum is present in non-iberulite aerosols deposited during the events of both studies, as observed by XRD analysis. In contrast, Díaz-Hernández and Párraga (2008) found gypsum in the XRD patterns of iberulites, whereas gypsum was not detected in our XRD analysis of iberulites (Fig. 3). Also, they found greater quantities of sulfate grains in their iberulites (using SEM) than we did (using EPMA). We interpret that sulfate-containing aerosol particles are captured by water droplets (iberulites precursors) and that these sulfates become distributed uniformly across the iberulites as water evaporates, as described in the present contribution. The concentration of sulfates on iberulite surfaces from the 1999—2005 period (Díaz-Hernández and Párraga, 2008) probably have a different origin, and we hypothesize that they were the result of processes occurring late during iberulite formation and thus taking place only at their surface. It is possible that industrial emissions containing SO_2 were active in SE Spain during the collection time span (1999—2005). Reaction of SO_2 with the water contained in the iberulite precursors at an advanced stage of formation would explain the concentration of sulfates on the surface. These industrial operations in the area may have since ceased or been modernized to decrease contamination output, thus explaining the current lack of sulfates on or near the surface of the iberulites. This possibility could not be confirmed but it is in good agreement with the known trends of decreased anthropogenic SO_2 output worldwide (Sharma et al., 2004; Kelly et al., 2005; Marmer et al., 2007; Quinn et al., 2009; Hirdman et al., 2010; Hand et al., 2012; Tørseth et al., 2012; Waldner et al., 2014). If the above interpretation is valid, it is implied that the larger part of the sulfates in the iberulites studied by Díaz-Hernández and Párraga (2008) was produced by interaction with SO_2 gases at the last stages of iberulite formation, and that the capture and/or retention of sulfate phases by iberulite precursors at an early stage is not efficient.

The different distribution of clay minerals in iberulites as

observed in the present contribution and that of Díaz-Hernández and Párraga (2008) appears to be related to the analytical tool used for observation. Cross-section SEM images from Díaz-Hernández and Párraga (2008) and in the present paper might suggest clay aggregation towards the surface of iberulites (Fig. 5). Also, the thin clay layer on the outer surface (Fig. 4) may bias the interpretation in this direction. However, the EPMA chemical mapping of the cross sections reveals high clay contents throughout the entire aggregates (Fig. 7).

Iberulites cannot be structures generated at the source areas for several reasons. First, such big particles (>50 μm) are not likely to travel long distances (Jeong et al., 2014). Typical size distributions of aerosol particles (other than those generated by volcanic eruptions) reach a maximum diameter of 50 μm (Gieré and Querol, 2010). Second, their spherical shape and the vortexes that can be observed in some of them (Díaz-Hernández and Párraga, 2008) match those of water drops modelled by hydrodynamic forces during fall. Thus, it must be concluded with Díaz-Hernández and Párraga (2008) that iberulites are generated by the interaction of dust aerosol and water droplets, with aerosol particles acting as condensation points and then by capture of more aerosol particles as the drops fall. This process does not require them to be formed exactly above the site where they are deposited, and allows for certain horizontal travel constrained by their large size and thus short residence time in the atmosphere.

The enrichment of clay minerals in iberulites as compared to the composition of the total aerosol sample suggested in our study could be explained by the greater efficiency of water drops in capturing clay particles over coarser particles. This is very likely in the light of the research by Beard and Grover (1974) and Grover and Pruppacher (1985), as described by Díaz-Hernández and Párraga (2008). During the fall of the water drops, there is a redistribution of the particulate material within them. In the initial stages, the water drops undergo strong internal circulation (Le Clair et al., 1972) that relocates the particles. The volume of a typical raindrop (1–5 mm diameter) is much larger than the volume occupied by the aerosol particles within it (iberulites have diameters of up to ~100 μm; Fig. 1). In the later stages, the volume of the raindrop decreases as water evaporates and the particles are increasingly confined, producing a particle distribution shaped by water flow and the electrical forces between mineral particles and between water molecules and particles. When the volume of the raindrop reaches that of the added volume of the mineral particles inside, the aggregate is shaped by the drop surface, explaining the spherical shape and the vortexes described by Díaz-Hernández and Párraga (2008). In this process, the mineral grains are distributed in a somewhat random fashion, with lumps of small clay particles mixing with larger mineral grains. However, a layer of clay platelets is deposited at the very surface. It is not clear why this is so but we can conjecture two possibilities. One is that some clay particles remain just below the water–air interface during the fall, parallel to the surface of the raindrop. As the water evaporates, these platelets are finally attached flat on the surface of the iberulite. Another possibility is that the clay particles at the surface of an iberulite about to dry out are reoriented by surface tension and/or electrical forces and located flat on the surface. Given their large surface-to-volume ratio, the particles cover the aggregate almost entirely. Any dissolved species will precipitate in the late stages of drying, more likely where water takes longer to evaporate. Clay minerals are hygroscopic due to residual surface charge and large surface area. Thus, it is plausible that residual water accumulates on clay surfaces and within clay lumps, driving dissolved ions to these regions. This would explain the apparent association of gypsum with clay in the iberulites (Figs. 4, 5D and 6D).

5. Conclusions

In circum-Mediterranean areas, aerosol mineral particles from Saharan plumes can coalesce by interaction with atmospheric water into large spherical aggregates (up to ~100 μm), termed iberulites.

Common and iberulite-rich aerosols from the Sahara contain mainly quartz, carbonates, feldspars and clays (illite, smectite and kaolinite). The texture of the iberulites studied consists of coarse mineral particles embedded in a matrix of clay minerals, which also surrounds the entire spheroidal aggregate. The clays appear to be enriched in the iberulites as compared to common aerosols and play a significant role in their formation. They are responsible for some particular textural features of the iberulites, such as the external clay coating and clay distribution between coarser mineral particles, which is likely to provide mechanical strength to these aggregates.

Some details of the structure and composition of the iberulites studied here are different from those of previously observed samples, suggesting modifications driven by the dust sources and atmospheric conditions, possibly including anthropic activity. Specifically, the comparison of samples from iberulite sets recovered years apart in the Granada area (SE Spain) shows a recent decrease of sulfate content, which we interpret to be caused by decreased SO_2 anthropic emission.

Minor Fe oxy-hydroxides phases, distributed homogenously within the iberulites and responsible for their pinkish colour, must be taken into account in relation to radiation absorption processes and the thermal behaviour of these dust aerosols in the atmosphere.

Acknowledgements

This work was supported by the P11-RNM-7067 project from the Junta de Andalucía (C.E.I.C.-S.G.U.I.T.). A.S.N. acknowledges support from the human resources training programme "Salvador de Madariaga" (Ministerio de Educación, Cultura y Deporte, Spain). Support was also provided by The Natural History Museum hosting the visits of A.S.N. and J.L.H.D. We would like to thank A. González, M. Mª Abad, C. Hernández, M. A. Hidalgo and J. Montes (C.I.C. and Department of Mineralogy, University of Granada) for guidance with analytical electron studies and sample preparation.

References

Avila, A., Queralt-Mitjans, I., Alarcón, M., 1997. Mineralogical composition of African dust delivered by red rains over north-eastern Spain. J. Geophys. Res. 102 (D18), 21977–21996.

Balkanski, Y., Schultz, M., Claquin, T., Guibert, S., 2007. Reevaluation of mineral aerosol radiative forcings suggests a better agreement with satellite and AERONET data. Atmos. Chem. Phys. 7, 81–95.

Beard, K.V., Grover, S.N., 1974. Numerical collision efficiencies for small raindrops colliding with micron size particles. J. Atmos. Sci. 31, 543–550.

Bout-Roumazeilles, V., Combourieu, N., Peyron, O., Cortijo, E., Landais, A., Masson-Delmotte, V., 2007. Connection between south Mediterranean climate and North African atmospheric circulation during the last 50000 yrBP North Atlantic cold events. Quat. Sci. Rev. 26, 3197–3215.

Chamley, H., 1989. Clay Sedimentology. Springer-Verlag, Berlin, p. 623.

Díaz-Hernández, J.L., Miranda, J.M., 1997. Tasas de deposición de polvo atmosférico en un área semiárida del entorno mediterráneo occidental. Est. Geol. 53, 211–220.

Díaz-Hernández, J.L., Martín-Ramos, J.D., López-Galindo, A., 2011. Quantitative analysis of mineral phases in atmospheric dust deposited in the south-eastern Iberian Peninsula. Atmos. Environ. 45, 3015–3024.

Díaz-Hernández, J.L., Párraga, J., 2008. The nature and tropospheric formation of iberulites: pinkish mineral microspherulites. Geochim. Cosmochim. Acta 72, 3883–3906.

Engelbrecht, J.P., Derbyshire, E., 2010. Airborne mineral dust. Elements 6, 241–246.

Franzen, L.G., Hjelmroos, M., Karllberg, P., Brorstrom-Lunden, E., Juntto, S., Savolainen, A., 1994. The yellow snow episode of northern Fennoscandia, March 1991: a case study of long distance transport of soil, pollen and stable organic

compounds. Atmos. Environ. 22, 3587–3604.

Gieré, R., Querol, X., 2010. Solid particulate matter in the atmosphere. Elements 6, 215–222.

Glaccum, R.A., Prospero, J.M., 1980. Saharan aerosols over the tropical North-Atlantic: mineralogy. Mar. Geol. 37, 295–321.

Goudie, A.S., Middleton, N.J., 2001. Saharan dust storms: nature and consequences. Earth Sci. Rev. 56, 179–204.

Grover, S.N., Pruppacher, H.R., 1985. The effect of vertical turbulent fluctuations in the atmosphere on the collection of aerosol particles by cloud drops. J. Atmos. Sci. 42, 2305–2318.

Hand, J.L., Schichtel, B.A., Malm, W.C., Pitchford, M.L., 2012. Particulate sulfate ion concentration and SO_2 emission trends in the United States from the early 1990s through 2010. Atmos. Chem. Phys. 12, 10353–10365.

Hirdman, D., Burkhart, J.F., Sodemann, H., Eckhardt, S., Jefferson, A., Quinn, P.K., Sharma, S., Ström, J., Stohl, A., 2010. Long-term trends of black carbon and sulfate aerosol in the Arctic: changes in atmospheric transport and source region emissions. Atmos. Chem. Phys. 10, 9351–9368.

Jeong, G.Y., Kim, J.Y., Seo, J., Kim, G.M., Jin, H.C., Chun, Y., 2014. Long-range transport of giant particles in Asian dust identified by physical, mineralogical, and meteorological analyses. Atmos. Chem. Phys. 14, 505–521.

Kelly, V.R., Lovett, G.M., Weathers, K.C., Likens, G.E., 2005. Trends in atmospheric ammonium concentrations in relation to atmospheric sulfate and local agri-culture. Environ. Pollut. 135, 363–369.

Kok, J.F., 2011. A scaling theory for the size distribution of emitted dust aerosols suggests climate models underestimate the size of the global dust cycle. Proc. Nat. Acad. Sci. 108, 1016–1021.

Lawrence, C.R., Neff, J.C., 2009. The contemporary physical and chemical flux of aeolian dust: a synthesis of direct measurements of dust deposition. Chem. Geol. 267, 46–63.

Le Clair, B.P., Hamielec, A.E., Pruppacher, H.R., Hall, W.D., 1972. A theoretical and experimental study of the internal circulation in water drops falling at terminal velocity in air. J. Atmos. Sci. 29, 728–740.

Lorimer, G.W., Cliff, G., 1976. Analytical electron microscopy of minerals. In: Wenk, H.R. (Ed.), Electron Microscopy of Minerals. Springer-Verlag, New York, pp. 506–519.

Ma, Q., He, H., Liu, Y., Liu, C., Grassian, V.H., 2013. Heterogeneous and multiphase formation pathways of gypsum in the atmosphere. Phys. Chem. Chem. Phys. 15, 19196–19204.

MacEwan, D., Wilson, M.J., 1984. Interlayer and intercalation complexes of clay minerals. In: Brindley, G.W., Brown, B. (Eds.), Crystal Structures of Clay Minerals and their X-Ray Identification. Mineralogical Society, London, UK, pp. 197–248.

Marmer, E., Langmann, B., Fagerli, H., Vestreng, V., 2007. Direct shortwave radiative forcing of sulfate aerosol over Europe from 1900 to 2000. J. Geophys. Res. Atmos. 112, D23S17. http://dx.doi.org/10.1029/2006JD008037.

Martín-Ramos, J.D., Díaz-Hernández, J.L., Cambeses, A., Scarrow, J.H., López-Galindo, A., 2012. Pathways for quantitative analysis by X-ray diffraction. In: Aydinalp, C. (Ed.), An Introduction to the Study of Mineralogy. InTech, pp. 73–92.

Miller, R.L., Cakmur, R.V., Perlwitz, J., Geogdzhayev, I.V., Ginoux, P., Koch, D., Kohfield, K.E., Prigent, C., Ruedy, R., Schmidt, G.A., Tegen, I., 2006. Mineral dust aerosols in the NASA Goddard Institute for Space Sciences ModelE atmospheric general circulation model. J. Geophys. Res. 111, D06208. http://dx.doi.org/10.1029/2005JD005796.

Moulin, C., Lambert, C.E., Dulac, F., Dayan, U., 1997. Control of atmospheric export of dust from North Africa by the North Atlantic oscillation. Nature 387, 691–694.

Paquet, H., Coudé-Gaussen, G., Rognon, P., 1984. Etude minéralogique de poussières sahariennes le long d'un itinéraire entre 19° et 35° de latitude nord. Rev. Géol. Dyn. Géogr. Phys. 25, 257–265.

Pósfai, M., Axisa, D., Tompa, É., Freney, E., Bruintjes, R., Buseck, P.R., 2013. In-teractions of mineral dust with pollution and clouds: an individual-particle TEM study of atmospheric aerosol from Saudi Arabia. Atmos. Res. 122, 347–361.

Quinn, P.K., Bates, T.S., Schulz, K., Shaw, G.E., 2009. Decadal trends in aerosol chemical composition at Barrow, Alaska: 1976–2008. Atmos. Chem. Phys. 9, 8883–8888. http://dx.doi.org/10.5194/acp-9-8883-2009.

Rodríguez, S., Querol, X., Alastuey, A., Kallos, G., Kakaliagou, O., 2001. Saharan dust contributions to PM10 and TSP levels in southern and eastern Spain. Atmos. Environ. 35, 2433–2447.

Rodwell, M.J., Rowell, D.P., Folland, C.K., 1999. Oceanic forcing of the wintertime North Atlantic oscillation and Europe climate. Nature 398, 320–323.

Seinfeld, J.H., Pandis, S.M., 2006. Atmospheric Chemistry and Physics from Air Pollution to Climate Change. Wiley-Interscience, New York, p. 1326.

Sharma, S., Lavoue, D., Cachier, H., Barrie, L., Gong, S., 2004. Long-term trends of the black carbon concentrations in the Canadian Arctic. J. Geophys. Res. 109, D15203. http://dx.doi.org/10.1029/2003JD004331.

Shinn, D.B., North, G.R., Bowman, K.P., 2000. A summary of reflectometry profiles from the first year of TRMM radar data. J. Clim. 13, 4072–4086.

Sokolik, I.N., Toon, O.B., 1999. Incorporation of mineralogical composition into models of the radiative properties of mineral aerosol from UV to IR wave-lengths. J. Geophys. Res. Atmos. 104, 9423–9444.

Swap, R.M., Gaustamy, M., Greco, S., Talbot, R., Kallberg, P., 1992. Saharan dust in the Amazon basin. Tellus B 44, 133–149.

Tegen, I., Lacis, A.A., 1996. Modeling of particle size distribution and its influence on the radiative properties of mineral dust aerosol. J. Geophys. Res. 101, 19237–19244.

Tørseth, K., Aas, W., Breivik, K., Fjæraa, A.M., Fiebig, M., Hjellbrekke, A.G., Lund Myhre, C., Solberg, S., Yttri, K.E., 2012. Introduction to the European monitoring and evaluation programme (EMEP) and observed atmospheric composition change during 1972–2009. Atmos. Chem. Phys. 12, 5447–5481.

Waldner, P., Marchetto, A., Thimonier, A., Schmitt, M., Rogora, M., Granke, O., Mues, V., Hansen, K., Karlsson, G.P., Zlindra, D., Clarke, N., Verstraeten, A., Lazdins, A., Schimming, C., Iacoban, C., Lindroos, A.-J., Vanguelova, E., Benham, S., Meesenburg, H., Nicolas, M., Kowalska, A., Apuhtin, V., Napa, U., Lachmanov, Z., Kristoefel, F., Bleeker, A., Ingerslev, M., Vesterdal, L., Molina, J., Fischer, U., Seidling, W., Jonard, M., O'Dea, P., Johnson, J., Fischer, R., Lorenz, M., 2014. Detection of temporal trends in atmospheric deposition of inorganic ni-trogen and sulfate to forests in Europe. Atmos. Environ. 95, 363–374.